POLITECNICO DI TORINO

Master's degree course in Nanotechnologies for ICTs

Master's Degree Thesis

Testing and modeling neutron radiation damage in Silicon Photonics integrated circuits

Supervisor:
Prof. Paolo Bardella

Candidate:
Daniele Alfiero
student ID: 306007

Hosting institution:
CERN - European Organization for Nuclear Research
Internship supervisor:
Dr. Jan Troska

Academic Year 2022/2023

Per nonna Tere e nonno Mario.

"Love is the only thing we are capable of perceiving that transcends dimensions of time and space."

Acknowledgements

This project was carried out at CERN, one of the world's most exciting scientific laboratories. I am grateful to everyone who supported me throughout this new experience and introduced me to the field of scientific research. A special thanks to my supervisor, Dr. Jan Troska, for being an excellent mentor and guide for my first work experience. Thank you Carmelo and Lauri, my fantastic teachers and colleagues who have inspired and encouraged me. I am grateful for the time you gave to train me and provide me with the instruments to be autonomous. I also want to express my appreciation to my Opto team colleagues for being welcoming and warm from the very beginning. You are all wonderful people, and I am excited to share new experiences with you in the future.

I would like to thank Prof. Paolo Bardella who introduced me to the world of SiPh in the course "Photonic Devices". I am grateful to you for being my supervisor during this exciting journey. Thank you for always being available and providing me with honest and thoughtful advice. I appreciated them all.

To my family, I extend my greatest appreciation. Thank you, Mum, Dad, Diddi, and Andre, for always being there for me. Nothing is more valuable than our bond. We have faced hard times, but we have always overcome them together. I am grateful that you have always been on my side, even when it was not easy because I was pushing you away. I love you, always.

To my second family, to all my friends I want to share my gratitude and love for all your support. I am sorry that I cannot thank you one by one here, but I will find my way to let you know how valuable you all are for me. I want to tell you that without your support I would not be where I am now. Giorgia, Davide, Erika, Silvia, Martina, Gigi, Rachele, Matteo, Davide, thank you for always believing in me and for the time that you spent encouraging me. I am really lucky to have you by my side. My heart is shared with you, and I will always be there whenever you need me.

Finally, I want to thank the people who made me the person I am. To my grandparents, present and not, I give all my gratitude. You are the people who raised me with love, thank you for passing on all your values to me. I will always believe in what you have taught me and I am trying my best to live a life full of love, like you have. I love you.

Vi amo, grazie.

Abstract

The foreseen upgrades for the Large Hadron Collider (LHC) and the CERN Experiments increase the radiation tolerance requirements for the optical readout of the detectors. The High Luminosity upgrade of the LHC is set to improve integrated luminosity by tenfold compared to the original LHC design in the upcoming years. As a result, the number of particle collisions during a given period of time will considerably increase, leading to a significant increase in generated data. High-speed optical data transmission is used to transfer the data produced by the particle detectors to the data collection point.

This work analyses the impact of neutron radiation on Silicon Photonics, which is a candidate technology for next generation of radiation tolerant transceivers for High Energy Physics (HEP) applications. The EP-ESE-BE Section at CERN is conducting an R&D project to develop radiation-resistant Photonic Integrated Circuits (PICs) to be used in the harsh environment of the LHC detector. The photonic integrated circuits engineered by our research team underwent extensive testing at unprecedented levels of neutron fluence. A maximum neutron fluence of $3.8 \cdot 10^{16}$ cm^{-2} was achieved, and the experimental results show small performance degradation after high neutron fluence irradiation. Several components were electro-optically measured during neutron irradiation, such as Ring Modulators, Mach-Zehnder Modulators, and silicon-germanium Photo-Detectors. Further analysis of the effects induced by neutron irradiation on the photonic integrated circuits was conducted through TCAD simulations, which yielded good agreement with the experimental results.

Contents

List of Figures

List of Tables

Chapter 1

Introduction

1.1 CERN: the Large Hadron Collider

CERN, the European Organization for Nuclear Research, is the world's largest laboratory for High-Energy Physics (HEP) research. The mission of CERN is to deepen our understanding of the Universe and the laws that govern it, leading a collaboration between 23 Member States and sharing scientific knowledge with many countries around the world.

The Large Hadron Collider (LHC) is the world's largest and most powerful circular particle accelerator, with a circumference of 27 km, located on the border between France and Switzerland, near the city of Genève [2]. Two high-energy particle beams are injected in the LHC starting from the accelerator complex (Figure 1.1) and accelerated by radiofrequency cavities. The particle beams are guided around the ring by strong magnetic fields maintained by superconducting electromagnets. The beams travel in opposite directions, reaching near-light speed before colliding. The extremely high-energy densities and temperatures reached in the LHC collisions are similar to those that reigned in the early moments of the creation of our Universe, allowing exploration up to 10^{-12} seconds after the Big Bang. At present, the collision energy of the proton beams reaches 13 TeV. The energy released by the collision is converted into matter in the form of new particles, which are identified and tracked by CERN's detectors. These are located in four different sites within the LHC, corresponding to the four main CERN experiments: ATLAS, CMS, ALICE and LHCb. The collision rate is very high, with a bunch spacing between two particle beams of 25 ns. The luminosity is a measure of the number of potential collisions per surface unit over a given period of time, and the actual LHC accelerator is designed for the proton beams luminosity of 10^{34} $\text{cm}^{-2}\text{s}^{-1}$. Consequently, the integrated luminosity, which corresponds to the number of collisions that can occur in a certain time period, expected to be reached in 2025 is of 450 fb^{-1}, where 1 fb^{-1} equates to 100 million million collisions [3].

In the next years, the High-Luminosity upgrade of LHC (HL-LHC) is targeted to increase peak luminosity by five times with respect to nominal designs, with a maximum projected integrated luminosity of 4000 fb^{-1}, planned for the years from 2029 to 2040. This will require a major upgrade of all the technologies involved in the LHC [8].

CERN is committed to developing cutting-edge scientific research that will benefit not only the HEP experiments but also many other fields ranging from healthcare to communication technologies.

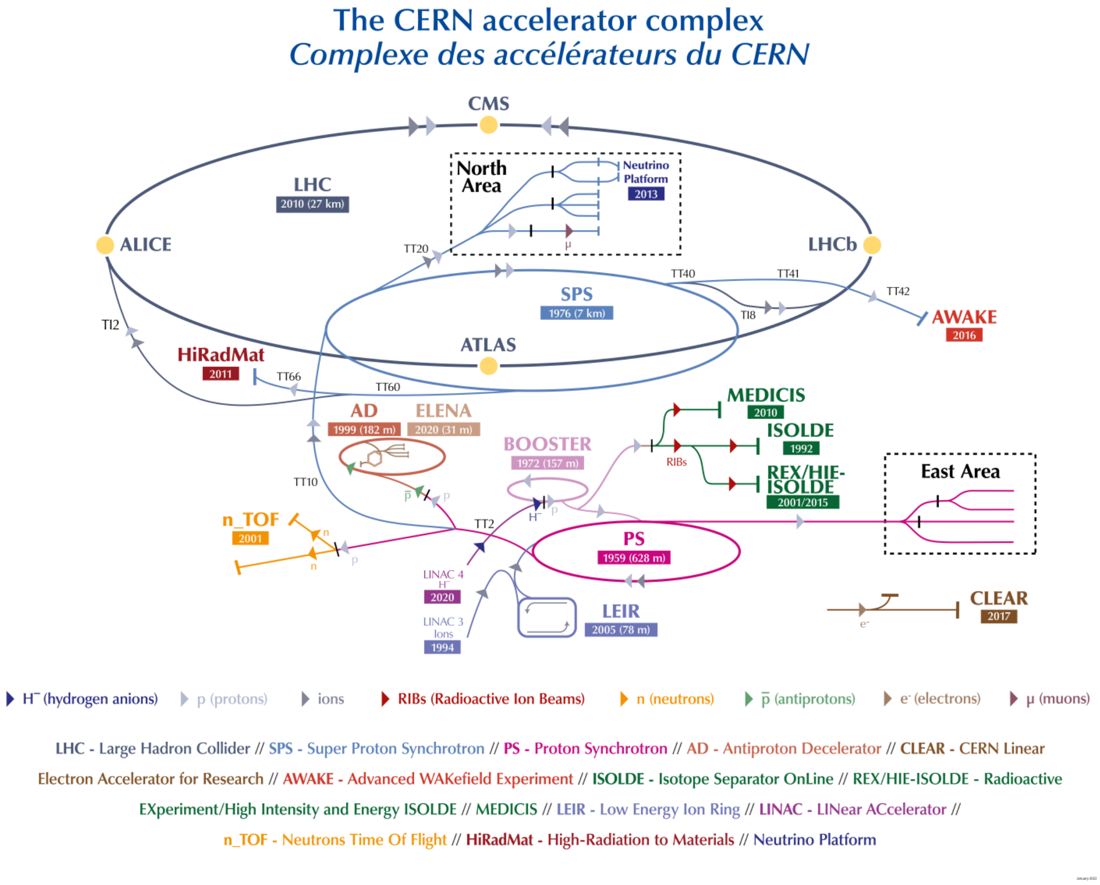

Figure 1.1: The CERN accelerator complex [2].

1.2 High-Speed Links for HEP

Among the many challenges faced by CERN’s experiments is the one involving data transmission. The data generated after particle collisions are extremely high, reaching one petabyte of collision data per second [1]. The data collected by the detectors in the Front-End (FE) must be reliably transmitted to the Back-End (BE), where all the data post-processing and analysis can take place in a radiation-free environment. The technological challenges behind this process are evident, and linking the FE to the BE requires equipment capable of withstanding harsh environments while also providing high-speed operational bandwidth. Optical data transmission is widely preferred in areas where data generation is extremely high, such as in the LHC experiments.

The data generated by the FE sensors go through a first electronic read-out, are then electro-optically converted and sent to the BE via optical fibres. The Versatile Link (VL) project aimed to develop a bidirectional optical link between FE and BE in LHC experiments, with low-mass and low-volume components capable of withstanding high radiation levels and providing transmission rates up to 5 Gb/s [4]. Optical transceivers were developed and successfully installed in all four main experiments for the LHC's Phase I upgrade, but they will not be able to cope with the data volume and tolerance levels expected in Phase II. Therefore, the project evolved into Versatile Link PLUS (VL$^+$), shown in Figure 1.2b, where the optical transceivers are designed and optimised for the HL-LHC era, providing a transmission rate of 10 Gb/s per fibre [5].

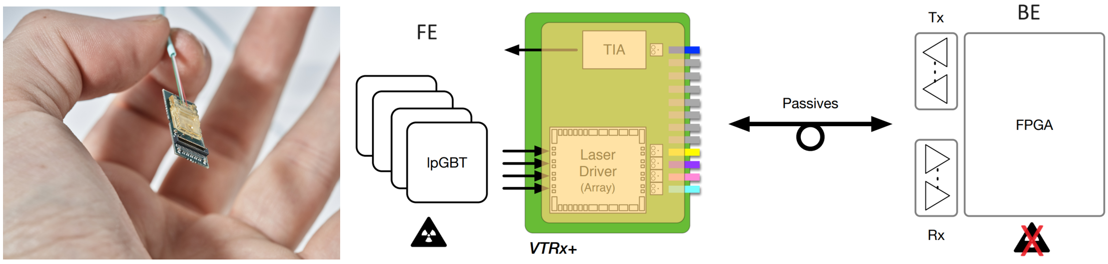

(a) *VTRx$^+$ (Credits: CERN).*

(b) *Versatile Link PLUS system.*

Figure 1.2: (a) Optical transceiver VTRx$^+$, (b) VL$^+$ system for HL-LHC upgrade [50].

The EP-ESE-BE (Experimental Physics - Electronic Systems for the Experiments - Back End) Section at CERN is working on radiation-hard devices that can operate in the harsh environment of the LHC detectors. The new version of the transceiver VTRx$^+$ (Figure 1.2a) is being developed and tested, and these components have been qualified for 1 MGy of total ionising dose, $1{\cdot}10^{15}$ neutrons/cm^2 and $1{\cdot}10^{15}$ hadrons/cm^2 fluence [6]. Despite the ability of these modules to withstand such high levels of radiation, the planned upgrades for the final runs of HL-HLC are expected to reach a total ionising dose of 12 MGy(Si) and 1 MeV neutron equivalent fluence of $2.3{\cdot}10^{16}$ $\mathrm{n_{eq}/cm^2}$. It is therefore expected that the current project can be implemented over the next decade of LHC operation, but further research will be needed to ensure high-speed links for future HEP experiments.

1.3 Silicon Photonics for High-Speed Links in HEP

The great advantage of Photonic Integrated Circuits (PICs) is the ability to achieve high-speed data transmission, large bandwidth, and low power consumption compared to those of discrete optoelectronic circuits. In particular, Silicon Photonics (SiPh) is a promising technological platform that has garnered significant interest due to its wide range of applications, from high-speed data transmission networks [44] to quantum computing, sensing and communication [9, 37], biomedical imaging and diagnostic [32, 52], avionics and aerospace [15], and High-Energy Physics [38, 41, 35, 28]. The ability to fabricate PICs on Silicon-On-Insulator (SOI) wafers has allowed the rapid development of SiPh chips over the past decade, in particular due to the compatibility of SiPh with standard CMOS technology processes.

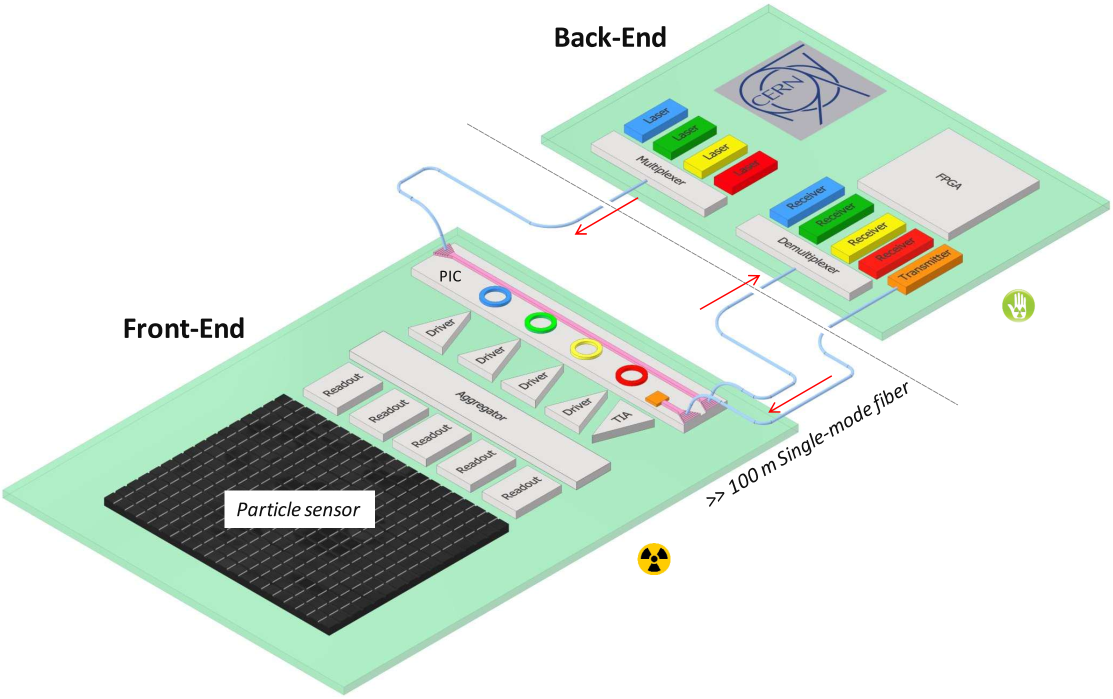

Figure 1.3: Schematic architecture of future high-speed links based on SiPh integrated circuits for HEP applications [41].

As part of CERN EP R&D program [7], SiPh is being investigated for future high-speed links for CERN experiments. Figure 1.3 shows the architecture of a proposed concept for the SiPh based data link. The SiPh PIC is located in the harsh environment of the FE, close to the particle sensor within the LHC detectors, while the most sensitive optical equipment (e.g. LASER source) or commercial electronics (e.g. FPGAs) are kept in the radiation-free area of the BE.

The particle sensor generates data after particle detection, which is condensed into a multi-Gb/s data stream by an electronic aggregator. The electrical signals are then applied to the SiPh PIC where the electro-optical conversion takes place thanks to a Wavelength-Division Multiplexing (WDM) circuit consisting of a cascade of four Ring Modulators (RMs) in the same waveguide. Long single-mode optical fibres ($\gg$100 m) are then used to transmit the optical signal to the BE zone, where commercial electronics is used for data analysis. The transmission of optical control signals from the BE to the FE reaches the PIC receiver (Rx) based on a Si-Ge Photo-Detectors (PD), which can opto-electrically convert the incoming signal to the FE electronics. The configuration of these links for HEP is asymmetric, because the data rate coming from the particle detector is greater than the transmission signal rate that has to be transmitted to the FE.

The aim of this R&D is to investigate the tolerance of SiPh PICs in a harsh environment and their suitability in high-speed links for HEP applications.

1.4 Silicon Photonics: PICv2

The work reported in this thesis analyses the radiation tolerance of a SiPh PIC developed at CERN. In particular, the PIC was exposed for the first time to the highest level of neutron fluence ever reached, up to $3.8 \cdot 10^{16}$ neutrons/cm^2, and a characterisation of the response of different devices within the chip was obtained. In parallel, a model was developed on the Synopsys® Sentaurus™ TCAD software to simulate the macroscopic effects induced by neutron damage, which agreed well with the experimental results. The PIC under test is the second version of this generation of PICs designed at CERN and manufactured by a commercial foundry as a part of a multi-project wafer run.

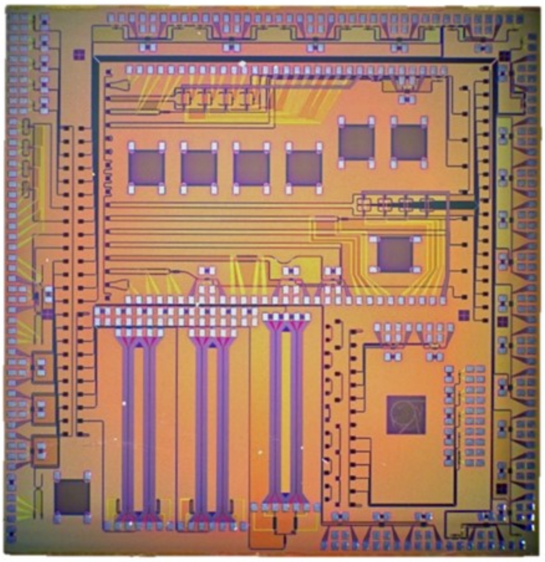

Figure 1.4: PICv2, SiPh PIC designed by CERN. Footprint: 5 mm x 5 mm.

The PICv2 comprises several photonic devices with different characteristics, the aim of which was to evaluate the devices that guarantee the best performance under irradiation. Based on previous irradiation experiments, only a subset of the devices was analysed in this study. In particular, greater attention was given on Ring Modulator 0 (RM 0), which is the reference design and will also be used for the next generation of PICs. The PIC includes several devices such as Ring Modulators, Mach-Zehnder Modulators (MZMs) and silicon-germanium Photo-Detectors (PDs). The following subsections provide a theoretical introduction to these devices, with a particular focus on the physics behind RMs, as they will be extensively analysed both in the irradiation test and with simulation, while a shorter and qualitative introduction is provided for MZMs and PDs.

1.4.1 Ring Modulator

The ring resonator basic structure consists of a looped optical waveguide that is coupled with an access device for light transport, usually a standard straight waveguide. The light entering the ring goes into resonance, i.e. the waves interfere constructively with themselves when the round trip phase shift equals an integer times 2π [14]. This generates a specific pattern in the transmission spectrum, where the optical power shows several dips at specific wavelengths that correspond to the ring resonance.

The two main configurations for a ring resonator are all-pass and add-drop, shown in Figure 1.5.

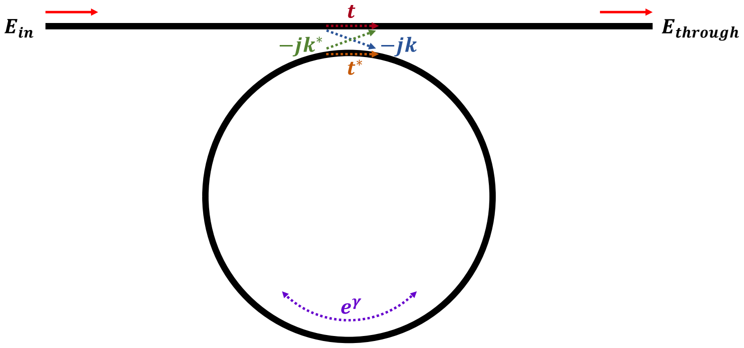

(a) *All-Pass.*

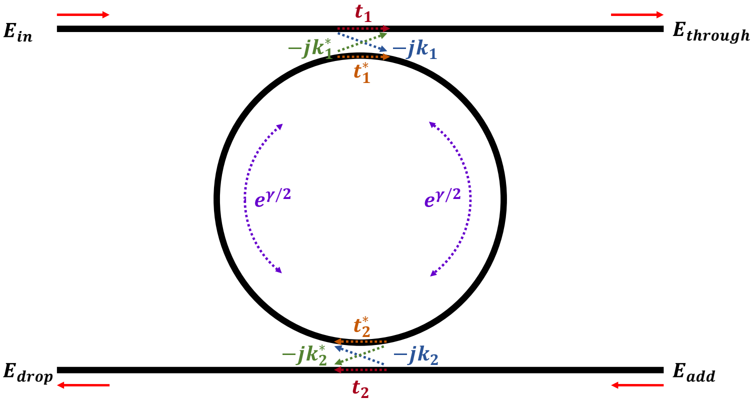

(b) *Add-Drop.*

Figure 1.5: (a) All-pass and (b) add-drop configurations of the ring resonator, with the coefficients for the evanescent and transmitted electromagnetic fields.

The ratio of the through and incident optical field amplitudes can be found by assuming a continuous wave (CW) incident light and neglecting the back reflections into the bus waveguide. By considering directional couplers with transmission t and t^* (or self-coupling) and coupling $-jk$ and $-jk^*$ for the evanescent fields (or cross-coupling), we can write:

$$\frac{E_{\text{through}}}{E_{\text{in}}} = \frac{t - e^{\gamma}}{1 - t^* e^{\gamma}}, \quad \gamma = -\alpha L - j\beta L \tag{1.1}$$

for the all-pass configuration. In (1.1), β is the propagation constant of the circulating mode, while α is the power attenuation coefficient (cm^{-1}). L is the round trip length. If no losses are assumed in the coupling sections, the power splitting ratio of the couplers $|t|^2$ and $|k|^2$ must satisfy: $|t|^2 + |k|^2 = 1$. By looking at (1.1), the modulus of the numerator is zero with periodicity equal to the Free Spectral Range (FSR), while the modulus of the denominator is zero when: $e^{-\alpha L} = 1/|t|$. Since $|t| < 1$, in order to obtain zero field at the through port, it should be $e^{-\alpha L} > 1$, which is impossible if we consider passive materials, as silicon, where power attenuation constant α is greater than zero. If the ring is coupled to another waveguide that can add another input field, the output fields at the two ports for the add-drop configuration can be found as:

$$E_{\text{through}} = E_{\text{in}} \frac{t_1 - t_2^* e^{\gamma}}{1 - t_1^* t_2^* e^{\gamma}} - E_{\text{add}} \frac{k_1^* k_2 e^{\gamma/2}}{1 - t_1^* t_2^* e^{\gamma}} \tag{1.2}$$

$$E_{\text{drop}} = E_{\text{add}} \frac{t_2 - t_1^* e^{\gamma}}{1 - t_1^* t_2^* e^{\gamma}} - E_{\text{in}} \frac{k_1^* k_2 e^{\gamma/2}}{1 - t_1^* t_2^* e^{\gamma}} \tag{1.3}$$

The resonance wavelength can be related to the effective refractive index n_{eff} according to the following equation:

$$\lambda_{\text{res}} = \frac{n_{\text{eff}} L}{m}, \quad m = 1,2,3, \ldots \tag{1.4}$$

where m is the order of the resonant mode. An example of the resonance peak of the ring resonator is shown in Figure 1.6.

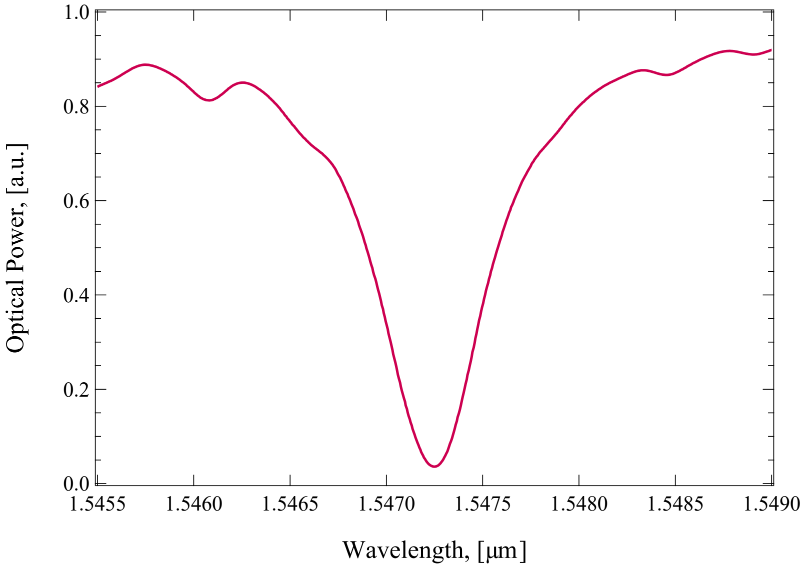

Figure 1.6: Spectrum of the resonance peak of the ring resonator.

The resonance peaks are spaced in wavelength and, in a first order approximation of the dispersion, the spacing depends on the round trip length L and on group index n_g and is known as Free Spectral Range:

$$\mathrm{FSR} = \frac{{\lambda_\mathrm{res}}^2}{n_\mathrm{g} L}. \tag{1.5}$$

The FSR is the spacing between two resonance wavelengths ($|\lambda_{\mathrm{res},m+1} - \lambda_{\mathrm{res},m}|$) in the transmission spectrum. The group index is an expression of the propagation velocity for the envelope of a propagating pulse traveling in a dispersive medium that can be written as:

$$n_\mathrm{g}(\lambda) = n_\mathrm{eff}(\lambda) - \lambda \frac{\mathrm{d}n_\mathrm{eff}(\lambda)}{\mathrm{d}\lambda}, \tag{1.6}$$

where the variation of the effective refractive index with the wavelength ($\mathrm{d}n_\mathrm{eff}/\mathrm{d}\lambda$) accounts for the material dispersion [19].

The Full-Width at Half-Maximum (FWHM) for an all-pass ring resonator can be expressed as:

$$\mathrm{FWHM} = \frac{(1-ta){\lambda_\mathrm{res}}^2}{\pi n_\mathrm{g} L \sqrt{ta}}, \quad a = e^{-\alpha L}. \tag{1.7}$$

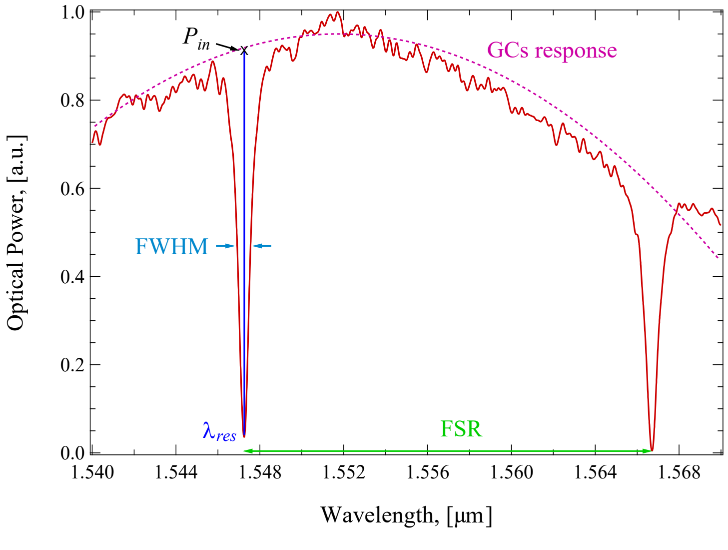

Figure 1.7: Example spectrum with some FOMs of the ring resonator.

The key figures of merite (FOMs) that are useful in the characterisation of the confinement strength of the ring are the Quality factor (Q) and the Finesse (F). The physical meaning of these relates to the temporal confinement of the fields within the ring, i.e. to the number of round-trips made by the light before being lost to internal loss and the bus waveguides. The higher the quality factor, the fewer the losses of the resonator. We can express the quality factor as:

$$Q = \frac{\lambda_{\text{res}}}{FWHM} = \frac{\pi n g L\sqrt{ta}}{\lambda_{\text{res}}(1-ta)}, \tag{1.8}$$

and the finesse as:

$$F = \frac{\text{FSR}}{\text{FWHM}} = \frac{\pi\sqrt{ta}}{1-ta}. \tag{1.9}$$

The intrinsic Extinction Ratio (ER_i) of the ring resonator can be defined as the ratio of the maximum transmitted power over the minimum power, i.e. can be written as:

$$ER_i|_{\text{dB}} = 10\log_{10}\left|\frac{P_{\text{in}}}{P_{\text{min}}}\right|, \tag{1.10}$$

where the input power is the one reported in Figure 1.7 and the minimum power corresponds to the power measured at the resonance wavelength of the ring.

The aforementioned FOMs are fundamental for the characterisation of the ring as resonator. The employment of the micro-rings for high-speed link applications reported in Section 1.2 requires the characterisation of the device as an optical modulator. The functionality of the RM relies on the electro-optical modulation achieved in Si thanks to the plasma dispersion effect [39]. The injection or depletion of carriers in silicon results in a change in both the real (Δn) and imaginary ($\Delta\alpha$) parts of the refractive index. These variations are referred to as electrorefraction and electroabsorption, respectively. Thanks to the research conducted by Soref and Bennett [46], which assessed the variation in silicon's refractive index for a broad range of carrier densities at telecommunication wavelengths of 1.3 µm and 1.55 µm, we can rely on the subsequent empirical expressions:

$$\Delta n = \Delta n_{\text{e}} + \Delta n_{\text{h}} = -\left[8.8\cdot 10^{-22}\Delta N_{\text{e}} + 8.5\cdot 10^{-18}(\Delta N_{\text{h}})^{0.8}\right], \tag{1.11}$$

$$\Delta\alpha = \Delta\alpha_{\text{e}} + \Delta\alpha_{\text{h}} = 8.5\cdot 10^{-18}\Delta N_{\text{e}} + 6.0\cdot 10^{-18}\Delta N_{\text{h}}, \tag{1.12}$$

for $\lambda_0 = 1.55$ µm. The terms ΔN_{e} and ΔN_{h} represent the variation in carrier density (cm^{-3}) for electrons and holes, respectively. Another option is to modify the refractive index of silicon with thermo-optical modulation, thanks to the large thermo-optical coefficient of silicon, which can be expressed as:

$$\frac{\text{d}n}{\text{d}T} = 1.86\cdot 10^{-4}\ \text{K}^{-1}. \tag{1.13}$$

For instance, this mechanism is used to regulate the resonance wavelength of the RMs, usually by means of tungsten micro-heaters. An example of the resonance wavelength shift due to the thermo-optic coefficient of Si at different micro-heater powers is shown in Figure 1.8. However, it is not possible to rely on thermo-optical modulation for high-frequency applications because the thermal variation is slower than the electro-optical one.

The typical structure of a RM consists of a phase shifter, which is a PN junction built into the ring rib through which light passes, and a tungsten micro-heater on top of the ring, as shown in the cross-section of Figure 1.9.

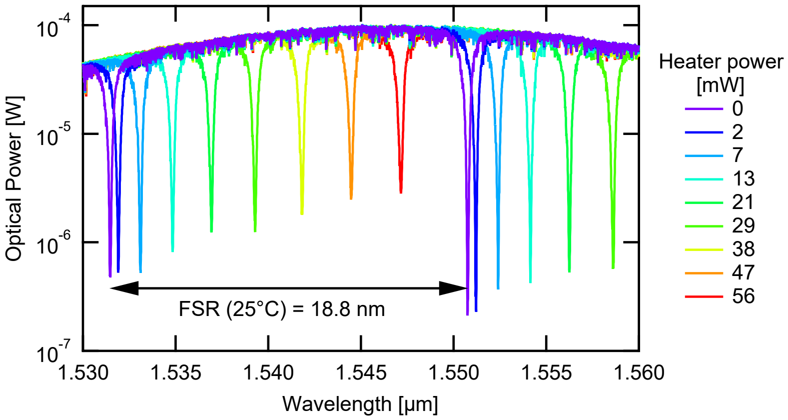

Figure 1.8: Resonance wavelength shift for different micro-heater powers.

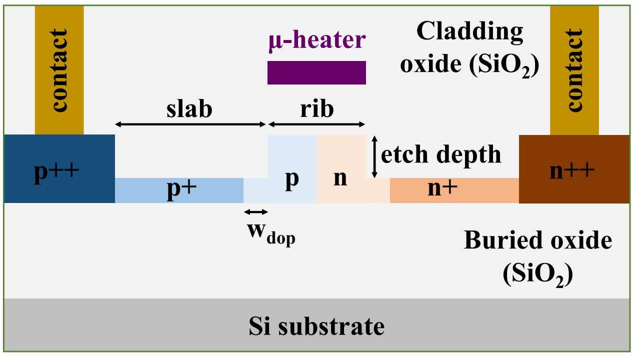

Figure 1.9: Cross-section of the phase shifter of a RM, with the micro-heater on top.

When the phase shifter is biased, the injection or depletion of carriers from the silicon rib causes a variation in the refractive index due to the plasma dispersion effect, which consequently changes the resonant wavelength of the RM, as shown in Figure 1.10a.

The parameter that evaluates the strength of this shift is the Modulation Efficiency (ME) of the RM, and it is a fundamental FOM that characterises the modulation properties of the ring. The ME is calculated as the variation in the resonance wavelength induced by a voltage applied to the phase shifter of the ring. The higher the doping, the larger the ME of the RM for the same voltage applied, but at the same time the optical losses increase. Therefore, it is important to find the right compromise between ME and optical losses for the application of the RM.

The last FOM to be discussed is the minimum Transmission Penalty (TP), which gives an indication of the input power converted to Optical Modulation Amplitude (OMA) by the RM. The TP can be expressed as:

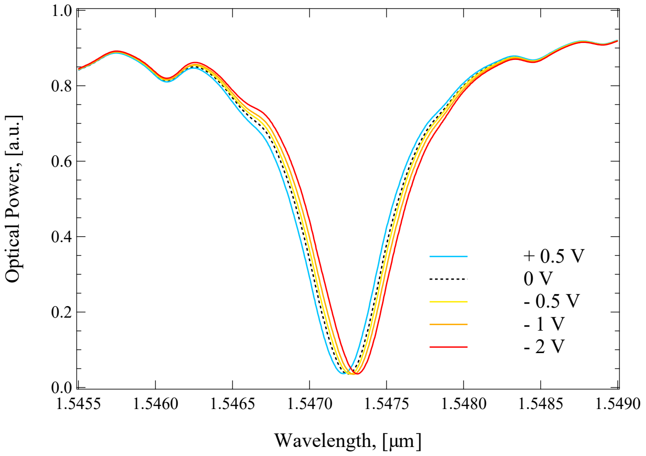

(a) *Resonant peak modulation.*

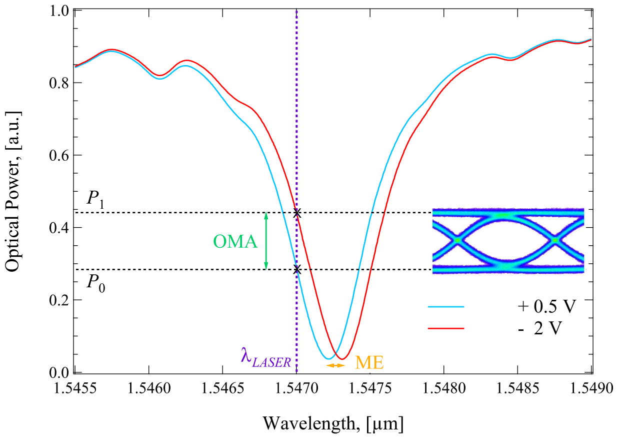

(b) *NZR.*

Figure 1.10: (a) Variation of the resonance wavelength in the optical spectrum for different voltages applied to the RM phase shifter, (b) example of NZR standard for a RM, defined by the LASER wavelength.

$$TP|_{\,\mathrm{dB}} = 10\log_{10}\left|\frac{2P_{\mathrm{in}}}{\mathrm{OMA}}\right|, \tag{1.14}$$

where $\mathrm{P_{in}}$ is the input power. The higher the TP, the lower the OMA, which is calculated as:

$$OMA = P_1 - P_0, \tag{1.15}$$

i.e. it expresses the difference between the two power levels related to the two applied voltages, which correspond to logic-level high (P_1) and logic-level low (P_0) in non-return-to-zero (NZR) digital application of the ring [25], as shown in Figure 1.10b. Examples of both TP and OMA spectra are reported in Figure 1.11. The left-minimum of the TP is the FOM which will be analysed in Subsection 2.4.2.

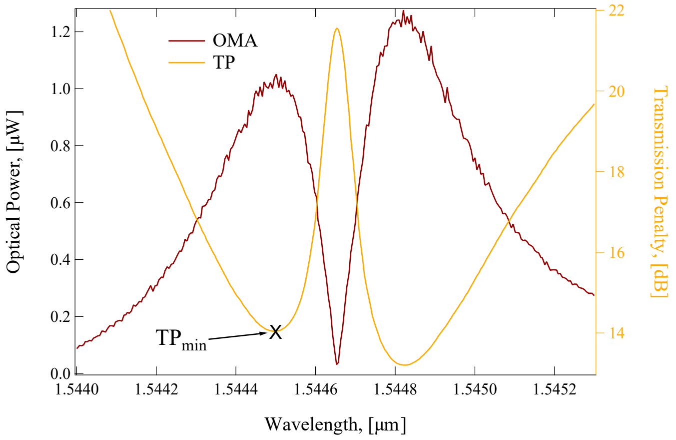

Figure 1.11: OMA (absolute value) and TP spectra examples for RM 0.

1.4.2 Mach-Zehnder Modulator

A Mach-Zehnder modulator is a device that splits incoming light into two arms and recombines the travelling fields at the end. The light travelling in the two arms can experience a variation in the optical path due to a variation in the refractive index, which ultimately causes interference when the light is recombined. A schematic representation of a MZM is shown in Figure 1.12.

MZMs in SiPh PICs rely on the same phenomenon used to modulate RMs, i.e. the plasma dispersion effect. Incoming light is split between the two arms of the MZM and travels within the ribs of each arm, where the PN junction is formed. By applying different voltages to the two arms, we are able to change the refractive indices independently, creating a shift in the optical paths. When the two light beams are recombined at the end of the device, the accumulated shift produces interference of different types. If the total phase shift between the two beams is 180°, the light undergoes destructive interference and no light is seen at the output. The voltage difference required to produce a phase shift of 180° is known as V_π [51].

Each arm cross-section is very similar to the RM cross-section shown in Figure 1.9, with different geometric dimensions and doping concentrations (and without tungsten micro-heaters). The physical length of the MZM arms is in the millimetre range, as can be seen from the PICv2 image at the bottom-left of Figure 1.4. This is the main drawback for this type of device to be implemented for Very Large Scale Integration (VLSI).

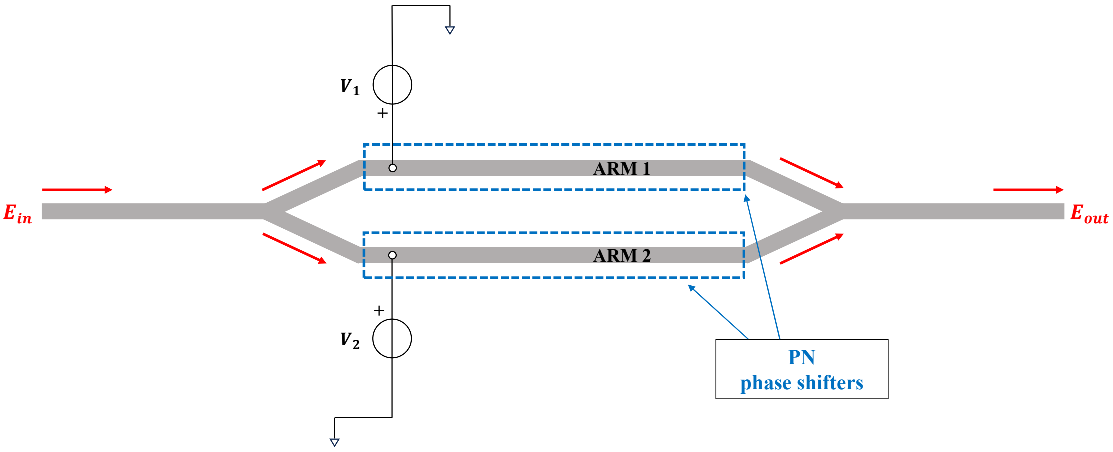

Figure 1.12: Schematic representation of a MZM.

1.4.3 Si-Ge photodetector

Photodetectors are essential components in photonic integrated circuits given their role as opto-electro converters. In SiPh PICs one of the most promising candidates are waveguide-integrated germanium-on-silicon p-i-n photodiodes (Ge-on-Si PDs), where Ge is employed as absorber layer thanks to its strong absorption in the O-band and C-band telecommunication wavelengths [45].

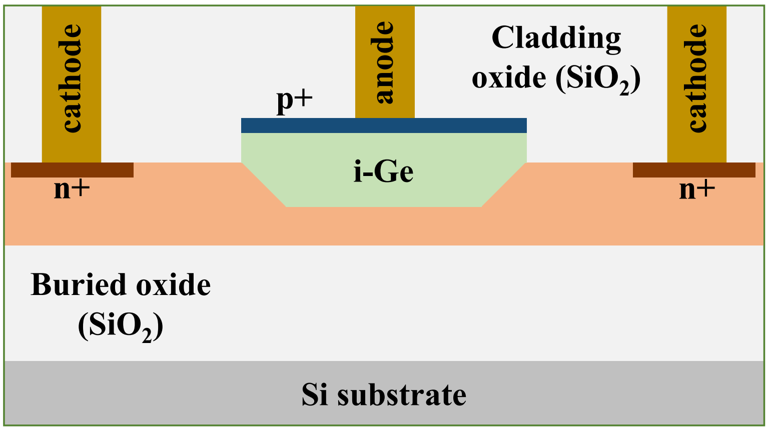

Figure 1.13: Cross-section of a VPIN Ge-on-Si PD.

The PDs presented in this work and electrically analysed during the neutron irradiation test are vertical p-i-n (VPIN) photodetectors, where the intrinsic Ge layer is placed above the silicon. Fast transient times and high bandwidth (∼ 50 GHz) are the main advantages of this device architecture [34]. The anode on top of the Ge-absorber generates a strong electric field with low applied bias. However, the metal contact on the germanium layer reduces the responsivity due to light absorption or activates defects at the Si-Ge interface due to high electric fields [17]. The schematic representation of the VPIN PDs cross-section within the PICv2, analysed in this work, is shown in Figure 1.13.

This family of devices has already been characterised for PICv2 in previous studies, during which they have been exposed to high proton and neutron fluences [34] as well as X-ray radiation [54], [27]. It has been showns that the responsivity of Ge-on-Si photodiodes is not appreciably affected by Total Ionising Dose (TID). Conversely, displacement damage is identified as the principal source of degradation. In this work, the results of current-voltage characteristics for this type of device under very high levels of neutron fluence will be presented, showing the effects of displacement damage on the macroscopic electro-optical characteristics.

Chapter 2

Neutron Irradiation Test

2.1 Purpose

The irradiation test presented in this chapter was conducted to characterise different SiPh components within the PICs, in order to acquire a good statistics on the device performances when irradiated up to a high neutron fluence.

For the first time, we conducted simultaneous testing on various devices with different neutron fluxes, since the PICs under test were placed at different distances from the neutron beam. The experiment aimed to establish whether the irradiation response of the devices was flux dependent. This was also the first use of this experimental setup including a tunable LASER and an electrically driven polarisation controller (EPC). To obtain accurate data on the electro-optic response of the devices, fast and reliable data acquisition was required, and this was the aim of these two instruments.

In Section 2.4, it will be shown that the employed setup facilitated numerous data acquisitions during irradiation, enabling a clear observation of device responses to neutron irradiation. During the irradiation test, various devices were kept at different temperatures, ranging from room temperature (RT) to higher temperatures using RM micro-heaters. The analysis focused on investigating the possible effects of distinctive temperature conditions on the device's responses to neutron irradiation.

2.2 PIC under test

The second version of the SiPh PIC developed at CERN presents many devices with several characteristics, based on different geometrical designs or doping concentrations. Based on the results of previous irradiation tests, only the most relevant components were selected for each chip, by choosing the most radiation-hard devices or those that required further investigation. In total, 14 devices were measured on each chip: 1 Mach-Zehnder Modulator (MZM), 8 Ring Modulators (RMs) and 4 Si-Ge Photo-Detectors (PDs). Each device is classified within the chip with a specific numerical label and a schematic of the location of the Devices Under Test (DUTs) is reported in Figure 2.1b.

Aluminium electrical pads are connected to the tracks of the printed circuit board (PCB) by means of gold wire bonding. The aluminium pads are connected to the devices via copper metal lines in the Back-End of the Line (BEOL) of the PIC. The wire bonding of all devices in the external part of the PIC is visible in the left-hand side of Figure 2.1a. On the left-hand side of Figure 2.1b are also shown the IN/OUT Grating Couplers (GCs) related to the corresponding waveguide. The single-mode fibres are connected to the PIC through grating couplers, as shown in Figure 2.1c. The PIC under test is passive, thus the LASER source is external. Figure 2.1a shows a complete picture of the PCB with the PIC in the centre.

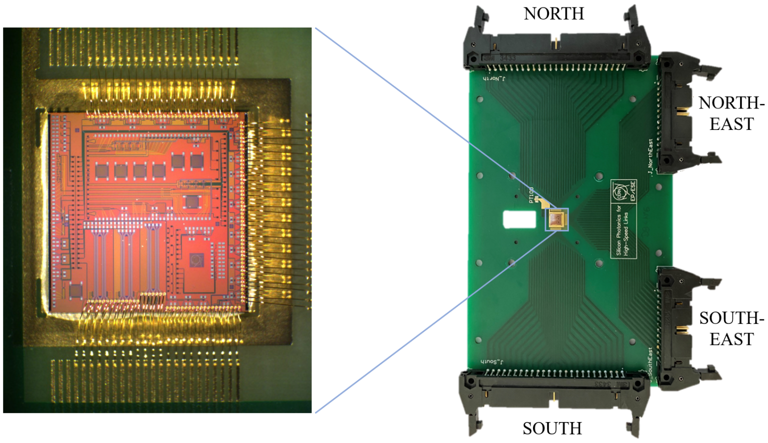

(a) *PIC on the PCB with gold wire bonding. In this picture is missing the ribbon of single-mode fibres attached through grating couplers.*

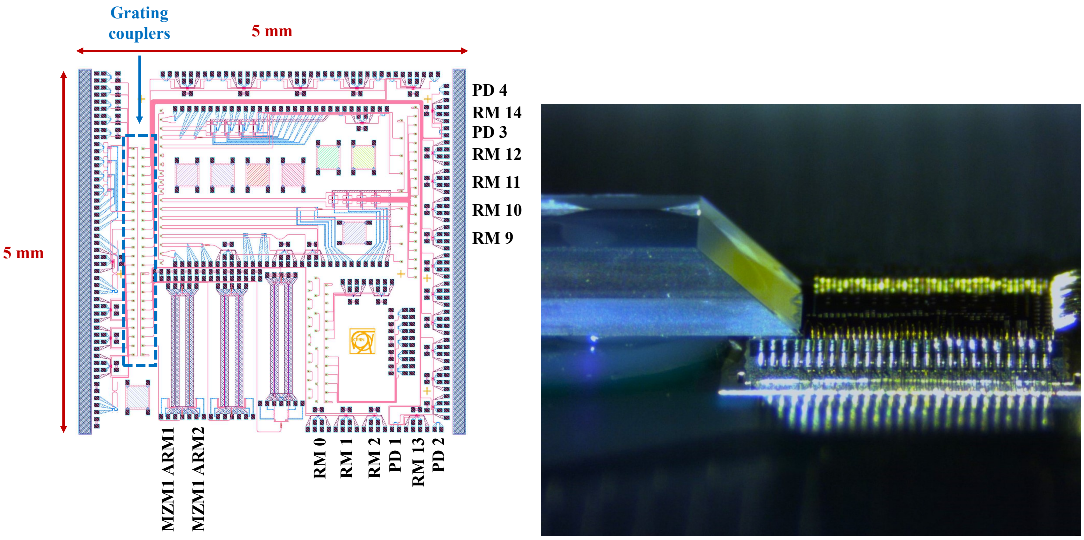

(b) *DUTs within the PICv2.*

(c) *Fibre coupling.*

Figure 2.1: (a) PIC on the PCB with gold wire bonding, (b) DUTs location within the PICv2, (c) fibre coupling.

The 14 DUTs selected per each PIC only come from two connectors: 'SOUTH' and

‘NORTH-EAST’. However, not all devices coming from these connectors were actually tested, thus different routing boards were required to effectively select only the desired DUTs.

The PIC is manufactured using standard CMOS processes, with electrical access to the devices, including the RM phase shifter, via copper metal lines in the BEOL of the chip. Because the ground plane on the PCB is common to all devices within the same PIC, leakage currents from non-tested devices can interfere with the device being measured. This phenomenon presents a particular problem when analysing small currents. Section 2.3 explains how this was taken into account in the experimental setup.

The devices that were tested within each PIC are listed in Table 2.1. The DUTs were tested at different temperature conditions, ranging from RT to higher temperatures. The RM temperature was set by the tungsten micro-heaters on top of them.

DUTs within a single PIC	**Temperature range, [°C]**	**RM radius, [µm]**
MZM1 ARM1	RT	-
MZM1 ARM2	RT	-
RM 0	70 - 85	5
RM 1	105 - 125	5
RM 9	RT	5
RM 10	70 - 85	5
RM 11	75 - 85	7.5
RM 12	RT	7.5
RM 13	100	5
RM 14	RT	5
PD 1	RT	-
PD 2	RT	-
PD 3	RT	-
PD 4	RT	-

Table 2.1: List of the DUTs within a single PIC. In red the RMs with the micro-heater biased.

The PICs underwent testing under varying neutron fluxes, resulting in a range of maximum neutron fluence levels. Table 2.2 presents the list of three PICs that were irradiated. The table shows the different fluxes to which the PICs were exposed and the maximum neutron fluence reached.

	Neutron flux, [neutrons/s·cm^2]	**Maximum fluence, [neutrons/cm^2]**
PIC 1	$11.3 \cdot 10^{14}$	$3.8 \cdot 10^{16}$
PIC 2	$5.9 \cdot 10^{14}$	$2.0 \cdot 10^{16}$
PIC 3	$4.0 \cdot 10^{13}$	$1.5 \cdot 10^{15}$

Table 2.2: Irradiated PICs with corresponding neutron flux and maximum neutron fluence reached.

2.3 Experimental setup

The neutron irradiation test of the SiPh PICs developed at CERN has been carried out at the Université catholique de Louvain (UCLouvain), Belgium. The Cyclotron Resource Centre (CRC) hosts a facility with a cyclotron where a 50 MeV deuteron beam impinges on a beryllium target, initiating the $^{9}Be(d,n)^{10}B$ reaction. The peak of the energy distribution of the neutron beam is centred at 23 MeV, as shown from Figure 2.2.

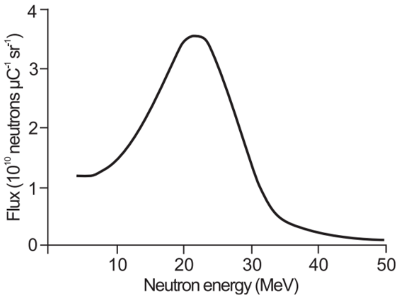

Figure 2.2: Neutron beam energy distribution, from [48].

The deuteron beam was turned on at 9:41 AM on Thursday 22nd of June 2023, and it continuously irradiated the beryllium target until the end of the test at 20:21 PM on Friday 23rd of June, for a total irradiation time exceeding 34 hours.

The experimental setup was designed to assess the optical spectra of the devices while concurrently evaluating their electrical figures of merit. We were interested in DC measurements of current-voltage characteristics of DUTs both in forward and reverse bias. A schematic of the final experimental setup is shown in Figure 2.3.

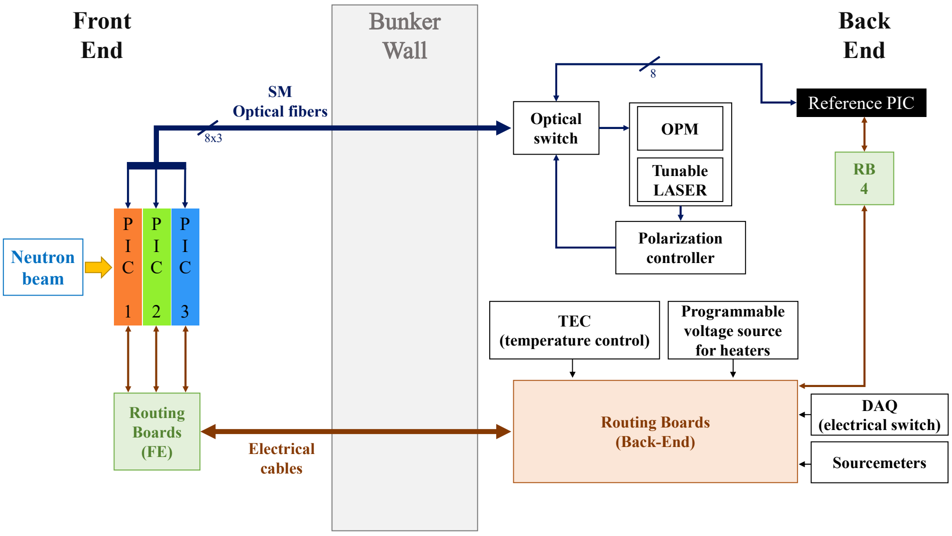

Figure 2.3: Schematic of the experimental setup.

The neutron source is located in a specific bunker where the deuteron beam comes from a branch of the cyclotron. The experimental setup has then been subdivided into two different locations: the Front-End (FE) room, where the PICs were irradiated, and the Back-End (BE), where all the instruments and PCs were kept in a radiation-free environment. In total, the experiment involved four PICs, three located in the FE irradiated by the neutron beam and one in the BE which was taken as reference. Starting from the FE, the PICs were located in a rack parallel to the neutron beam, at different distances from the beryllium target in order to analyse the PICs irradiated with different fluxes. The devices were connected to the BE using electrical cables and single-mode optical fibres (around 30 metres long). Routing boards were designed for the selection of the desired DUTs within the PICs and to establish the instrument connections. A parallel setup was also used for the reference PIC in the BE, using the same routing boards and the same length of cables, in order to obtain comparable measurements.

In Figure 2.4 is shown the final experimental setup for the neutron irradiation test, together with the PCBs installed in the rack.

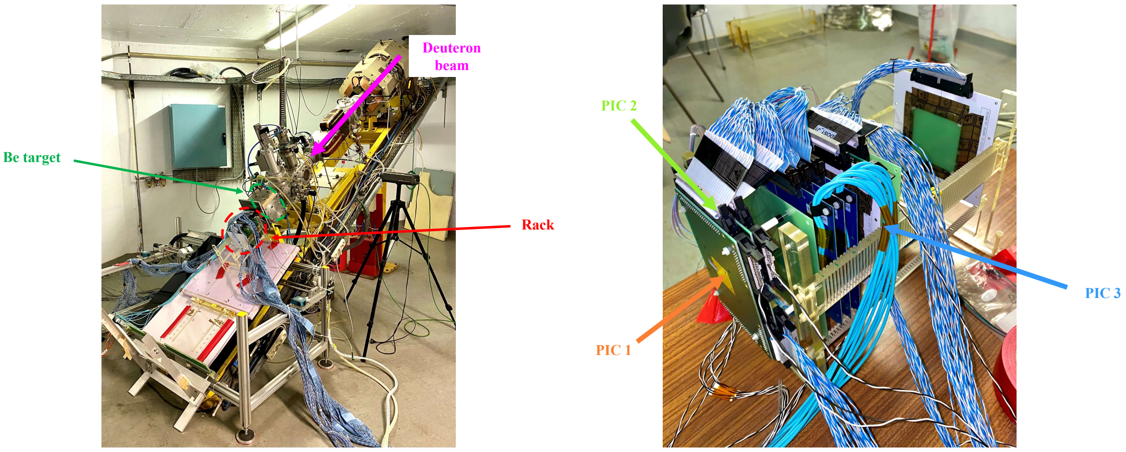

(a) *Neutron source.*

(b) *Rack before installation.*

Figure 2.4: Final experimental setup in the FE, with the rack (b) and the branch of the cyclotron that irradiates the Be target to initiate the reaction (a).

The software used to control the instruments, monitor the test in real-time and post-process the results was IGOR Pro by WaveMetrics. The measurement loop was realised to acquire current-voltage characteristics and optical spectra. A more detailed description of the algorithm developed for this test is reported in Appendix A.

2.3.1 Electrical setup

The acquisition of static current-voltage characteristics was realised by means of two sourcemeters, named respectively 'V_meas' and 'V_idle'. The sourcemeters were used both as voltage sources and for current measurements. As mentioned above, grounding was common for all the devices; therefore, to avoid the undesired leakage of currents, two voltage sources were used. The voltage applied to the DUT is 'V_meas', while all the other untested devices are connected to 'V_idle'. The two voltages are incremented together and kept equal for the first part of current acquisition; in this way, the leakage currents from other devices are reduced, and the response of the selected DUT can be properly analysed. Since all 14 devices selected for the irradiation test are basically PN junctions, we can let 'V_idle' fix and increment only 'V_meas' as soon as the DUT reaches the conduction region (or in proximity of the breakdown for reverse bias), that is, when the current of the measured device becomes dominant with respect to leakage currents. The limits for idle voltages were established by means of laboratory tests before the neutron irradiation experiment. Figure 2.5 shows an example of a current-voltage acquisition for a device under test (RM 0 in the example) and the voltage range over which 'V_idle' was incremented together with 'V_meas'.

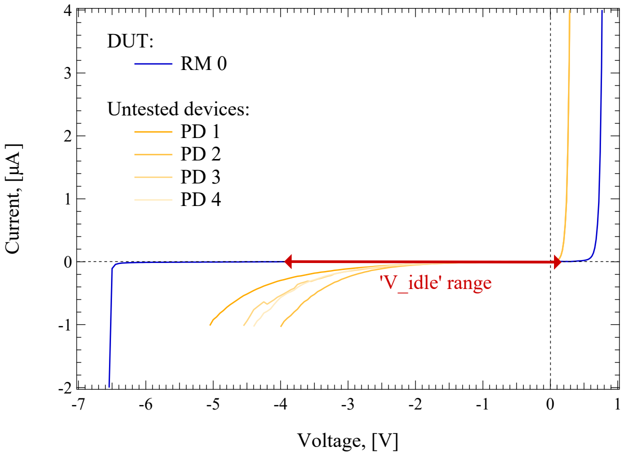

Figure 2.5: Example of pre-irradiation acquisition of the current-voltage characteristic of RM 0. The idle voltage is increased according to the measurement voltage in the depicted range, applied to all untested devices. The I-V characteristics of the untested PDs are also displayed to highlight the limitations of the idle voltage range.

The primary constraint on the idle voltage range is attributed to the PDs, which exhibit substantially lower breakdown or threshold voltages compared to RMs or MZMs. Additionally, it should be mentioned that the illustrated range is applicable solely to the pre-irradiation measurements, as neutron irradiation is anticipated to result in a change in the devices' current-voltage characteristics. The measurement loop utilised during the test was capable of adjusting the voltage limits based on the previous set of measurements. As a result, an active control analysis was conducted throughout the entire test. The selection of the DUT is performed by means of a Data Acquisition/Data Logger Switch Unit (DAQ) with 3 slots and 20 channels each. By sequentially closing the DAQ channels, we connect the DUT to 'V_meas' and let all the other devices at 'V_idle'.

An independent programmable voltage source was used to set the temperature of the heaters. For example, each RM's phase shifter is designed to have a resistive tungsten micro-heater on top of the rib waveguide, which can be heated up by Joule effect and inducing the shift of the characteristic resonance wavelength. The thermo-optic coefficient of Si allows an efficient variation of the refractive index and the shift in the resonance wavelength is almost linear with temperature, with a shift variation of 70 pm/°C and heating efficiency of about 4 °C/mW [28]. Each PCB has a built-in PT100 sensor, which is a common Resistance Temperature Detector (RTD) or resistance thermometer. The PT100 sensors of the PICs situated in the FE were used to monitor the temperature within the bunker. Additionally, the reference PIC in the BE was connected to a Temperature Controller (TEC) and maintained at the same temperature as the chips in the FE by using Peltier elements.

Two different sets of routing boards were developed, one for the FE and another for the BE, as shown in Figure 2.6. The former were designed for DUT selection, discarding the untested devices within the PIC, while the latter managed the instrument connections.

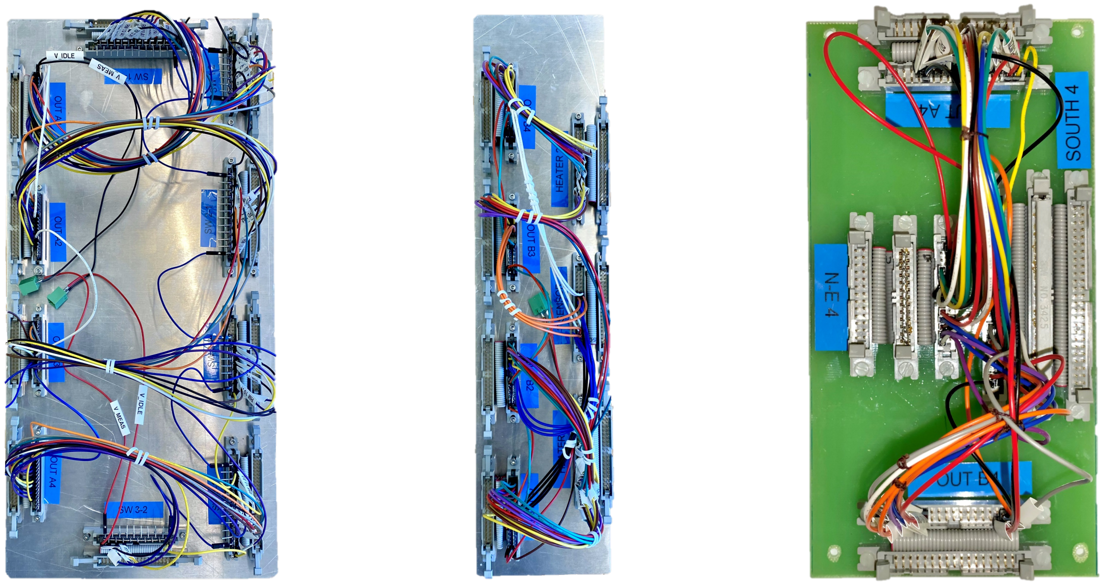

(a) *Routing board A - BE*

(b) *Routing board B - BE*

(c) *Routing board - FE*

Figure 2.6: Routing boards designed for the irradiation test. (a), (b) routing boards for the BE, used for for instrument connections, (c) routing board for the DUT selection within the PIC; there were one routing board of this type for each PIC.

2.3.2 Optical setup

As already mentioned, the single-mode fibers are connected to the PIC thorugh grating coupling. Four optical channels were analysed for each PIC, resulting in a total of 16 channels. An optical switch was used to select the desired optical channel under test. A schematic representation of the four optical channel tested within one PIC is shown in Figure 2.7.

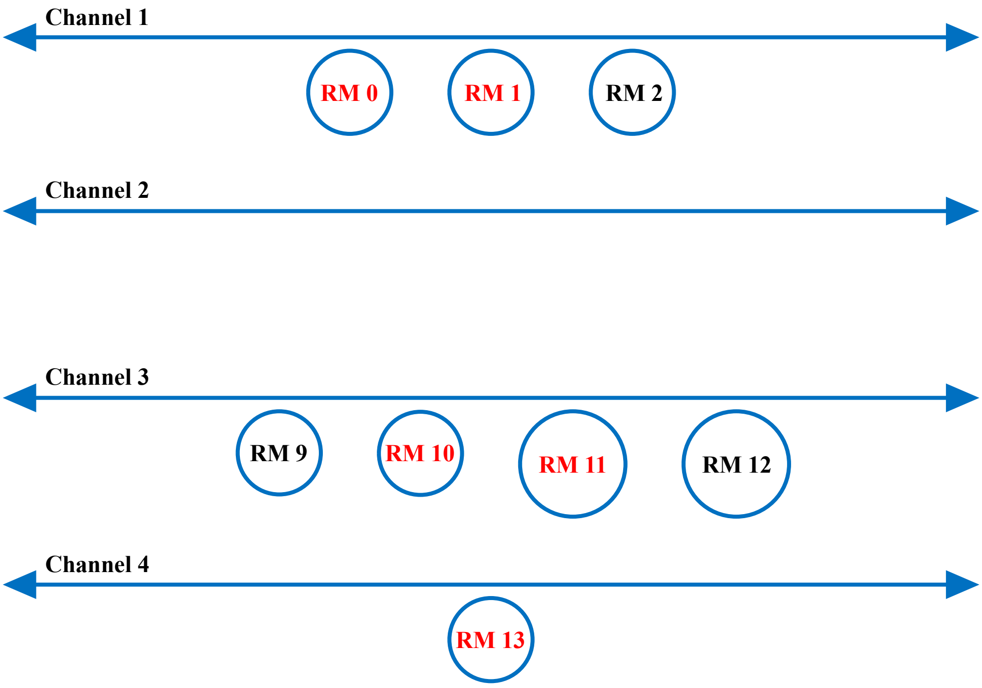

Figure 2.7: Schematic representation of the four optical channels tested within one PIC. Each waveguide can hold a bus of RMs, while the second channel is a shunt waveguide. The optical channels begin and end with grating couplers. In red, the RMs with the micro-heaters biased.

Each optical channel can hold a bus of RMs. For instance, the first and third waveguides of each chip contain several RMs, while the fourth has only RM 13 and the second is a shunt. The importance of the heaters is evident, as there can be RMs of similar resonance wavelengths in the same waveguide. Therefore, micro-heaters are crucial in separating different resonance peaks within the optical spectrum.

Biasing of the heaters was carried out prior to the irradiation test. Subsequently, the resonance wavelength of each RM was computed both before and after activating the micro-heater. Considering the thermo-optic shift of the resonance wavelength of 70 pm/°C the temperature of the tungsten heater was calculated with respect to the room temperature (RT). Concerning the fourth waveguide, with only RM 13, there were no constraints regarding the heating nor the resonance shift, then it was decided to evaluate the response of the RM at high temperature of 100 °C. This was interesting because it was the only RM that could be kept at the same high temperature throughout the entire irradiation test and for all four chips. Only the micro-heaters of five RMs were electrically connected, specifically the ones of the RMs highlghted in red in (2.7). The voltage range applied to the micro-heaters goes from 0.8 V to 1.35 V.

The optical spectra were acquired by means of a tunable LASER in the C-band and a built-in optical powermeter (OPM). The emission wavelength of the LASER can be tuned and a sweep over a certain wavelength was performed, that in this test went from 1520 nm to 1580 nm. The optical spectrum was then reconstructed by merging the tunable LASER's emission wavelength with the OPM's optical power measurement. To evaluate the modulation properties of the rings, different voltages were applied to the RMs' phase shifter (0.5 V, -0.5 V, -1 V, -2 V) and each time the optical spectrum was acquired.

Light polarization control is fundamental to limit Polarization-Dependent Loss (PDL) in single-mode fibers, therefore an electrically driven polarisation controller (EPC) was inserted in the test loop. The EPC provides up to four actuators that can be independently DC tuned by applying a voltage range from -5 V to 5 V. The controller uses a magnetically driven fiber squeezing technique, i.e. single-mode optical fibers are squeezed by electromagnetic actuators that allow the control of the state of polarization by changing the birefringence [26]. The set of four voltages applied to the polarisation controller that maximise the optical power were regulated by a control loop in the code each time a different optical channel was scanned. In Figure 2.8 is shown the normalised optical power for the four optical channels of the reference PIC, in the post-irradiation period. As it can be observed, the overall variation remains below the ±10% during the 17 days of measurements, confirming the stability of the polarisation controller.

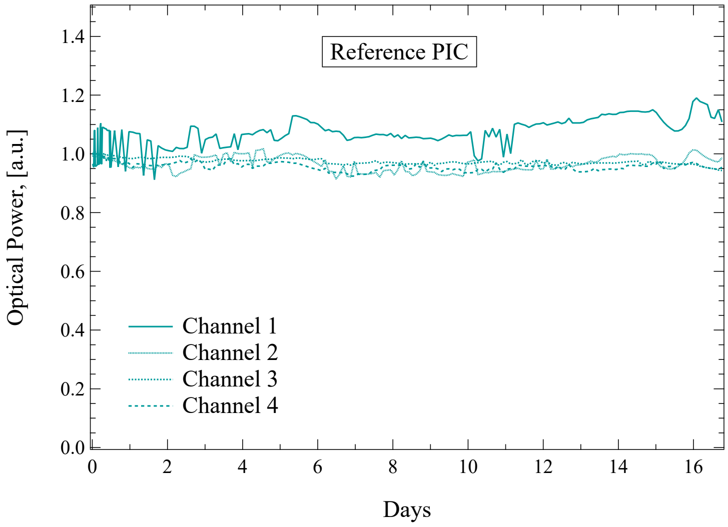

Figure 2.8: Normalised optical power for the four optical channels of the reference PIC in the post-irradiation measurements.

2.4 Experimental results

The total irradiation time was approximately 34 hours, then the experiment was not interrupted and data acquisition continued for 17 days, performing a measurement cycle every two hours, while during the irradiation the acquisition was continuous (this should be remembered when looking at post-irradiation data). This was necessary to evaluate if there was a recovery in the DUT response without modifying the setup. The high amount of data was then post-processed and the electro-optic FOMs were extracted. The reported plots are shown considering three different conditions:

- Pre-irradiation
- Irraditaion
- Post-irradiation

For what concerns the irradiation data, they have been evaluated as a function of the fluence. In this neutron irradiation test, a maximum neutron fluence of $3.8 \cdot 10^{16}$ n/cm^2 has been reached. These are the highest fluence levels these PICs have ever been exposed to. The fluence (Φ) was calculated from the flux of the neutron beam, that is related to the measured deuteron current I and to the distance from the target d according to the following equation [48]:

$$\Phi(t,d) = \int_{t_0}^{t} I(\tau)\,\mathrm{d}\tau \times \frac{1 \times 10^{14}}{0.079 \cdot d^{1.902}} \tag{2.1}$$

The current of the deuteron beam was monitored during the irradiation test and remained stable, as shown in Figure 2.9.

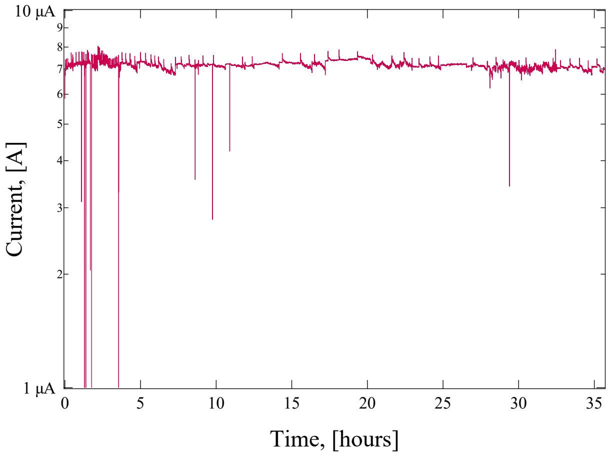

Figure 2.9: Deuteron current during the neutron irradiation test.

2.4.1 Electrical measurements

The current-voltage (I-V) characteristics were acquired for all the 14 devices tested, including MZMs, RMs and Si-Ge PDs. In particular, more attention was paid to RM 0, which is the reference design and will also be adopted for the next PIC generation. From the I-V characteristics, different analysis can be conducted to extract some interesting electrical FOMs which aid in device characterisation. All DUTs can be described as diodes with unique characteristics based on the respective device. A description of the DUTs was reported in Section 1.3. Both forward and reverse biases were measured and the data were post-processed following the procedure described in Appendix B.1. The electrical FOMs demonstrate clear variation with increasing fluence, indicating damage induced by the neutron irradiation. The reference PIC, on the other hand, preserves a good stability. The most relevant parameters for describing the diode and its characteristics are threshold and breakdown voltages. The latter was specifically examined during this test as it can help to comprehend the effects of neutron irradiation. The aforementioned FOMs are reported in Figure 2.10 for RM 0.

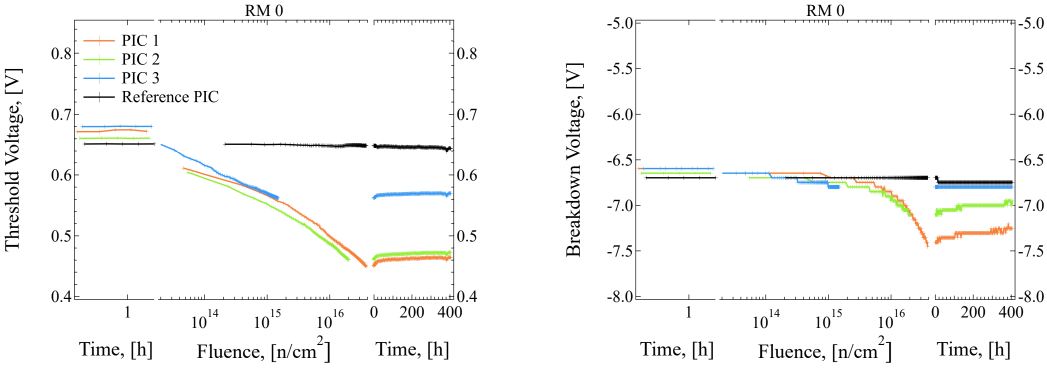

(a) *Threshold voltage.*

(b) *Breakdown voltage.*

Figure 2.10: (a) Threshold voltage and (b) breakdown voltage of RM 0.

Figure 2.10b shows a certain step-wise profile for the reported FOMs. The explanation of this trend is reported in Appendix B.1, together with the metod used for data post-processing.

The threshold voltage of the RM phase shifter decreases with neutron irradiation and similar trends can be observed for the three irradiated PICs. With respect to the threshold, the breakdown voltage does not begin to decrease immediately following neutron irradiation. Instead, a fluence greater than $1{\cdot}10^{15}$ n/cm^{-2} is actually required to observe a significant reduction. The first explanation to the observed outcomes can be attributed to the donor/acceptor removal mechanism, as described in literature. This phenomenon impacts the efficacy of silicon detectors for HEP and is evident at elevated levels of proton or neutron irradiation [40],[29],[30]. When fast particles at high fluence levels irradiate doped silicon, as is the case in this test with high-energy neutrons (with a peak mean energy distribution at 23 MeV [48]), collisions with the crystal lattice cause displacement damage, leading to a general deactivation of the dopant atoms. The microscopic origin behind this mechanism is not yet comprehensively understood. Nevertheless, one suggested hypothesis is that ion-dopant complexes of varying types can be generated because of irradiation, which ultimately causes a decrease in the effective doping concentration [22].

The displacement of boron atoms from a substitutional site in crystalline silicon can be induced by proton irradiation [36]. The displacement is mainly generated by Si self-interstitials (I_{Si}) generated in the lattice by proton beam. The I_{Si} defects are generated by high-fluence proton irradiation and can interact with boron atoms to form B-I_{Si} couples. The displacement of boron atoms increases exponentially with irradiated fluence, reaching a saturation point. This process can result in the deactivation of dopants, ultimately leading to a reduction in doping concentration. It is reasonable to assume that the same mechanism can be induced by neutron irradiation. Additional research is crucial to better understand donor/acceptor removal and to explore potential design or annealing solutions.

Neutron irradiation revealed a reduction in both the threshold and breakdown voltages, as well as modifications to the slope of the current-voltage characteristics in these regions as a result of neutron fluence. Both reverse and forward current profiles show reduction in the slope with neutron irradiation. This phenomenon can again be attributed to acceptor/donor removal mechanisms. The effective reduction of doping concentration leads to a decrease in the slope resistance of a diode, meaning that the resistance of the diode after reaching the threshold voltage increases. This can be represented using the piecewise linear model of the diode, where the actual current-voltage characteristic can be approximated using two-segment piecewise linear approximations. As shown in Figure 2.11, with neutron irradiation we observe a reduction of the slope, meaning that the diode resistance in this region increases due to dopant removal mechanism. The presented figure depicts

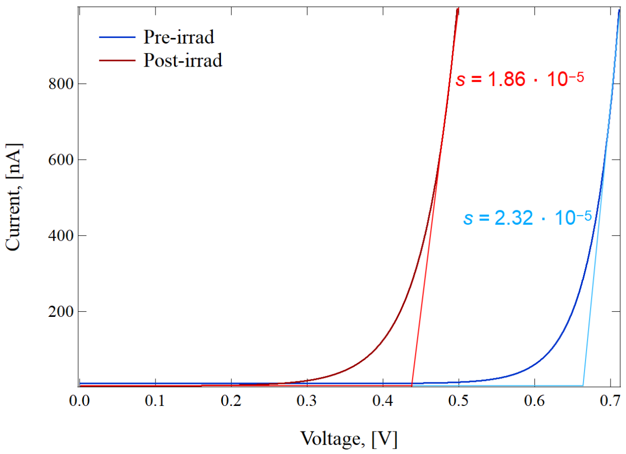

Figure 2.11: Exponential fitting of the current-voltage characteristic of RM 0 for the first PIC, compared with the piecewise linear model of the diode in forward bias. The slope decreases with neutron irradiation, confirming the acceptor/donor removal mechanism and indicating an increase of the diode series resistance.

the exponential current-voltage characteristics of RM 0 in the first PIC at maximum fluence, in comparison to pre-irradiation measurements. The linear piecewise model is used to determine the slope in the linear region beyond the threshold, which corresponds to the inverse of the diode resistance. The diode resistance increases with neutron fluence, beginning from ∼43.1 kΩ prior to irradiation, and reaching an estimated resistance of ∼53.8 kΩ. Future research should further investigate this effect to gain insight into the possible variation of doping concentrations due to neutron irradiation.

Mach-Zehnder modulators were also analysed during the irradiation test. Beside RMs, the design of the MZMs is characterised by a lower doping concentration, almost ten times lower than that of the rings. Consequently, larger voltages are necessary to bring the device into breakdown. The results of MZM 1 are shown in Figure 2.12. The results from the other arm of the MZM (ARM 2) are not shown but they were comparable with the one of the first arm.

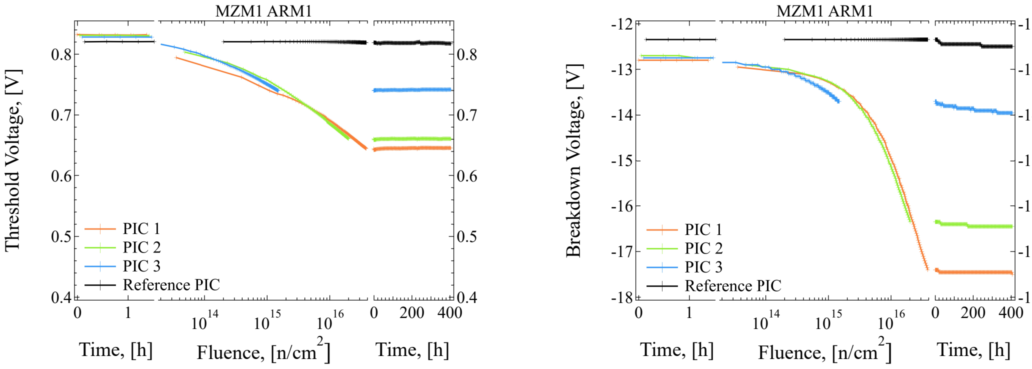

(a) *Threshold voltage - MZM1 ARM1.*

(b) *Breakdown voltage - MZM1 ARM1.*

Figure 2.12: Threshold and breakdown voltages of MZM 1 - ARM 1.

All FOMs underline the effect of neutron irradiation, leading to considerations similar to those stated for RM 0. The decrease in the forward threshold voltage can also be related to several trap states generated by Non-Ionising Energy Loss (NIEL). As a result of irradiating high-energy particles, atoms in the lattice can be displaced and become mobile in the crystal. NIEL is the energy that displaced atoms/ions lose while travelling, creating displacement damage and defects that can act as generation and recombination centres [24],[20]. As a consequence, the voltage needed to bring the junction into the forward conductive region is reduced. It is noteworthy that the shift in breakdown voltage for MZM is significantly greater than that observed for RM 0. The breakdown voltage of MZM starts at approximately -13 V and reaches a value of -17.5 V at the highest neutron fluence. This confirms the acceptor/donor removal mechanism and highlights that the reduction of the effective doping concentration does not decrease when the doping concentration is lowered. No improvement can be observed after the irradiation, but instead a slight decrease in the breakdown voltage is recorded. This contrasts with our findings for RM 0. For example, in the post-irradiation measurements, Figure 2.10b exhibits a very slight recovery of both forward and breakdown voltages. It is worth noting that the high temperature of the RM 0 heater kept the ring at an elevated temperature, whereas the MZM was kept at ambient temperature throughout the test (see Table 2.1).

This suggests that the heaters contribute to the annealing of the devices, while the damage induced by fast neutrons remains largely unchanged without intervention. Consequently, the defects induced by neutron irradiation can be considered to be relatively steady and permanent. Therefore, it is worth analysing different RMs with almost the same design of RM 0 but without the heaters turned off. RMs 9, 12 and 14 were electrically measured throughout the test; RM 9 and RM 14 have the same doping and mainly the same design as RM 0, while RM 12 has a larger radius (7.5 µm) and the same doping concentrations of MZMs. The normalised outcomes for these devices, only for PIC 1, are reported in Figure 2.13, compared with RM 0.

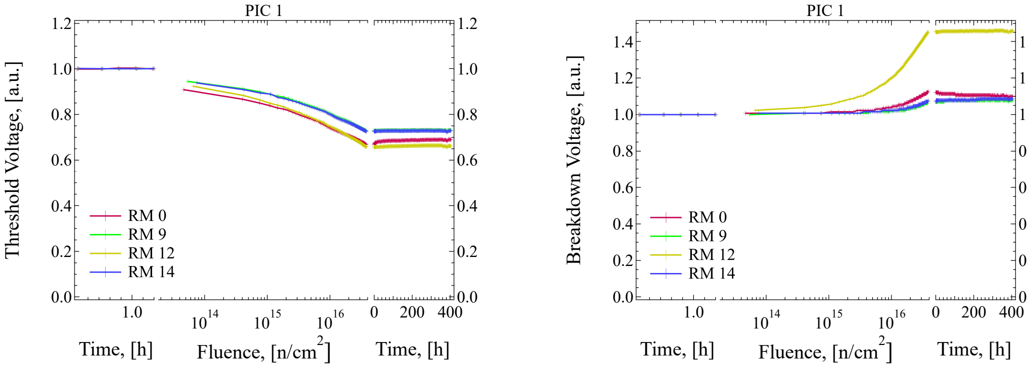

(a) *Threshold voltage.*

(b) *Breakdown voltage.*

Figure 2.13: Threshold voltage and breakdown voltage of RMs 9, 12 and 14 from PIC 1, normalised and compared with RM 0. RMs 9, 12 and 14 they all have the micro-heaters turend off.

The breakdown and threshold voltages of RMs 9, 12 and 14 show no sign of recovery after neutron irradiation. On the contrary, a slight improvement is observed for RM 0, which confirms that the heaters aid in device annealing. However, the recorded recovery is not significant. The observed increase in the breakdown voltage of RM 12 is noteworthy, as it suggests greater sensitivity to neutron irradiation. The introduction of higher dopings helps mitigate the effects of neutron-induced damage. The same FOMs calculated for the other RMs under test are not reported in this work, but similar trends are observed.

For the first time, we extensively evaluated the breakdown of the devices during this irradiation test. Earlier work has shown that the breakdown voltage is shifted to higher values and the swing is increased by neutron irradiation, indicating an increase in linear resistance. Additionally, the shape of the kink in the I-V characteristic of the breakdown current was analysed for the first time. Compared to pre-irradiation measurements, the breakdown kink becomes much smoother with neutron irradiation. This evidence is noteworthy when considering the two primary mechanisms that can cause breakdown in the junction, namely, avalanche generation and band-to-band (B2B) tunnelling [49]. The former induces the breakdown through the collision of a thermally generated electron that has acquired a high kinetic energy with an atom. This process may disrupt the lattice bonding and cause ionisation of the atom, resulting in the creation of an additional electron-hole pair. The pair is then subjected to the same high electric field, thus accelerating and triggering another impact ionisation. The result is an avalanche generation that brings about an abrupt increase in current. The band-to-band tunnelling is a different breakdown mechanism caused by the direct tunneling of an electron of the valence band to the conduction band. When the applied voltage is sufficiently high, the junction barrier is reduced due to the banding of the band edges at the junction. The transmission probability of the highest energetic electrons in the p-side is therefore increased, and tunnelling can occur. A schematic representation of the two breakdown mechanisms is sketched in Figure 2.14.

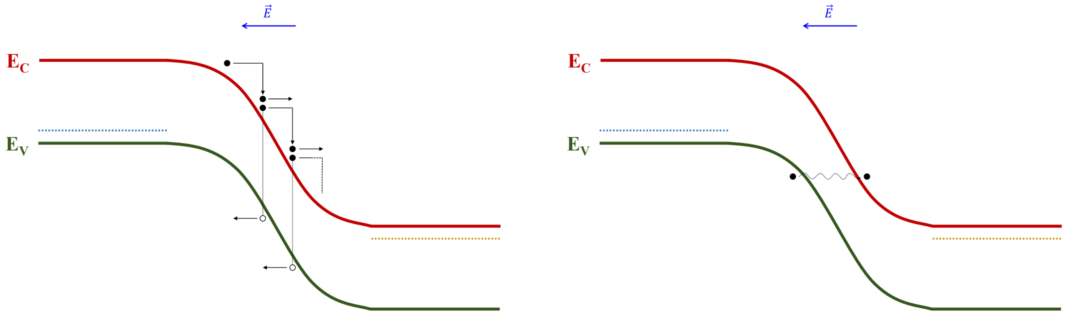

(a) *Avalanche generation by impact ionisation.*

(b) *Direct band-to-band tunneling.*

Figure 2.14: Breakdown mechanisms for the silicon diode in reverse bias.

The breakdown mechanism of a PN junction is directly related to the electric field in the junction; to trigger the B2B tunnelling in a silicon diode, critical electric fields greater than 10^6 V/cm must be reached [49]. This requires either very high voltages applied or high doping concentrations. In the case of RM 0, the doping concentrations found for the rib are greater than 10^{18} cm^{-3} (the analysis of the doping will be extensively described later in Chapter 3). Another characteristic of the two breakdown mechanisms is the shape of the kink in the current. The B2B tunnelling shows a much sharper kink with respect to the avalanche generation, because the amount of carriers that can tunnel will not increase with the voltage applied, but the tunneling will occur as soon as the potential barrier will be sufficiently lowered. Therefore, in this case, the current will gain a sharp increase, while for the avalanche generation the kink will be smoother. This irradiation test had not the aim of understanding the breakdown mechanism, but some interesting considerations can be made by looking at the current-voltage characteristics, since the measurements were performed to increase the acquisition of data points in the proximity of the breakdown.

Figure 2.15 shows the breakdown of RM 0 before irradiation compared to the measurement at maximum neutron fluence.

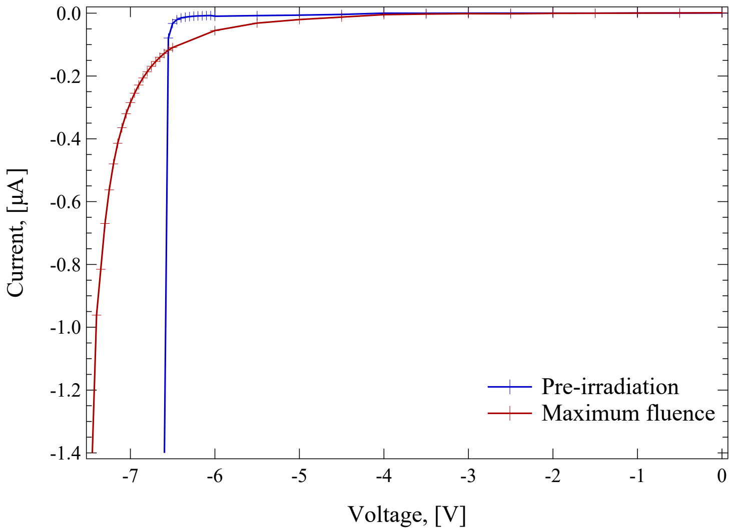

Figure 2.15: Current-voltage characteristic of RM 0 of the first PIC in reverse bias. The pre-irradiation measurements are compared with the data at highest neutron fluence; the breakdown kink shows a smoother profile after irradiation.

In addition to the shift in the breakdown voltage towards higher values, the current kink becomes significantly smoother after neutron irradiation. An explanation for this smoothing could arise from the creation of various defects resulting from irradiation, which subsequently generate different trap states in the silicon band gap. Although the initial current is very sharp, this does not provide sufficient evidence to conclude that the breakdown of this device is due to B2B tunnelling. However, based on these observations, further analysis can provide insight into the mechanism that initially causes device breakdown and how this mechanism changes with neutron irradiation, leading to a possible modelling of the trap states generated in the silicon band gap.

The last type of devices studied in this irradiation test were Si-Ge photodiodes. In this work, only electrical analyses will be conducted on these devices. These photodetectors are based on the vertical p-i-n silicon (Si-VPIN) junction with germanium layer that acts as ligth absorber and the anode is on top of the Ge. We analysed four Si-VPIN photodetectors of the same type, therefore only the results from PD 1 are shown in Figure 2.16.

The photodiodes demonstrate a decrease in the threshold voltage when exposed to neutron irradiation, confirming the same trend observed for RMs and MZMs. However, the breakdown voltage is shifted towards smaller values. Compared to other devices, Si-Ge PDs experience a reduction in the breakdown voltage, indicating that a lower bias is required to bring the junction to breakdown. This would appear to be in contrast to the acceptor/donor removal mechanism discussed previously, but it should be taken into account that PDs have a different junction structure. The effects of displacement damage in intrinsic germanium are not well understood. This region is expected to be not significantly affected by effective dopant deactivation. Thus, it is possible that the

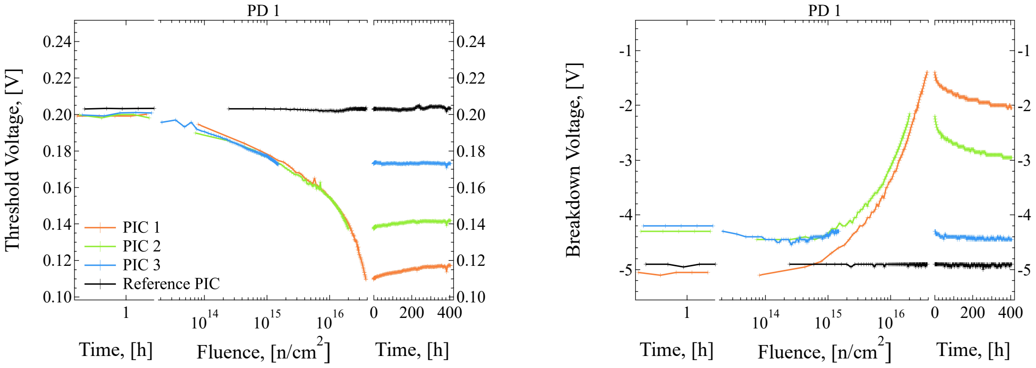

(a) *Threshold voltage - PD 1.*

(b) *Breakdown voltage - PD 1.*

Figure 2.16: Threshold and breakdown voltages of VPIN Si-Ge photodetector with neutron irradiation.

displacement damage will mainly generate different defect species that introduce different trap states. The presence of trap states can decrease the breakdown voltage of the junction. Additionally, the generation of trap states in the Ge absorber could facilitate a potential carrier transport pathway. The band structure of germanium, which has a smaller band gap energy in comparison to that of silicon and a direct band gap in the optical communication range, further supports this scenario.

It should also be noted that the recorded current may not correspond to the breakdown of the PDs, as the experimental acquisition loop was designed to avoid damage to the diodes by high currents; hence, the collection of the current-voltage characteristics was stopped when the current reached 1 µA. Therefore, it is possible that the PD current recorded during neutron irradiation simply corresponds to the increase of the dark current in reverse bias. Differentiation between actual breakdown or a substantial increase in dark current could only have been achieved with a wider acquisition current range, which would have caused damage to the devices.

In summary, the observed trends in forward bias for Si-Ge PDs are consistent with the outcomes of RMs and MZMs. This indicates that the primary mechanism for the current-voltage characteristics of devices in the forward region is the creation of defects due to neutron irradiation, resulting in different trap states. Regarding the reverse bias, it is assumed that the amount of displacement damage with fluence is similar for all the DUTs. The acceptor/donor removal mechanism is the critical factor even if the effect of trap states becomes predominant for very low doping, such as for PDs. Additional studies can be conducted to improve our understanding of the outcomes arising from displacement damage in SiPh components induced by irradiation from high-energy particles.

2.4.2 Optical measurements

Optical measurements were conducted solely on RMs; the four optical channels host a total of 32 RMs, 8 for each PIC. Several FOMs were obtained from the optical spectra, and different analyses of the data were performed. Only the most relevant parameters are presented to avoid redundancy. As reported for the electrical outcomes, a more comprehensive examination will be presented for RM 0. Along with it, other relevant results from other devices are also reported, such as modulators with different doping levels or without the heater turned on. The procedure adopted for data post-processing is based on the subtraction of the grating coupler response from the optical spectra and then on the Lorentzian fitting of the resonance peaks, from which the FOMs were evaluated. A more detailed description of the method is given in Appendix B.2. An example of a raw optical spectrum acquired during the test is shown in Figure 2.17.

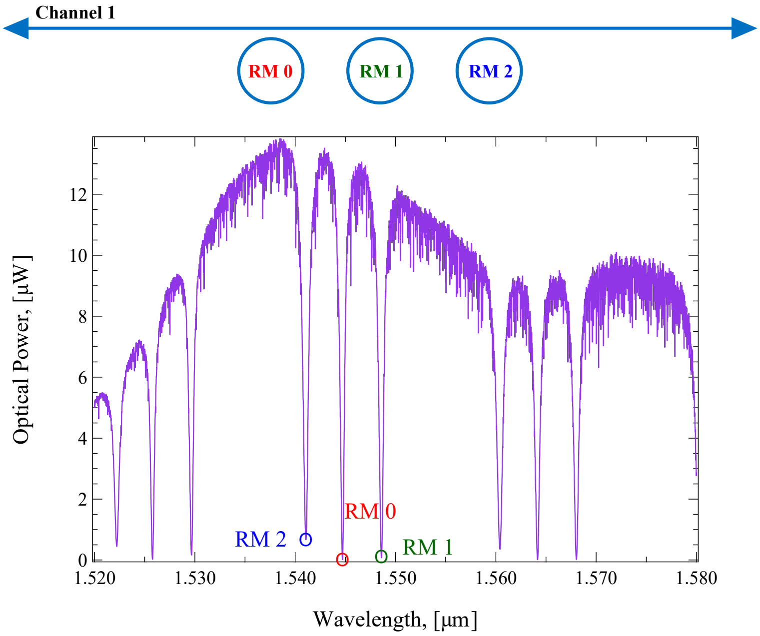

Figure 2.17: Raw example of the acquisition of an optical spectrum. The depicted plot is the optical spectrum related to the first optical channel under study of the PIC, where there is a bus of three RMs (RM 0, 1 and 2). The peaks of the resonance wavelength were adjusted by regulating the heater biasing.

The first relevant FOM that was evaluated is the resonance wavelength of the resonators. Figure 2.18 shows both the value of the resonance wavelength (2.18a) of RM 0 for each PIC and the relative variation of the resonance with respect to the average of the pre-irradiation data (2.18b).

With the neutron irradiation, the resonance of the RM is shifted towards higher wavelengths, as can be seen from the relative variation. The reference PIC shows good stability throughout the entire test. The increasing profile followed by the relative resonance peak agrees well among the three chips as a function of fluence and can be related to the damage

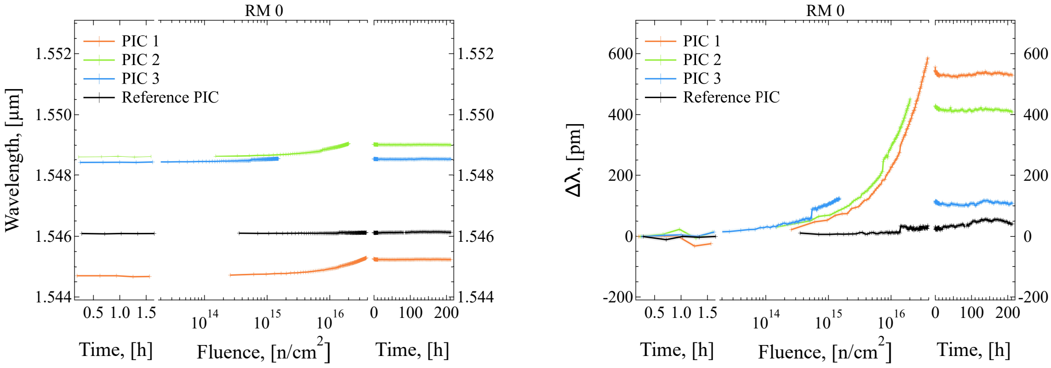

(a) *Resonance wavelength.* (b) *Relative resonance wavelength variation.*

Figure 2.18: (a) Resonance wavelength and (b) corresponding relative variation for RM 0. The variation of wavelength $\Delta\lambda$ was evaluated with respect to the average of the pre-irradiation resonance wavelengths.

induced by the neutron irradiation. According to the resonance wavelength equation (1.4), the neutron irradiation is responsible for an increase in the effective refractive index.

A 3 dB attenuator was used to avoid self-heating of the RMs due to the high input optical power, which would have had an impact on the shape of the resonance peaks. This variation in the optical power will be present throughout the analysis of all experimental results, corresponding approximately to the following fluences:

- $1{\cdot}10^{16}$ n/cm^2 - PIC 1
- $7{\cdot}10^{15}$ n/cm^2 - PIC 2
- $5{\cdot}10^{14}$ n/cm^2 - PIC 3

Nonlinear effects such as free carrier absorption (FCA) and two-photon absorption (TPA) in silicon are relevant when the light power density entering the ring is elevated. Thermal effects are predominant and, with high optical power densities, the resonator shows bistability when the spectrum is acquired with a swept LASER source [14]. The 3 dB attenuator was introduced because a reduction in optical power was expected with neutron irradiation. Therefore, to prevent having a high optical power at the start of the experiment and a low power during the test, the attenuator was removed when the optical power dropped below 1 µW. For the reference PIC, since it was plotted as a function of the maximum fluence like PIC 1, the effect of the removal of the 3 dB attenuator is seen at the same fluence level as PIC 1.

The most relevant parameter that can influence the position of the resonance peak is the temperature, due to the thermo-optic coefficient of silicon; therefore, it is worth pointing out once again that RMs 0 were characterised by the presence of the heaters, as reported in Table 2.1. Therefore, a source of noise that could have affected the experiment is the programmable voltage source used to heat up the micro-heaters, since a slight variation in the bias applied to the tungsten heaters can shift the resonator response; i.e. given the silicon thermo-optic coefficient, a variation of 0.5 ℃ can cause a shift in the resonance wavelength of 35 pm. The temperature of the PICs was monitored throughout the test exploiting the built-in Pt100 thermoresistive sensors and remained fairly stable, as shown in Figure 2.19.

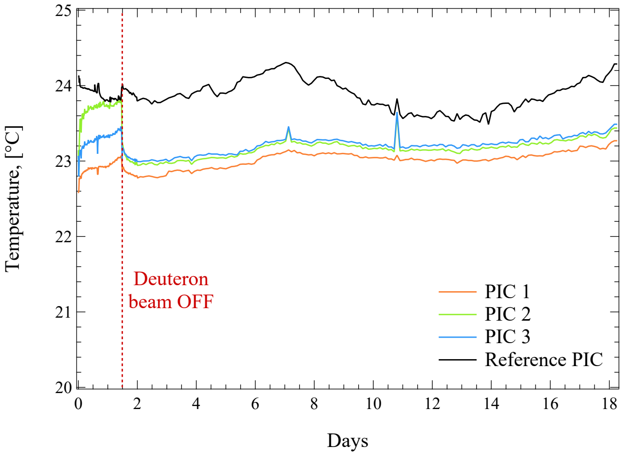

Figure 2.19: Temperature monitoring throughout the test.

The reference PIC was connected to a TEC that regulated the temperature according to the temperature measured in the bunker. Small variations in ambient temperature can be considered slow with respect to the data acquisition. The abrupt drop in the temperature profile for the three irradiated PICs corresponds to the shutdown of the deuteron beam, which occurred after more than 36 hours of testing.

In addition to the variation in the resonance wavelength, it is also worth evaluating how the shape of the resonance peak changes with the neutron irradiation. The FWHM has been extracted from the fitting procedure and is shown in Figure 2.20c. The shaded areas around the curves represent the absolute error of the measurement, which was considered to be the absolute error of the tunable LASER accuracy, corresponding to ±5 pm from the datasheet. The variation in the width profile is not well understood, and further laboratory tests can be carried out to verify the relative variation of this parameter over time. One reason for this could be that the Lorentzian fitting used to evaluate the FWHM is highly dependent on the input power, which is directly related to the response of the grating couplers. Therefore, a variation in the input power or in the grating coupler spectrum can lead to slightly different changes in the overall height and width of the fit. The same profile can be seen from the Quality factor in Figure 2.20d, because it is related to the inverse of the FWHM, as given in (1.8).

Conversely, the FSR in Figure 2.20a increases slightly with the fluence, and this behaviour is particularly accentuated for PICs 1 and 2, i.e. those exposed to higher irradiances, whereas it is less evident for fluences below $1{\cdot}10^{15}$ n/cm^2. The FSR depends directly on the second power of the resonance wavelength, as given in (1.5), therefore an increase

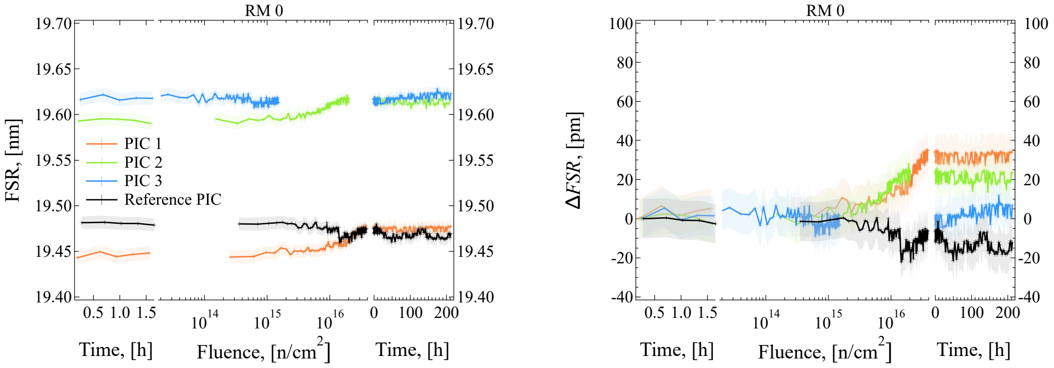

(a) *FSR.* (b) *ΔFSR.*

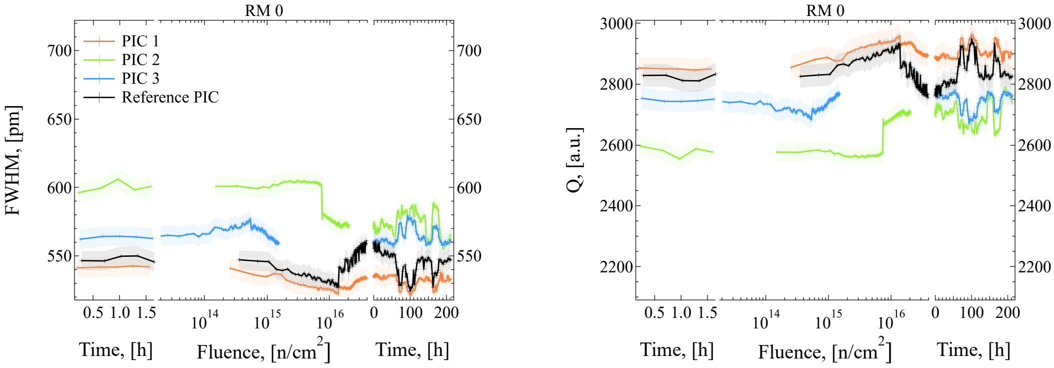

(c) *FWHM.* (d) *Quality factor.*

Figure 2.20: (a) Free Spectral Range, (b) relative FSR variation, (c) Full-Width at Half-Maximum and (d) Quality factor of RM 0. The Quality factor is inversely related to the FWHM and the same profile can be recognised.

in the latter is expected to increase the FSR. The FSR also depends on the group index, which is directly related to the effective refractive index and its dispersion [19], hence further future studies could try to relate the variation of the effective refractive index to the fluence. Together with the FSR, its relative change compared to the values before irradiation is shown in Figure 2.20b to better highlight the increase due to neutron irradiation. Apart from modulating parameters such as ME and TP, all other FOMs vary significantly between the PICs, or at least the variation due to process variation is greater than the total variation induced by neutron irradiation.

As previously noted in the electrical characteristics, there is no significant change in the reported FOMs during the post-irradiation period, which may confirm that the neutron irradiation damage is permanent.

The last two FOMs that are useful in characterising the RM are the Modulation Efficiency (ME) and the Transmission Penalty (TP). The former indicates the strength of

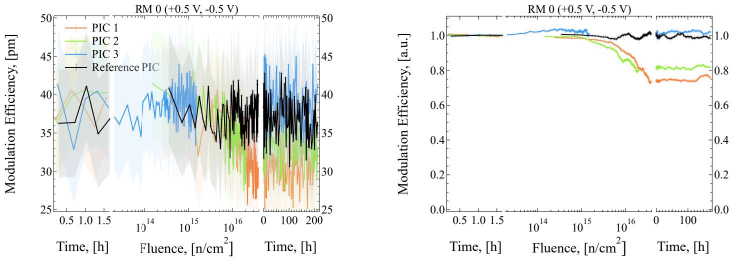

(a) *ME - (+0.5 V, -0.5 V).* (b) *Filtered ME - (+0.5 V, -0.5 V).*

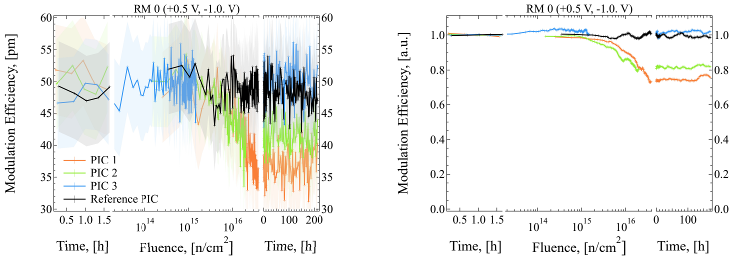

(c) *ME - (+0.5 V, -1.0 V)* (d) *Filtered ME - (+0.5 V, -1.0 V).*

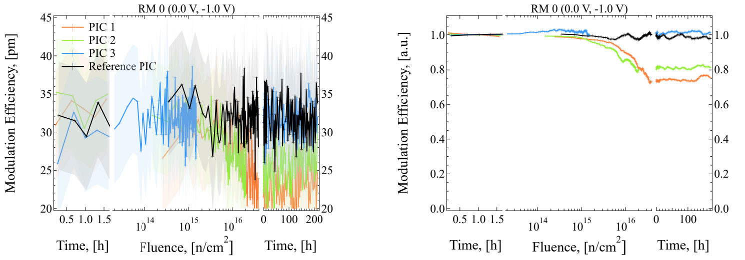

(e) *ME - (0.0 V, -1.0 V).* (f) *Filtered ME - (0.0 V, -1.0 V).*

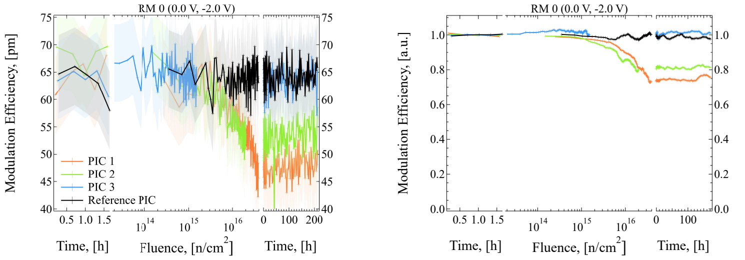

(g) *ME - (0.0 V, -2.0 V).* (h) *Filtered ME - (0.0 V, -2.0 V).*

Figure 2.21: Calculated (left column) and filtered (right column) ME of RM 0 for 4 different voltage conditions.

the modulation when the phase shifter is biased, i.e. it is based on the plasma dispersion effect in the silicon rib. By biasing the PN junction, injection or depletion of carriers results in changes in carrier densities within the rib, which modifies the complex refractive index [33]. This mechanism is widely used to modulate the resonance wavelength of silicon RMs to be used in NZR applications. The ME can thus be evaluated as the difference in the resonance wavelengths when two different voltages are applied. In Figure 2.21 are reported the MEs for four different voltage combinations. The noise coming from the tunable LASER is more apparent considering that the ME is of the order of tens of picometres, therefore filtered and normalised results are shown on the right side of Figure 2.21. A moving average filtering was applied to eliminate short-term variations and emphasise the impact of neutron irradiation. The procedure used for this filtering will be the same for all filtered plots hereafter, considering that all quantities in dB have been linearly scaled prior to normalisation.

There is a general reduction in ME with neutron irradiation, which can be attributed to the donor/acceptor removal mechanism that reduces the effective doping in the rib. The reduction of the doping concentration reduces the strength of the modulation efficiency because less carriers can be injected or depleted. It is interesting to note from the filtered and normalised plots that the degradation in modulation efficiency is independent of the bias range applied to the RM.

It is noteworthy that the ME is worsened by sufficiently high neutron fluences, in fact, the ME of the third PIC remains mainly at the same level as the pre-irradiation results, being consistent with the reference PIC. A similar response was observed in the breakdown voltages of the devices, with only the PICs exposed to the highest neutron fluences showing a significant shift in breakdown voltage. This is also consistent with the measurements made on the other RMs, not all of which are reported in this work.

The transmission penalty is calculated according to (1.14), and the minimum of the TP spectrum is shown in Figure 2.22.

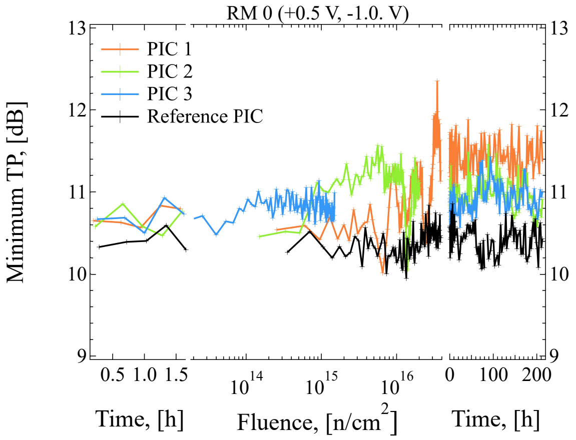

Figure 2.22: Minimum TP of RM 0 for the voltage range (0.0 V, +1.0 V).

The TP of RM 0 is very noisy due to the experimental setup limitations, and a small increase in the minimum TP can be observed with neutron fluence. In general, it is expected that the TP of the RMs should decrease slightly with neutron irradiation due to donor/acceptor removal, because the losses in the silicon rib decrease as the effective doping concentration reduces. This can be observed in other RMs that have been tested whose design has been customized by our team, as shown in Figure 2.23. In particular, RM 13 seems to show the greatest reduction in TP with neutron irradiation.

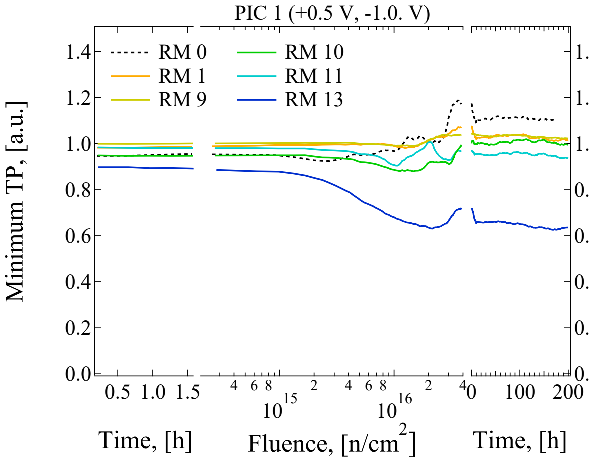

Figure 2.23: Filtered and normalised minimum TP in the voltage range (+0.5 V, -1.0 V) for other RMs under test compared with RM 0. With respect to RM 0, it can be observed a reduction in the minimum TP with neutron irradiation.

Considering all the calculated FOMs among the different RMs under test, we can confirm that the performance of the devices does not appear to be detrimentally affected by neutron irradiation, confirming the radiation hardness of SiPh and its suitability for HEP applications. It is also confirmed that the observed variations are related to the neutron fluence, although the fluxes for the three PICs were different. For this reason, the plots in Figure 2.24 focus on the comparison between the different RMs and do not always show all the extracted results from the irradiated PICs.

Unlike all other devices, RM 12 was the only one tested with lower doping specifications, ten times lower than RM 0 and same doping concentrations of MZM 1. This improves the optical properties of the ring by reducing round-trip losses due to free-carrier absorption and parameters such as Quality factor or ERi are ameliorated. Figure 2.24 shows the parameters calculated for RM 12 from PIC 1, compared to those of RM 0. The resonance peak is steeper due to the lower doping, i.e. the FWHM is also smaller compared to RM 0 (Figure 2.24c). At the same time, lower doping concentrations in the phase shifter reduce optical losses as light circulates through the ring, increasing the Quality factor.

Another interesting comparison can be performed with RM 11, which has a ring radius of 7.5 µm as RM 12, while for the other rings under test is 5 µm. The FSR and FWHM are expected to be smaller for this ring, since they are inversely proportional to the round-trip length (Equations 1.5 and 1.7). This was indeed confirmed by the measurements as shown in Figure 2.24. It can also be noted that the FSR of RM 11 is similar to the calculated

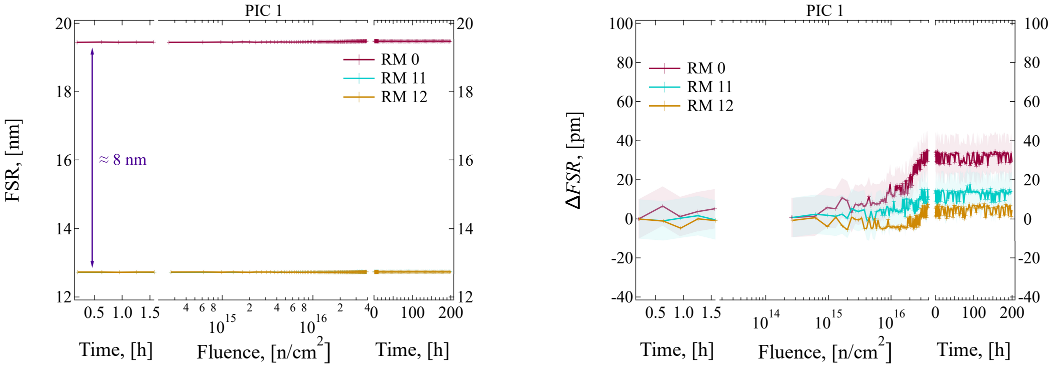

(a) *FSR.*

(b) *ΔFSR.*

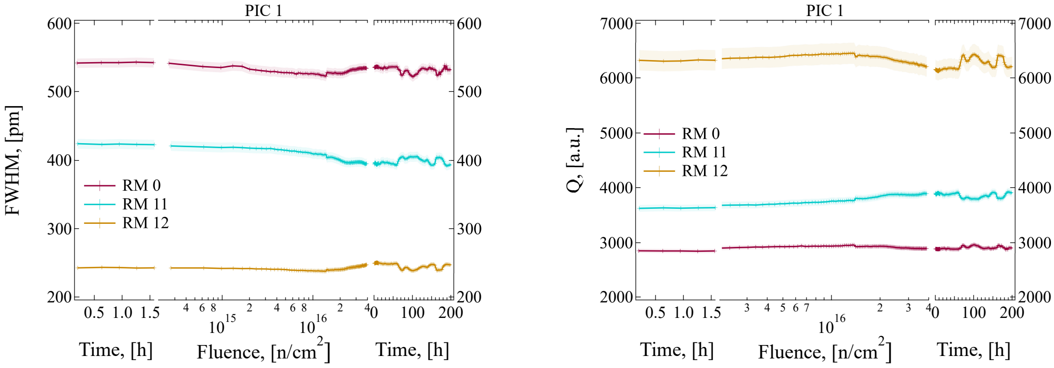

(c) *FWHM.*

(d) *Quality factor.*

Figure 2.24: Optical FOMs for RM 12 and RM 11 from PIC 1, compared with RM 0. In (a), the FSR of RM 11 is very close to that of RM 12 and cannot be clearly distinguished within this scale, but the difference is recognisable in (b).

value found for RM 12. The variation in the FWHM with neutron fluence is different among the rings and does not follow a common trend, therefore, further investigation is required to better understand the effect of neutron irradiation on this parameter.

By reducing the overall doping of the phase shifter, the ME is strongly reduced compared to other rings. When designing a PIC, it is important to find the right compromise between optical losses and modulation efficiency of the RMs. From Figure 2.25 can be seen that the ME is much smaller than RM 0, starting from pre-irradiation values around 20 pm. The reduction due to irradiation seems to be of the same order as for the other RMs, with an estimated decrease of ≈15 pm for a fluence of $3.8{\cdot}10^{16}$ n/cm^2, in the bias range (+0.5 V, -1.0 V).

In summary, the neutron irradiation test provided the opportunity to obtain a large number of statistics on the FOMs, useful for characterising the ring modulators. The parameters of both resonator and modulator were extracted and used to evaluate the

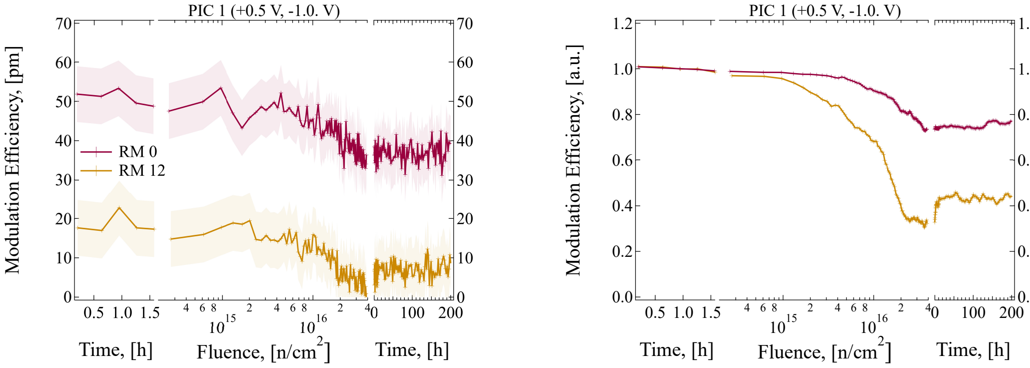

(a) *ME - (+0.5 V, -1.0 V).*

(b) *Filtered ME - (+0.5 V, -1.0 V).*

Figure 2.25: Calculated (a) and filtered (b) ME of RM 12 (low-doping) from PIC 1, compared with RM 0 for voltage range (+0.5 V, -1.0 V).

different design specifications among the rings. The performance of the RMs does not seem to be adversely affected by the neutron irradiation and there are good expectations for the optimal operation of these SiPh devices in HEP applications. The resonance wavelength is shifted to higher values with radiation, but the variation of other parameters such as FSR and Quality factor are not considered threatening for the final device operability. Regarding the modulator FOMs, the ME is degraded by the neutron fluence, with an observed decrease of the total ME in all the voltage ranges, while the TP seems to be slightly improved thanks to the acceptor/donor removal mechanism induced by irradiation. As a final comparison, in Figure 2.26 are shown the MEs of all the ring modulators under test (excluding RM 12, which had lower doping concentrations) as a function of the neutron fluence. It can be seen how this parameter decreases with irradiation and how this effect is consistent for all PICs and all RMs tested.

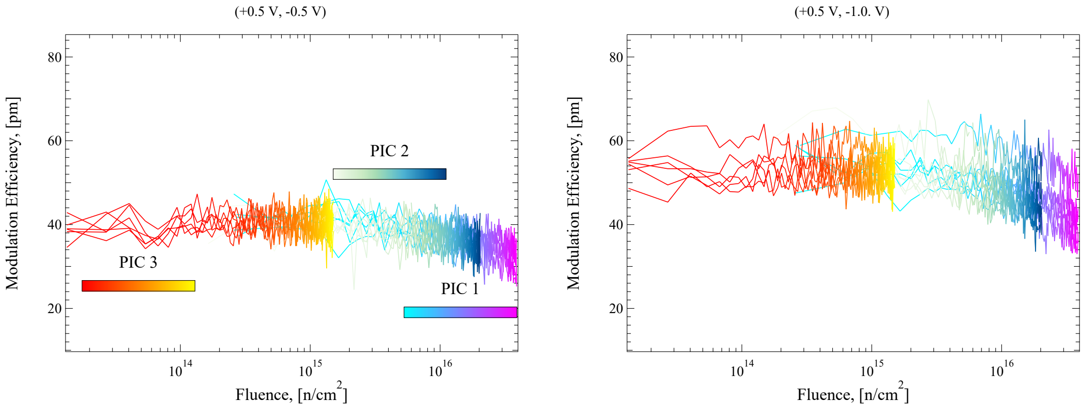

(a) *ME - (+0.5 V, -0.5 V).* (b) *ME - (+0.5 V, -1.0 V).*

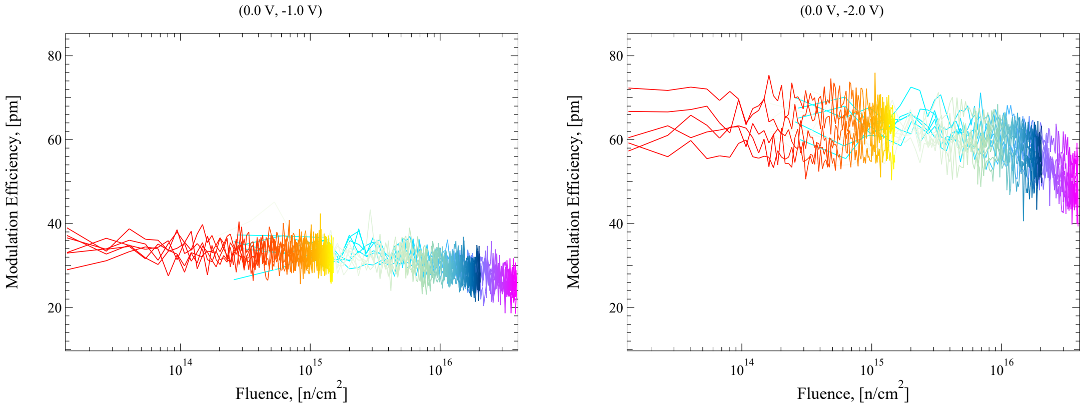

(c) *ME - (0.0 V, -1.0 V).* (d) *ME - (0.0 V, -2.0 V).*

Figure 2.26: Modulation efficiency in the four voltage ranges for all RMs and all PICs as a function of the neutron fluence. The followed trend is common for all RMs tested.

Chapter 3

TCAD Simulation

Neutron radiation damage has been shown to alter both electrical and optical responses of the devices. A simulation was developed to emulate the effect of neutron irradiation on the RM phase shifter. The tools provided by the Synopsys® Sentaurus$^{\text{TM}}$ TCAD software package were first used to simulate the fabrication process of the phase shifter to obtain a good match of the current-voltage electrical characteristics of the unirradiated device; then, various physical models were implemented to simulate the damage induced by neutron radiation. This work focuses on the electrical simulation of the device and on the corresponding variation on the current-voltage characteristic induced by irradiation damage; future works can start from the following results to also analyse the optical spectra and the variation of the FOMs characterising the RM. The following will focus on simulating the reference design, i.e. RM 0 in our PICs.

Doping profiles or doping levels are fundamental for the response of the ring because the carrier concentrations characterise both the optical losses and the strength of the modulation efficiency, as already studied from the previously reported measurements. Therefore, it is necessary to estimate the doping levels of the phase shifter to simulate the radiation effects on SiPh modulators.

3.1 Phase shifter design

The component that plays a critical role in the response of the RM is the phase shifter, i.e. the silicon PN junction built into the rib waveguide, which is used to modulate the resonance wavelength of the ring. The design of the RM is known in terms of geometrical features such as the rib width or slab thickness, but some relevant characteristics, such as doping profiles, are not known. The only known parameter concerning the electrical characteristics related to doping is the sheet resistance; therefore, this was used as a starting point to develop a procedure to obtain reasonable doping profiles that match with the measured current-voltage characteristics. The procedure will be described better in Section 3.1.1.

RM 0 has an all-pass configuration and a radius of 5 µm. The Sentaurus$^{\text{TM}}$ Process (*sprocess*) tool was used to simulate the manufacturing process of the ring. The first aim of the simulation was to reproduce the reasonable process flow to fabricate the device, with particular interest in the doping profile of the phase shifter, especially in the silicon rib. For this reason, rather than simulating the entire ring configuration, only a slice of the phase shifter was constructed. A 3D structure was developed, maintaining the same width and thickness of the real phase shifter, while the length of the slice was 600 nm. Figure 3.1 represents a schematic of the ring modulator; the cross-section of the simulated phase shifter is shown on the right side.

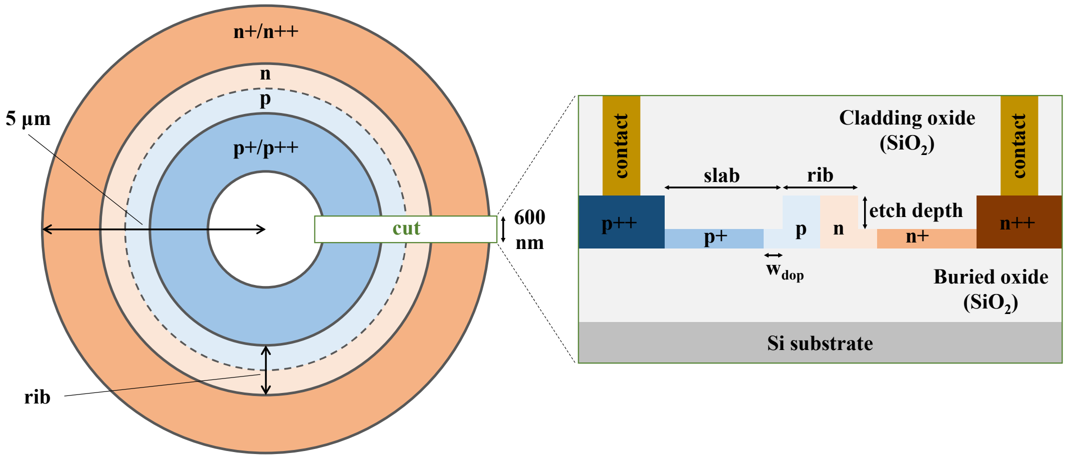

Figure 3.1: Schematic representation of the RM. On the right side is shown the cross-section of the simulated phase shifter on Sentaurus^{TM}.

The devices were manufactured on a 220 nm SOI platform, which corresponds to the declared rib height. The etch depth is 160 nm and this parameter directly influences the light confinement within the silicon rib. The higher the etch depth, the better the light confinement within the ring. However, the total depth also determines the surface over which the voltage applied at the contacts reaches the rib through the highly doped regions. Therefore, the greater the etch depth, the less uniform the potential will be at the sides of the rib. The rib width is 500 nm for RMs and 450 nm for MZMs, while the slab widths are 1000 nm for RMs and 1275 nm for MZMs [28]. The width of w_{dop} is 300 nm for RM 0, while it is smaller for the other rings designed by the team. The metal contacts on top of the heavily doped regions connect the phase shifter with the chip's BEOL. They consist of cylindrical tungsten vias surrounded by silicides.

The simulation starts with the construction of an SOI substrate (the silicon substrate was not simulated), i.e. standard SOI fabrication processes such as Smart Cut and wafer bonding were not emulated as they were beyond the scope of this work. Once the SOI is defined, with buried oxide (SiO_2) of 2000 nm and SOI of 220 nm thicknesses, the procedure is similar to a standard fabrication process. The SOI is patterned and etched by means of lithographic processes to obtain the phase shifter structure. The silicon is p-type, so is defined with an initial uniform boron concentration of $2.258 \cdot 10^{15}$ cm^{-3}. The initial boron concentration was found exploiting the procedure described in Section 3.1.1. The next step is to define the doping. The implantation process was simulated using the *sprocess* tool on the basis of the concentrations obtained from the sheet resistances. In particular, the model used is based on an analytical doping distribution that follows a Pearson distribution function. This model is well implemented in the software and is based on the implantation of dopant atoms following a Pearson distribution function, which can be defined as the solution to the following differential equation [47]:

$$\frac{\mathrm{d}}{\mathrm{d}y} f(y) = \frac{y-a}{b_0 + b_1 y + b_2 y^2} f(y) \quad \text{with} \quad y = x - R_\mathrm{p}, \tag{3.1}$$

where the a, b_0, b_1 and b_2 parameters are related to the higher order momenta of the function. The first moment is defined as:

$$R_\mathrm{p} = \int_{-\infty}^{+\infty} x f(x) \mathrm{d}x, \tag{3.2}$$

which is known as projected range. Higher order momenta m_i are defined as:

$$m_i = \int_{-\infty}^{+\infty} (x - R_\mathrm{p})^i f(x) \mathrm{d}x. \tag{3.3}$$

Apart from R_p, the other three momenta used to define the Pearson distribution function are:

$$\begin{aligned} \sigma &= \sqrt{m_2} \\ \gamma &= \frac{m_3}{\sigma^3} \\ \beta &= \frac{m_4}{\sigma^4} \end{aligned} \tag{3.4}$$

Relating these parameters to the well-known Gaussian distribution, σ is the standard deviation, while γ and β are the skewness and the kurtosis respectively. The skewness is the moment of the function which indicates the asymmetry of the distribution with respect to its centre, while the kurtosis indicates the importance of the tails of the distribution. If $\gamma = 0$ and $\beta = 3$ the distribution becomes Gaussian. The software allows you to define the Pearson distribution function for the implanted dopants by inserting these parameters. The four momenta characterising the distribution (i.e. R_p, σ, γ and β) have been obtained thanks to Lumerical simulations aimed at finding the best doping profile matching the optical simulations with the experimental results. This analytical implantation procedure was adopted only for the regions with thickness 220 nm (i.e. p++, p, n and n++), while for p+ and n+ regions the default Dios tables provided by the software were used [53].

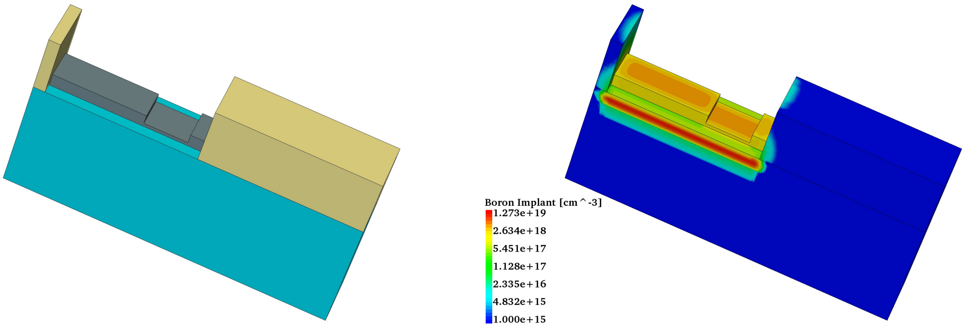

(a) *Photoresist: deposition and patterning.* (b) *Boron implantation.*

Figure 3.2: (a) Example of photoresist deposition and patterning before ion implantation. (b) Boron implantation of the phase shifter; the dose used is for the p-region of the rib, but to simulate a realistic fabrication process the implantation of the low-doping region is done also for the other regions (p+/p++). Notice that the annealing step is not yet done because will be performed only at the end of all the implantation steps.

In total, the phase shifter is composed of six different doped regions, therefore, the implantation simulation procedure tries to follow realistic ion implantation steps. For all the implantations, the model to evaluate damage in the silicon resulting from the implantation is activated, while the channelling was suppressed because the tilt and rotation angles of the ion beam were kept to zero, as it was not necessary to have these angles at realistic values for a quasi-2D simulation. The lithographic masks were defined in order to cover the different regions not to be implanted, i.e. the masks for the photoresist patterning were positive. An example of photoresist patterning followed by boron implantation is shown in Figure 3.2. As can be seen, the implantations are not done separately for each of the six different regions to be doped. This would not have been realistic in a fabrication process, so when p or n regions were implanted, p+/p++ and n+/n++ were also implanted. This implies that the implant doses found in Section 3.1.1 have to be tuned for each new implantation step, taking into account the dose already implanted. The tuning was done by taking a 1D cut in the middle of the region of interest and calculating the integral of the dopant distribution. By iterating this process throughout the implantation steps, it was possible to find the final doses to be set. The energies of the ion beam for each implantation were determined using an online calculator [21] (based on [13]), looking at the energy that gave the maximum of the implantation distribution at the centre of the silicon thickness. A final summary of the parameters used to define all the ion implantations of dopants is given in Table 3.1. The rapid thermal annealing for dopants activation was simulated at a temperature of 1050 ℃ for a time of 5 seconds. The final doping distribution is shown in Figure 3.3.

The last part of the simulation of the fabrication process is the realisation of the cladding oxide and the metal contacts. The cladding oxide (SiO_2) was deposited and then etched

	Dose, [cm^{-2}]	Energy, [keV]	Ion species
p	$1.5 \cdot 10^{14}$	35	Boron
p+	$3.8 \cdot 10^{14}$	7.5	Boron
p++	$1.42 \cdot 10^{15}$	35	Boron
n	$1.5 \cdot 10^{14}$	90	Phosphorous
n+	$3.1 \cdot 10^{14}$	25	Phosphorous
n++	$2.4 \cdot 10^{15}$	90	Phosphorus

Table 3.1: Implantation parameters used to define the doping of the phase shifter simulated with Sentaurus$^{\text{TM}}$ Process software.

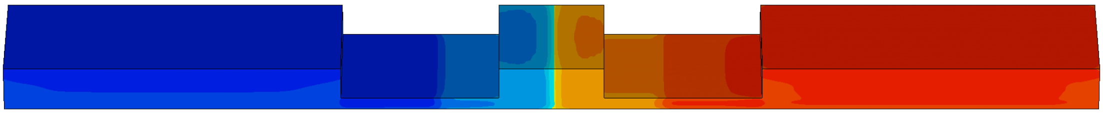

Figure 3.3: Final doping concentration of the phase shifter.

and planarised by means of a chemical-mechanical polishing (CMP) step, to reach a final thickness of 500 nm. Two masks were defined to etch the oxide over the heavily doped regions (p++/ n++) to realise the tungsten metal vias and silicides. After SiO_2 etching, the silicides were deposited and patterned to obtain four cylindrical vias, one for each tungsten pillar. At this point, the tungsten was deposited, and a final CMP was performed to planarize the final structure. Finally, copper was deposited on top of the tungsten-silicide region to obtain the final metal contacts for the electrical stimulation. The resulting structure of the phase shifter is shown in Figure 3.4.

3.1.1 Analytical model: doping concentration starting from sheet resistance

The biggest unknowns needed to simulate the phase shifter of the ring modulator were the doping profiles. Neither the characteristics of the ion implantation processes nor the nominal values of the doping in the six different regions were known. The only known parameter that was directly related to the doping concentration of the phase shifter was the sheet resistance. In the following, a method has been developed to calculate the possible dopant dose implanted in the silicon starting from this parameter. The procedure used is based a renowned model for electron and holes mobilities as a function of concentration

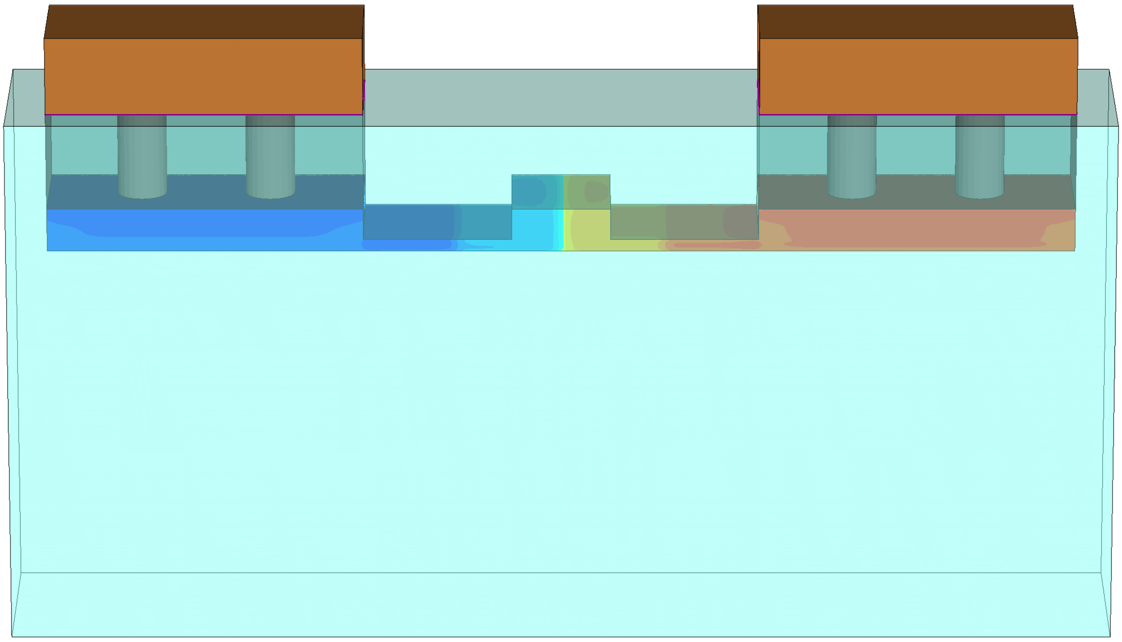

Figure 3.4: Final 3D structure of the phase shifter of RM 0 simulated with Sentaurus$^{\mathrm{TM}}$ TCAD.

and temperature, known as Arora mobility model [11], which is well implemented in the Sentaurus$^{\mathrm{TM}}$ Device (*sdevice*) tool that will be used for the electrical simulation. As already mentioned in Section 3.1, it is reasonable that multiple implantation processes are used for the highly-doped regions, while this method can give the possible values of the dose to be used for a single ion implantation. It will be explained later how the doses for p+/p++ and n+/n++ regions were determined.

The sheet resistance is the resistance of a piece of semiconductor, the thickness of which is much smaller than the two other dimensions. It is a parameter used to compare the electrical properties of devices that can be significantly different in size. The sheet resistance can be defined starting from the 3D resistance as:

$$R = \rho \cdot \frac{L}{A} = \rho \frac{L}{Wt} = R_{\mathrm{s}} \frac{L}{W}, \tag{3.5}$$

where R_{s} is the sheet resistance and ρ is the resistivity.

In general, if the sample is uniformly doped the resistivity is constant and the sheet resistance is:

$$R_{\mathrm{s}} = \frac{\rho}{t}. \tag{3.6}$$

For non-uniformly doped samples, the sheet resistance along the thickness t can be written as [42]:

$$R_{\mathrm{s}} = \left[\int_0^t \left(\frac{1}{\rho(x)}\right) \mathrm{d}x\right]^{-1} = \left[\int_0^t \sigma(x) \mathrm{d}x\right]^{-1} = \left[q \int_0^t \left[n(x)\mu_{\mathrm{e}}(x) + p(x)\mu_{\mathrm{h}}(x)\right] \mathrm{d}x\right]^{-1}, \tag{3.7}$$

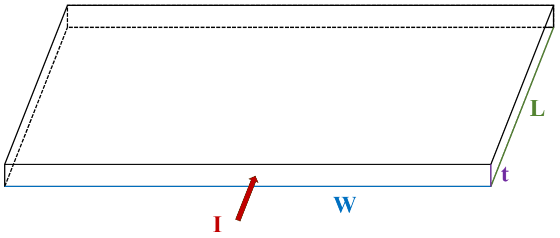

Figure 3.5: Geometrical representation of the sheet resistance definition; the current I is considered parallel to L.

where $\sigma(x)$ is the electrical conductivity, $n(x)$ and $p(x)$ are the electron and hole concentrations and $\mu_{\mathrm{e}}(x)$ and $\mu_{\mathrm{h}}(x)$ are the corresponding mobilities. In this study, the temperature dependence of conductivity is not considered and all parameters are related to an ambient temperature of 300 K. We can start by analysing the p-doped region of the rib. In this case, we can consider $p_{\mathrm{p}} >> n_{\mathrm{p}}$, thus the sheet resistance can be approximated as:

$$R_{\mathrm{s}} \approx \left[q \int_0^{x_{\mathrm{j}}} p(x) \mu_{\mathrm{h}}(x) \mathrm{d}x \right]^{-1} . \tag{3.8}$$

The junction depth x_{j} is defined as the depth at which the implanted dopant concentration reaches the bulk concentration of the sample. The hole concentration $p(x)$ in the p-doped sample, by assuming a complete ionisiation of dopants, can be written as:

$$p(x) = N_{\mathrm{A}}(x) + N_{\mathrm{B_p}}, \tag{3.9}$$

where $N_{\mathrm{B_p}}$ is the bulk hole concentration and $N_{\mathrm{A}}(x)$ is the acceptor concentration. The first concentration that must be found is the bulk one; the SOI is p-type and the resistivity of the unprocessed silicon layer is given, hence:

$$\rho = \frac{1}{\sigma} = \frac{1}{q N_{\mathrm{B_p}} \mu_{\mathrm{h}}} \rightarrow N_{\mathrm{B_p}} = \frac{1}{q \rho \mu_{\mathrm{h}}}, \tag{3.10}$$

where $N_{\mathrm{B_p}}$ is assumed to be uniform in all the SOI, as for the resistivity. The hole mobility $\mu_{\mathrm{h}}(x)$, according to the Arora model [11], can be analytically expressed as:

$$\mu_{\mathrm{h}}(x) = 54.3\,(T_{\mathrm{n}})^{-0.57} + \frac{1.36 \cdot 10^8\, T^{-2.23}}{1 + \left(\frac{N_{\mathrm{A}}(x)}{2.35 \cdot 10^{17}\, T_{\mathrm{n}}{}^{2.4}} \right) 0.88\, T_{\mathrm{n}}{}^{-0.146}} , \tag{3.11}$$

and similarly for electrons:

$$\mu_{\mathrm{e}}(x) = 88\,(T_{\mathrm{n}})^{-0.57} + \frac{7.4 \cdot 10^8\, T^{-2.33}}{1 + \left(\frac{N_{\mathrm{D}}(x)}{1.26 \cdot 10^{17}\, T_{\mathrm{n}}{}^{2.4}} \right) 0.88\, T_{\mathrm{n}}{}^{-0.146}} . \tag{3.12}$$

The model expresses the dependence of the mobility on both temperature T and doping concentrations N_A or N_D. $T_\mathrm{n} = T/300\,\mathrm{K}$, therefore in this study will be simply equal to unity. It can be shown that for low doping concentrations and for $T = 300\,\mathrm{K}$ the mobility is almost constant for both electrons and holes, as reported in Figure 3.6.

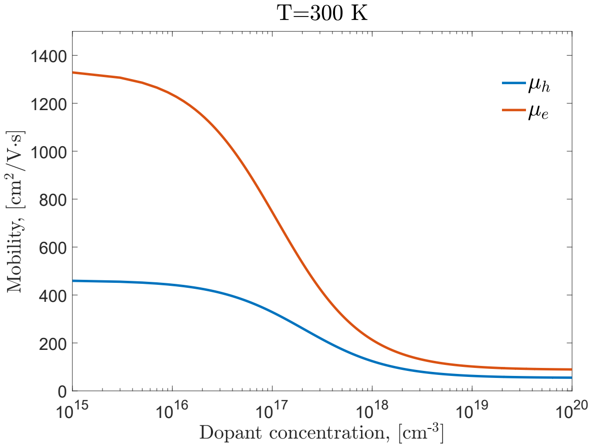

Figure 3.6: Electron and hole mobility according to the Arora model [11] for $T = 300\,\mathrm{K}$ as a function of the dopant concentration, boron and phosphorous respectively.

Therefore, to find the bulk concentration N_Bp from (3.10), the hole mobility μ_h can be considered constant and the bulk concentration of holes in the p-type SOI with is:

$$N_\mathrm{Bp} = \frac{1}{q\rho\mu_\mathrm{h}} = 1.4 \cdot 10^{15}\ \mathrm{cm}^{-3}, \tag{3.13}$$

with $\mu_\mathrm{h} = 459.3\ \mathrm{cm}^2/\mathrm{V}\cdot\mathrm{s}$ for a dopant concentration of $10^{15}\ \mathrm{cm}^{-3}$. By knowing the bulk hole concentration and considering the thermodynamic equilibrium, the mass-action law can be applied to determine the electron bulk concentration in the p-type SOI:

$$np = {n_\mathrm{i}}^2 \ \rightarrow \ N_\mathrm{Bn} = \frac{{n_\mathrm{i}}^2}{N_\mathrm{Bp}} = 6.7 \cdot 10^4\ \mathrm{cm}^{-3} \tag{3.14}$$

with $n_\mathrm{i} = 9.65 \cdot 10^9\ \mathrm{cm}^{-3}$ intrinsic carrier concentration of silicon at $T = 300\,\mathrm{K}$ [10]. As already mentioned in Section 3.1, the profiles of the doping implantation were found by means of Lumerical simulations. In order to find the dose to be implanted, that can be set in the simulator, we can assume a constant $N_\mathrm{A}(x)$ profile. Under this assumption, the hole mobility μ_h is constant along the silicon thickness and starting from (3.11) can be rewritten as:

$$\mu_\mathrm{h} = a + \frac{b}{1 + cN_\mathrm{A}} \tag{3.15}$$

with:

$$\begin{aligned} a &= 54.3\, T_{\mathrm{n}}^{-0.57} \\ b &= 1.36 \cdot 10^{8}\, T^{-2.23} \\ c &= \frac{0.88\, T_{\mathrm{n}}{}^{-0.146}}{2.35 \cdot 10^{17}\, T_{\mathrm{n}}^{2.4}}\ . \end{aligned} \tag{3.16}$$

Since the acceptor profile was assumed to be constant, the upper integration limit x_{j} in 3.8 becomes simply the 220 nm thickness of the SOI, because there is not a point in the vertical direction in which the acceptor concentration can equal the bulk one. By substituting (3.15) in (3.8), we get a quadratic equation for N_{A}:

$$N_A^2[(qR_{\mathrm{s}}t)(ac)] + N_{\mathrm{A}}[(qR_{\mathrm{s}}t)(a+b+acN_{\mathrm{Bp}})-c] + [(qR_{\mathrm{s}}t)(aN_{\mathrm{Bp}}+bN_{\mathrm{Bp}})-1] = 0, \tag{3.17}$$

that can be solved for the three p-regions according to the specific thickness t and the sheet resistance R_{s}. Once the acceptor concentrations have been found, it can be calculated the dose for the ion implantation to be set in *sprocess*. The dose is:

$$Q = \int_{-\infty}^{+\infty} N_{\mathrm{implanted}}(x)\mathrm{d}x, \tag{3.18}$$

which can be written by considering the dopants implanted in the SOI as:

$$Q = \int_{0}^{t} (N_{\mathrm{A}}(x) - N_{\mathrm{Bp}})\mathrm{d}x. \tag{3.19}$$

It turns out that, under the assumption of a uniform doping concentration along the thickness and by exploiting the Arora model for the carrier mobility, the acceptor concentrations N_{A} and the corresponding implant doses Q for the three p-doped region are:

	Acceptor concentration, [cm^{-3}]	Implant dose, [cm^{-2}]
p	$3.27 \cdot 10^{18}$	$7.20 \cdot 10^{13}$
p+	$1.51 \cdot 10^{19}$	$3.31 \cdot 10^{14}$
p++	$5.42 \cdot 10^{19}$	$1.20 \cdot 10^{15}$

Table 3.2: Calculated acceptor concentrations and implant doses for the three p-doped regions of the SOI.

It is clear that from 3.19, the dose implanted in the buried oxide or other effects are not considered. Moreover, as already reported, these values have been found for stand-alone ion implantation processes and not for multiple ones. The final doses used in the simulator are not the ones reported in Table 3.2, but they have been found starting from those values and by taking the integral of the acceptor concentration for each implantation step, accordingly tuning the implant doses to match with the ones in 3.2. By following this procedure and using the coefficients of the Pearson distribution function found with Lumerical, multiple implantation steps have been simulated. A final schematic representation of the implantation processes is shown in Figure 3.7.

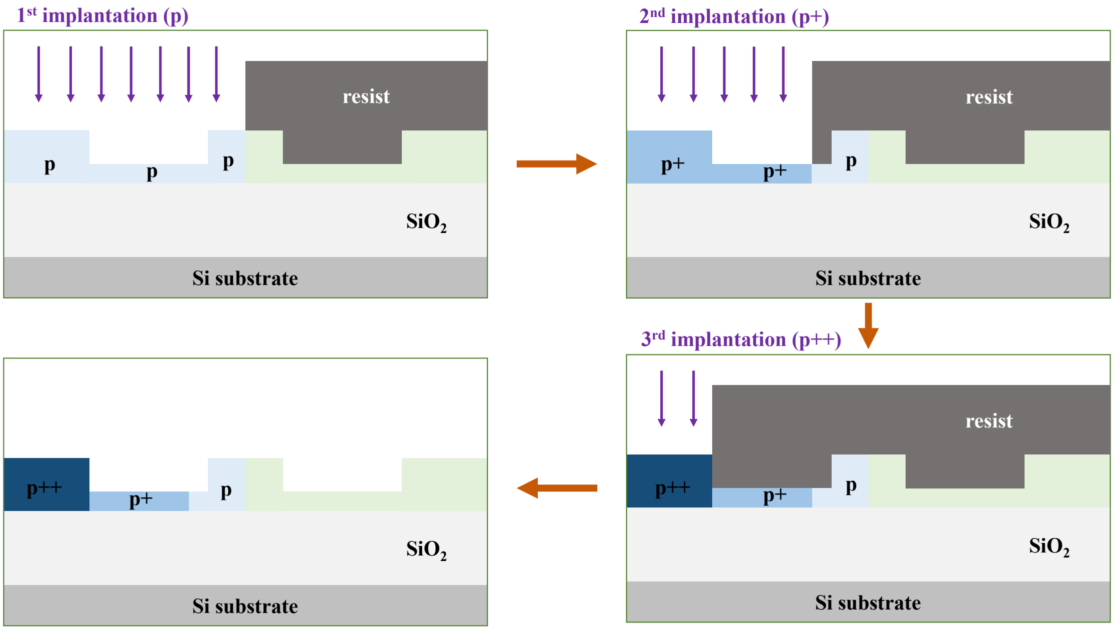

Figure 3.7: Schematic representation of the simulated implantation steps for the three p-doped regions of the phase shifter. After each step, a cut was performed in the vertical direction, and the integral of the acceptor concentration was calculated. Following this procedure, the final implant doses to be set in *sprocess* have been found to match Table 3.2.

The same procedure shown for the p-doped regions of the phase shifter has been followed for the n-type doping. In this case we can consider $n_\mathrm{n} >> p_\mathrm{n}$, therefore (3.7) can be written as:

$$R_\mathrm{s} \approx \left[q \int_0^{x_\mathrm{j}} n(x) \mu_\mathrm{e}(x) \mathrm{d}x \right]^{-1} \tag{3.20}$$

with:

$$n(x) = N_\mathrm{D}(x) + N_\mathrm{Bn}. \tag{3.21}$$

By assuming again uniform doping concentration along the thickness and by combining the electron mobility defined in (3.12) with (3.20), we obtain the quadratic equation for N_D:

$$N_\mathrm{D}{}^2[(qR_\mathrm{s}t)(ac)] + N_\mathrm{D}[(qR_\mathrm{s}t)(a+b+acN_\mathrm{Bn}) - c] + [(qR_\mathrm{s}t)(aN_\mathrm{Bn} + bN_\mathrm{Bn}) - 1] = 0, \tag{3.22}$$

with:

$$\begin{aligned} a &= 88\,T_{\mathrm{n}}^{-0.57} \\ b &= 7.4 \cdot 10^{8}\,T^{-2.33} \\ c &= \frac{0.88\,T_{\mathrm{n}}^{-0.146}}{1.26 \cdot 10^{17}\,T_{\mathrm{n}}^{2.4}}\ . \end{aligned} \tag{3.23}$$

The donor concentrations N_{D} and the corresponding implant doses Q for the n-doped region of the phase shifter are:

	Donor concentration, [cm^{-3}]	Implant dose, [cm^{-2}]
n	$3.06 \cdot 10^{18}$	$6.73 \cdot 10^{13}$
n+	$1.30 \cdot 10^{19}$	$2.85 \cdot 10^{14}$
n++	$6.88 \cdot 10^{19}$	$1.52 \cdot 10^{15}$

Table 3.3: Calculated donor concentrations and implant doses for the three n-doped regions of the SOI.

The doses in Tables 3.2 and 3.3 can be compared with the final doses used for the implantation reported in Table 3.1. As mentioned above, the final doses are higher because effects such as buried oxide implantation are not taken into account in the analytical model, which was used as a starting reference point.

3.2 Electrical simulation

Once the structure was created, the phase shifter was electrically simulated with the Sentaurus $^{\mathrm{TM}}$ Device tool. The simulation relies in solving the Poisson equation for electrons and holes with a Finite Element Method (FEM), i.e. a meshing of the structure is required. The mesh is critical to achieve a reasonable simulation without drastically increasing the computational time. An user-defined mesh was created, where finer steps were used in critical regions such as the silicon rib or the silicon-oxide interfaces, as shown in Figure 3.8.

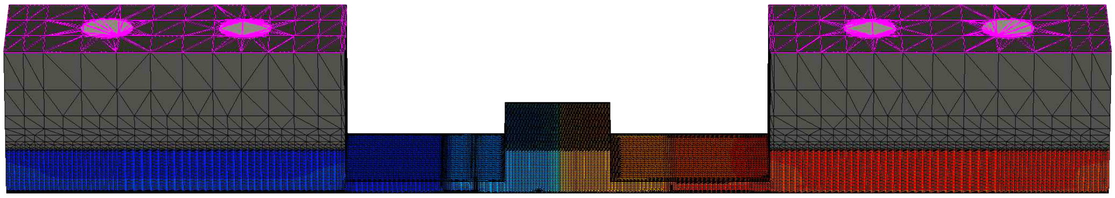

Figure 3.8: Mesh created for the electrical simulation of the phase shifter.

The *sdevice* tool allows the user to select the physical models to be implemented in the simulation, where a very well-stocked library is available. Fermi statistics and incomplete ionisation were activated for all the simulations, as for the Arora mobility model and the Auger and Shockley–Read–Hall (SRH) recombination mechanisms. The temperature of all simulations is set at 300 K. First, the phase shifter will be simulated in the pre-irradiation conditions, i.e. the current-voltage characteristic will be calculated and compared with the experimental results. Subsequently, the damage induced by neutron irradiation is implemented by means of ad hoc models that include different trap states in the silicon band gap.

3.2.1 Pre-irradiation

Simulation of the phase shifter prior to irradiation is essential to verify that the doping profiles generated result in a good match between the simulated and measured electrical characteristics. The first simulation is performed under equilibrium conditions, i.e. the phase shifter is not biased. Some relevant physical quantities calculated by the software, such as electric field, electrostatic potential and space charge, are reported in Figure 3.9.

To compare the measurements with the simulation, the phase shifter was biased and the current-voltage characteristic was calculated. Following the same biasing condition of the neutron irradiation test, the phase shifter was simulated in both forward and revers bias. A quasi-stationary simulation was performed, solving the Poisson equation for electrons and holes at each bias point, taking into account the physical models activated in the *sdevice* tool aforementioned. The comparison could not be made with the total current because only a section of the phase shifter of the RM was simulated, therefore, the current densities were evaluated. The surfaces considered are the PN junction area within the rib for both the real RMs and the simulated phase shifter, which are respectively given by:

$$\begin{aligned} A_{\text{TCAD}} &= 0.22\ \mu\text{m} \times 0.6\ \mu\text{m} \\ A_{\text{PIC}} &= 0.22\ \mu\text{m} \times (2\pi \times 5\ \mu\text{m})\ . \end{aligned} \tag{3.24}$$

The result in forward voltage of the TCAD simulation is shown in Figure 3.10a, where it is compared with the pre-irradiation measurements of the PICs. For all subsequent comparisons, the current-voltage characteristics will be presented in both logarithmic and linear scales, with the absolute value of current densities shown in the upper and lower graphs, respectively. For low voltages, the measurements show a much higher current compared to the simulated one. This was expected because the experimental setup of the irradiation test did not allow precise measurements of low currents. The TCAD simulation shows a very good agreement with the measurements in the forward current region.

The same analysis was performed for the reverse voltage; the outcome is shown in Figure 3.10b. The simulation of the junction breakdown with the software is very critical as various mechanisms, including avalanche generation and band-to-band tunneling, play a crucial role.

The low-current regions simulated cannot be compared with the pre-irradiation measurement results due to setup limitations. To further confirm the accuracy of the TCAD model, precise current measurements were carried out in the laboratory after the irradiation test, using a picoampere meter with decleared current resolution of 1 pA. Four separate PICs were assembled to wire bond only RM 0 of each chip to the PCB, and both forward and reverse current-voltage characteristics were collected. To collect statistical information on process variability among silicon wafers, it was decided to select four PICs from distinct

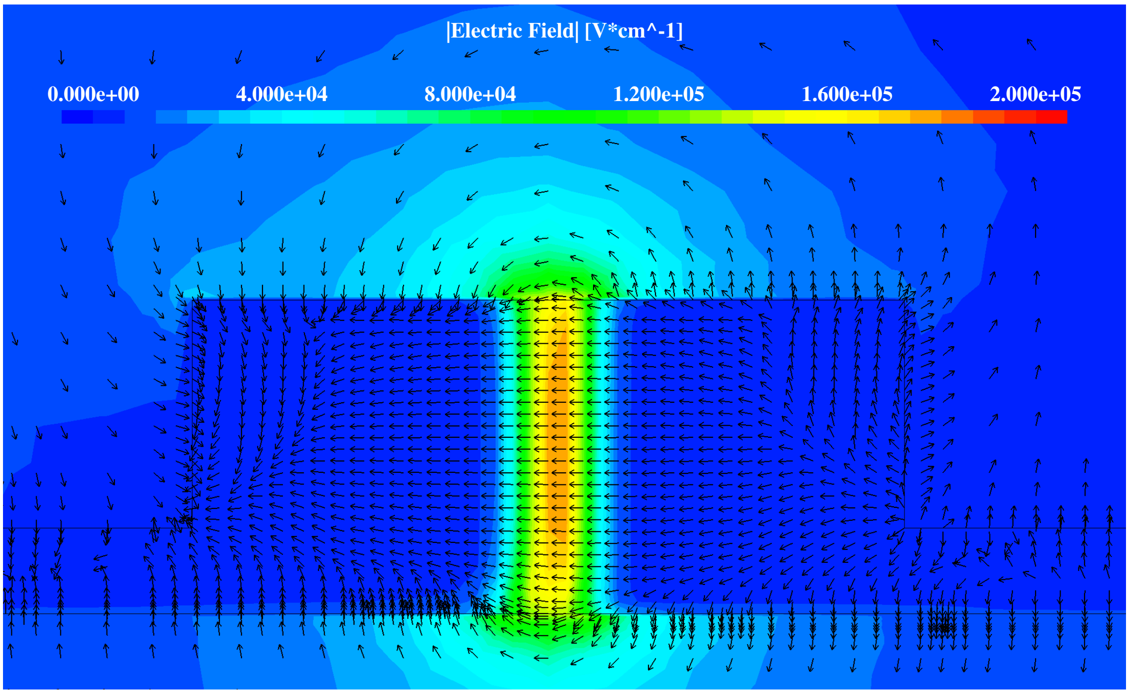

(a) *Electric field (absolute value).*

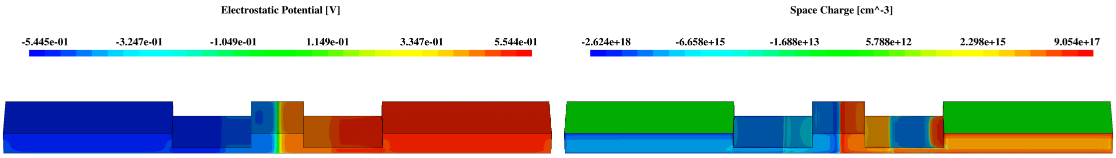

(b) *Electrostatic potential.*

(c) *Space charge.*

Figure 3.9: Physical quantities of the phase shifter calculated with *sdevice* under equilibrium condition: (a) electric field (absolute value with vectorial directions), (b) electrostatic potential, (c) space charge.

wafers. The objective of this test was also to evaluate the RM response at higher currents, even if this led to inevitable damage to the device, especially above breakdown. For both reverse and forward bias, currents exceeding mA were reached, which is more than three orders of magnitude larger than the current limit set during the irradiation test. The current saturation, resulting from the voltage drop in the low-resistivity area of the junction is easily observable. The results with the PICs measured in the laboratory are compared with the TCAD simulation before irradiation and are shown in Figure 3.11.

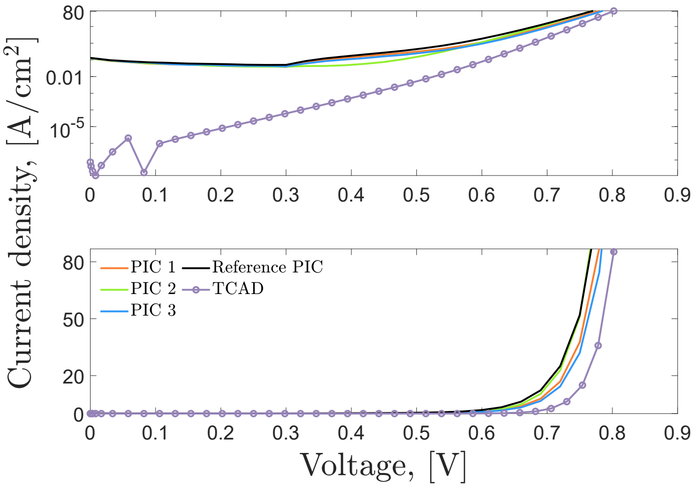

(a) *Forward bias.*

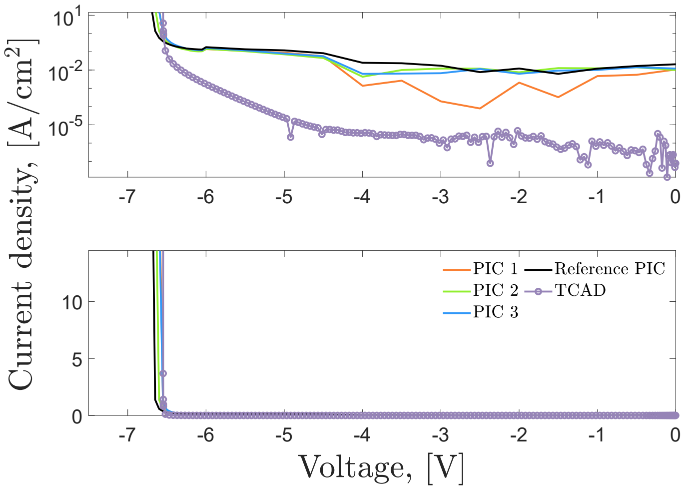

(b) *Reverse bias.*

Figure 3.10: Current-voltage characteristics for RM 0 before neutron irradiation, compared with the TCAD simulation.

The good agreement between the electrical simulation of the phase shifter and the actual measurements provides solid validation for the methodology proposed in Section 3.1.1 to determine the doping profiles.

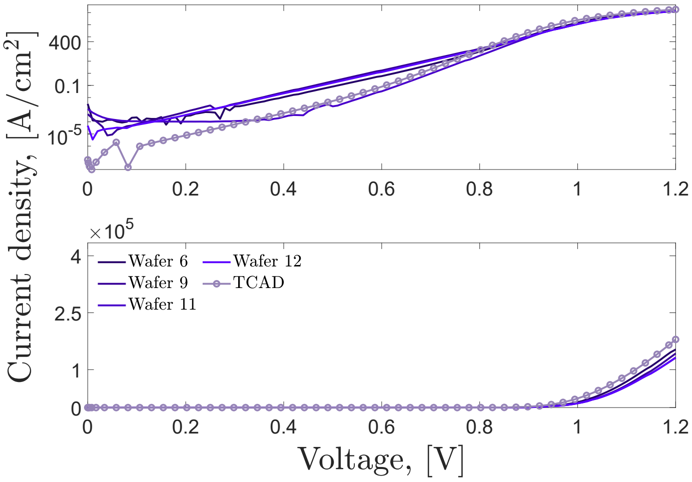

(a) *Forward bias.*

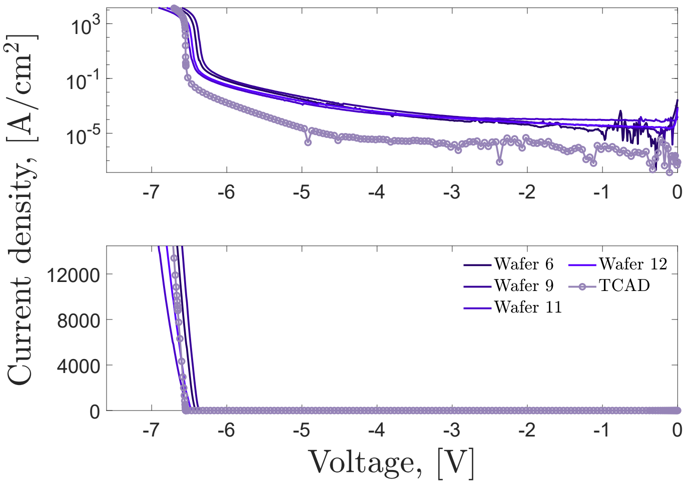

(b) *Reverse bias.*

Figure 3.11: Current-voltage characteristics for RM 0 from four different PICs of four different silicon wafers, acquired with the picoampere meter, compared with the TCAD simulation.

3.2.2 Neutron damage simulation

The modelling of neutron-induced damage to Silicon Photonics ring modulators remains an under-researched area in the literature. As highly penetrating particles that are indirectly ionising due to their charge neutrality, the ionisation produced by neutron irradiation can be attributed to either neutron absorption by nuclei or secondary ionisation resulting from displaced atoms. It is widely recognised that the displacement of atoms induced by neutrons is responsible for critical damage in silicon detectors for particle accelerators [30], [40]. This ultimately triggers a process referred to as donor/acceptor removal, whereby the initial doping concentration is effectively reduced. Collisions by fast neutrons and displaced recoiling atoms can displace and deactivate dopant atoms, leading to a reduction in the effective doping concentration and to the generation of different types of defects. This, in turn, increases both leakage currents and the full-depletion voltage of silicon detectors [29].

The TCAD simulation developed for the phase shifter under study implements ad hoc models that have been realised to describe bulk and surface damage caused by high-fluence protons and X-ray radiations. At present, there are no specific models available to accurately simulate the damage induced by high-fluence neutron irradiation at the device level for Silicon Photonics modulators. The adopted model relies on the implementation of trap states within the silicon band gap to replicate the radiation effect at the device level. The "Hamburg Pentatrap Model" (HPM) [43] and the "Perugia Surface and Bulk" (PSB) radiation damage model [12] have been developed through numerous irradiation tests on various silicon components. They introduce different trap states in the silicon band gap, and the characteristics were specifically defined according to the irradiation results. Both models define single-energy level trap states, in which concentration can be calculated as a function of the fluence by means of a specific factor (g_{int} for HPM and η for PSB).

The models can be fully implemented using the *sdevice* tool by defining the trap states for both donors and acceptors. The acceptor and donor traps remain uncharged when not occupied, and they carry the charge of one electron for acceptors and one hole for donors when they are fully occupied. Neither of the models is concerned with incorporating the precise defect species into the TCAD simulation, as this would be not feasible in the tool environment due to numerical convergence related problems. The goal of the models is to introduce certain trap state levels to emulate the macroscopic effects observed in the irradiated devices, i.e. the variation in the electrical characteristics due to neutron radiation damage. It is worth noting that defining the actual defect species, concentration, and distribution at high levels of neutron fluence remains challenging. Therefore, understanding these features at the microscopic level is difficult. Tables 3.4, 3.5 and 3.6 show the parameter for the two respective models.

Defect	Type	Energy, [eV]	g_{int}, [cm^{-1}]	σ_{e}, [cm^2]	σ_{h}, [cm^2]
E30K	Donor	$E_C - 0.1$	0.0497	$2.300 \cdot 10^{-14}$	$2.920 \cdot 10^{-16}$
V_3	Acceptor	$E_C - 0.458$	0.6447	$2.551 \cdot 10^{-14}$	$1.511 \cdot 10^{-13}$
I_p	Acceptor	$E_C - 0.545$	0.4335	$4.478 \cdot 10^{-15}$	$6.709 \cdot 10^{-15}$
H220	Donor	$E_V + 0.48$	0.5978	$4.166 \cdot 10^{-15}$	$1.965 \cdot 10^{-16}$
C_iO_i	Donor	$E_V + 0.36$	0.3780	$3.230 \cdot 10^{-17}$	$2.036 \cdot 10^{-14}$

Table 3.4: Parameters from the Hamburg Pentatrap Model, for a proton fluence in the range from $3{\cdot}10^{14}$ n_{eq}/cm^2 to $1.3{\cdot}10^{16}$ n_{eq}/cm^2 [43].

Type	Energy, [eV]	η, [cm^{-1}]	σ_e, [cm^2]	σ_h, [cm^2]
Donor	$E_C - 0.23$	0.015	$2.3 \cdot 10^{-14}$	$2.3 \cdot 10^{-15}$
Acceptor	$E_C - 0.42$	10	$1.0 \cdot 10^{-15}$	$1.0 \cdot 10^{-14}$
Acceptor	$E_C - 0.46$	1.2	$4.0 \cdot 10^{-14}$	$4.0 \cdot 10^{-13}$

Table 3.5: Parameters from the Perugia Bulk Model, for an equivalent fluence up to $1{\cdot}10^{16}$ n$_{eq}$/cm^2 [12].

Type	Energy, [eV]	Concentration, [cm^{-2}]	σ_e, [cm^2]	σ_h, [cm^2]
Fixed Charge	-	$1.08 \cdot 10^{12}$	-	-
Acceptor	$E_C - 0.56 \le E_T \le E_C$	$1.35 \cdot 10^{12}$	$1.0 \cdot 10^{-16}$	$1.0 \cdot 10^{-15}$
Donor	$E_V \le E_T \le E_V + 0.60$	$1.20 \cdot 10^{12}$	$1.0 \cdot 10^{-15}$	$1.0 \cdot 10^{-16}$

Table 3.6: Parameters from the Perugia Surface Model at saturation, i.e. for doses higher than 10 Mrad [31]. E_T is the energy level of the trap state.

A schematic representation of the trap states that both models introduce in the silicon band gap is shown in Figure 3.12.

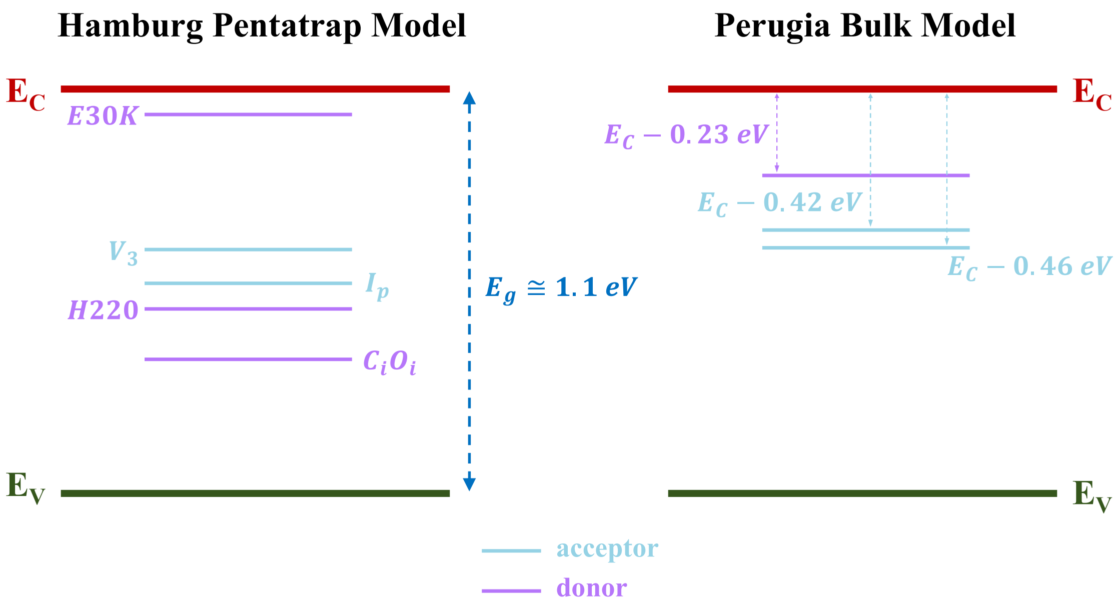

Figure 3.12: Representation of the trap states within the silicon band gap introduced by the Hamburg Pentatrap Model and the Perugia Bulk Model.

The models were implemented in TCAD simulation and were tested for the phase shifter under study in both forward and reverse biases. Both models are able to predict the results observed during the irradiation test, such as the increase in the breakdown voltage and the reduction of the diode threshold in forward bias. However, the reverse saturation current parameter could not be compared due to experimental setup limitations. The effective doping reduction mechanism is expected to increase this value with irradiation because it is directly related to the minority carrier concentrations within the junction. With a reduction of the effective doping concentration, there will be a corresponding increase in the minority carrier concentrations in the p- and n-doped regions, respectively, i.e. the reverse saturation current increases. The simulation can predict this phenomenon; hence, future irradiation tests can be improved to measure the reverse saturation current accurately. The current-voltage characteristics of RM 0 were compared with the TCAD model starting from the highest fluence reached, that is $\phi = 3.8 \cdot 10^{16}$ n/cm^{-2}, which was reached only by PIC 1. The simulation result is shown in Figure 3.13.

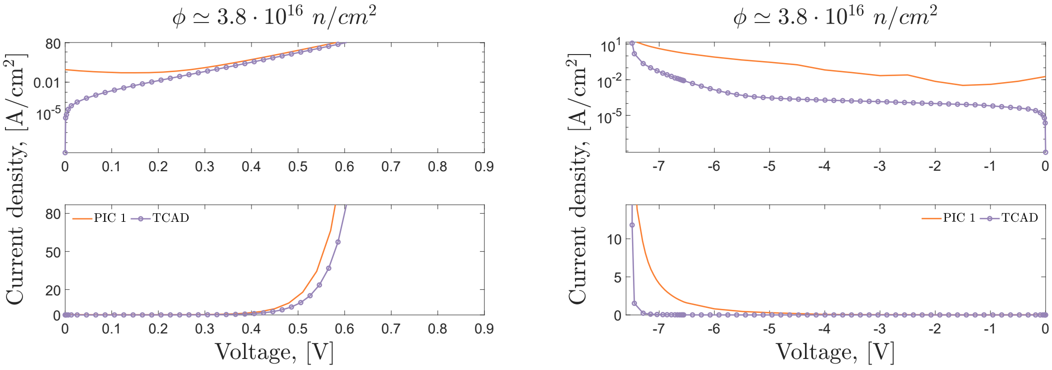
$\phi \simeq 3.8 \cdot 10^{16}\ n/cm^2$

$\phi \simeq 3.8 \cdot 10^{16}\ n/cm^2$

(a) *Forward bias.*

(b) *Reverse bias.*

Figure 3.13: Current-voltage characteristics for RM 0 of PIC 1 at the highest reached neutron fluence of 3.8·10^{16} n/cm^2, compared with the TCAD simulation.

The simulation results are capable of representing quite accurately the effects induced by neutron irradiation. Both forward and reverse biases follow the same trend observed with the measured samples, and the reverse saturation current of the TCAD simulation increases as expected. The reverse and forward biases both align with the trend observed in the measured samples. The TCAD simulation's reverse saturation current increases as expected. The smoothing of the breakdown kink, already observed in the irradiation measurements, is not well reproduced by the simulation: the reason for this may be hidden in the challenge of accurately simulating junction breakdown. Since the variation in the breakdown kink is typically linked to the dominant breakdown mechanism, it is a cumbersome task to properly simulate whether avalanche generation or band-to-band tunnelling occurred first. It must be noted that the HPM model was used for reverse bias, while the PSB model was used for forward voltage. The Perugia model overestimated the breakdown voltage in the reverse bias, while the Hamburg Pentatrap model underestimated the current for the forward bias. These models have not been developed for neutron irradiation or SiPh modulators, so perfect matching between simulations and measurements is not to be expected. Furthermore, simulating the entire phase shifter structure shown in Figure 3.4 under reverse bias was not feasible due to the complexity of the structure and numerical convergence issues due to the implementation of trap states. Consequently, the simulated device was simplified by excluding the highly doped regions and contacts, while retaining only the p- and n-doped areas. The simplified structure for the reverse bias simulations of neutron irradiation is shown in Figure 3.14.

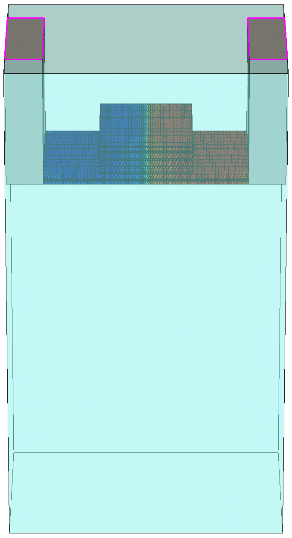

Figure 3.14: Simplified structure of the phase shifter used for simulating the neutron irradiation effects under reverse bias. The rib mesh remains unaltered.

It is noteworthy to compare the electric field at the PN junction in the high-fluence simulation with the pre-irradiation one. The electric field helps in understanding the previously discussed results; the breakdown of the junction can occur primarily as a result of two mechanisms: the avalanche generation or band-to-band tunnelling. This was already discussed in Section 2.4.1, but an insight to the calculated electric field highlights how the absolute electric field at the junction is reduced with the irradiation models. Figure 3.15 shows the electric fields under equilibrium calculated in the pre-irradiation condition and with the PSB model. Compared to the electric field of the non-irradiated phase shifter depicted in Figure 3.15a, a reduction is apparent for the electric field at the junction in Figure 3.15b. This agrees with the observed tendency for the breakdown voltage to increase with neutron irradiation, meaning that a greater applied voltage is required to initiate the junction breakdown. Unfortunately, these models do not alter the doping concentrations of the phase shifter directly. As a result, it is not possible to compare the doping profiles, and it is impossible to analyse the acceptor/donor removal mechanisms using the current models.

Further simulations were performed, varying the concentrations of trap levels according to the models and corresponding fluences. The general trend followed confirms the reasonable accuracy of the simulation results compared to the measured results. Simulations have shown higher levels of correspondence in the medium-high fluence range, approximately

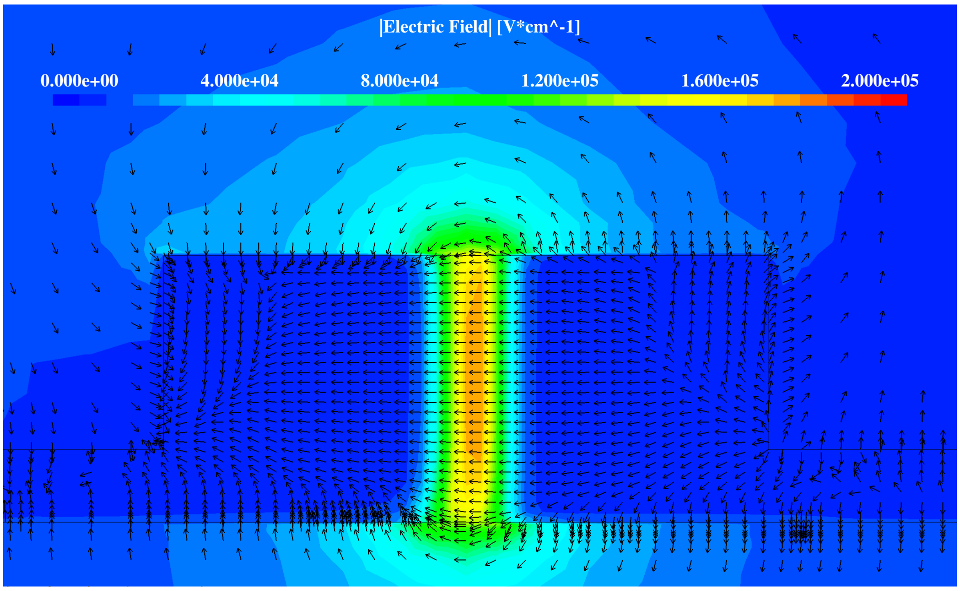

(a) *Electric field (pre-irradiation).*

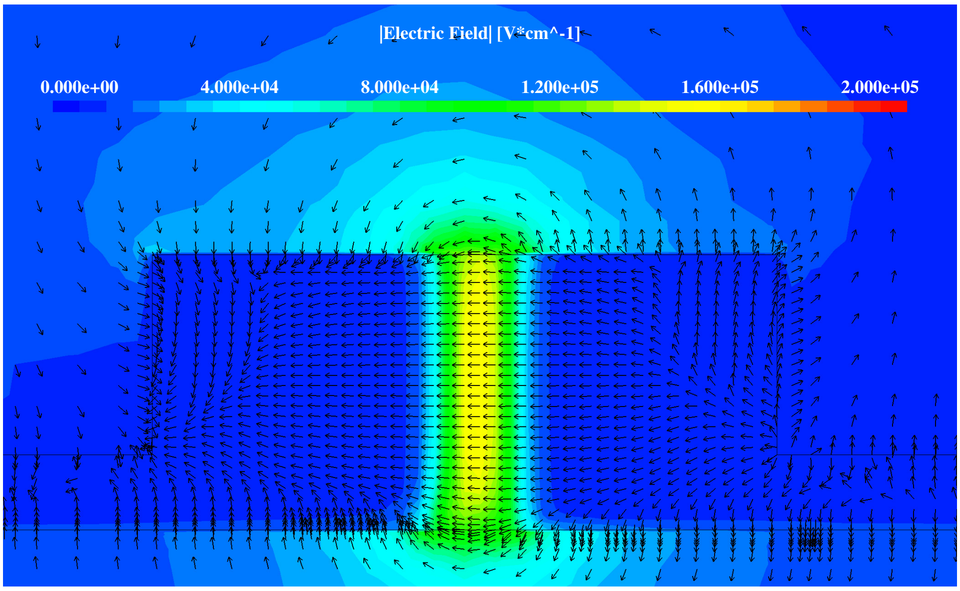

(b) *Electric field (neutron irradiation).*

Figure 3.15: Absolute electric field of the simulated phase shifter under equilibrium condition in the pre-irradiation simulation (a) and with the PSB model (b) used to simulate the neutron damage.

between $\phi \simeq 5 \cdot 10^{14}$ n/cm^{-2} and $\phi \simeq 1 \cdot 10^{16}$ n/cm^{-2}, while higher discrepancies are shown for low fluences. The outcomes of the simulations are compared with the current-voltage characteristics of the irradiated PICs in Figure 3.16.

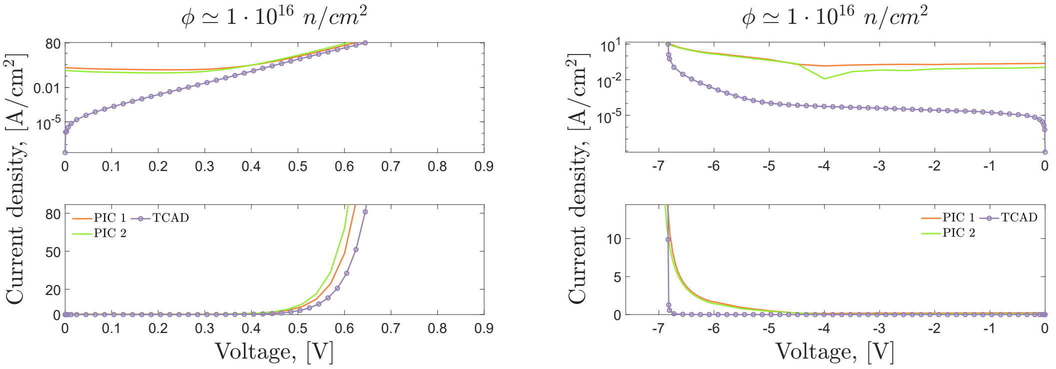

(a) *Forward bias.*
(b) *Reverse bias.*

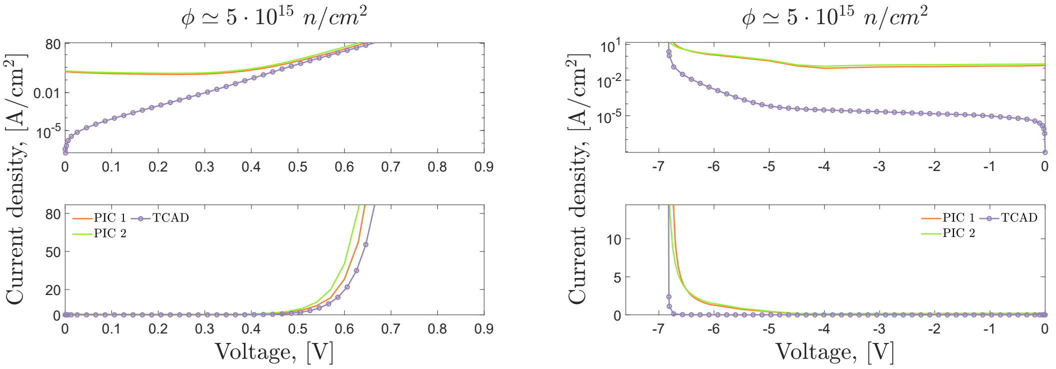

(c) *Forward bias.*
(d) *Reverse bias.*

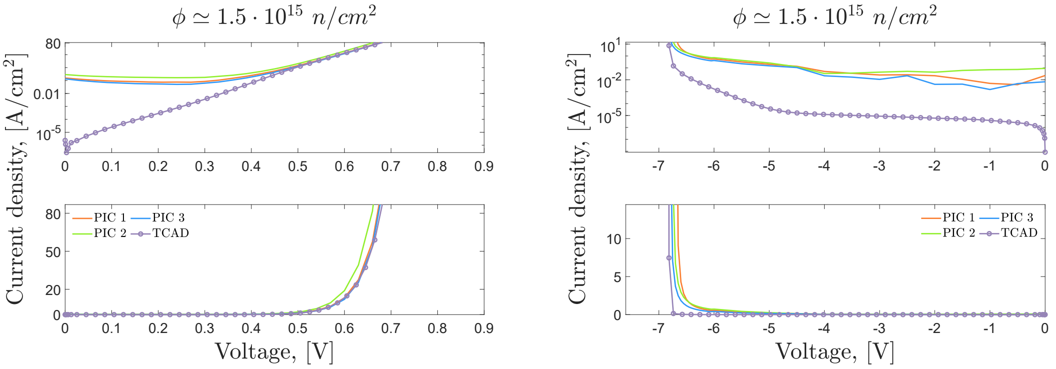

(e) *Forward bias.*
(f) *Reverse bias.*

Figure 3.16: Current-voltage characteristics for RM 0 of the irradiated PICs under different neutron fluence levels compared with the TCAD simulations.

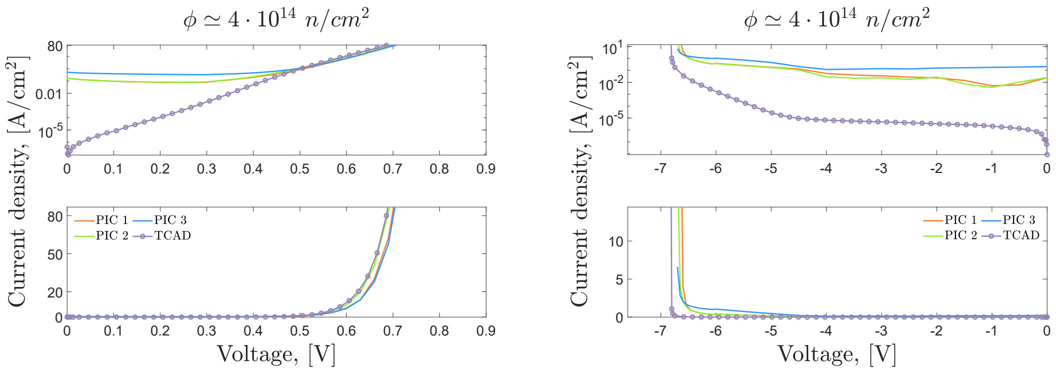

(g) *Forward bias.*
(h) *Reverse bias.*

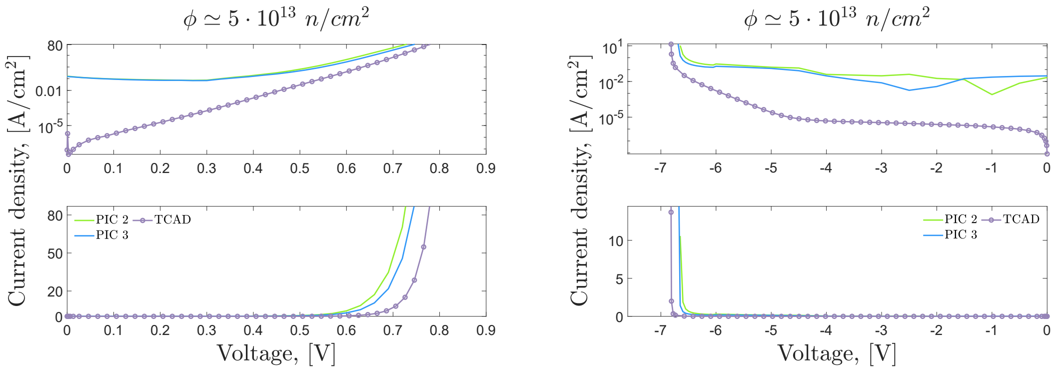

(i) *Forward bias.*
(j) *Reverse bias.*

Figure 3.16: Current-voltage characteristics for RM 0 of the irradiated PICs under different neutron fluence levels compared with the TCAD simulations (continued).

In summary, the simulation of the phase shifter produced excellent results compared to real measurements. The analytical model adopted to identify the doping profiles was verified by the simulation of the current-voltage characteristics. Furthermore, the “Hamburg Pentatrap Model” and the “Perugia Surface and Bulk model” were adopted in the *sdevice* environment to simulate the effects induced by neutron irradiation in the tested RMs. Simulation results were then compared with the measured data acquired during the irradiation test for different levels of neutron fluence. Upon comparison, a significant level of coherence was identified between the simulations and measurements obtained. The chosen models successfully project the trends detected in the threshold and breakdown voltages of the devices. Moreover, the increase in the reverse saturation current, which could not be accurately monitored during the irradiation test, supports the theoretical expectations. The presented model could be used to improve understanding of the physical effects of neutron irradiation in SiPh devices, ultimately aiding the design of new components to maximize their radiation hardness.

Chapter 4

Conclusions

The research presented in this thesis carried out an extensive characterisation on different photonic components within a SiPh PIC developed at CERN. Neutron irradiation tests were conducted on the devices, and electro-optic characteristics were obtained, with a maximum neutron fluence of of $3.8 \cdot 10^{16}$ n/cm^2 (23 MeV). This was the highest fluence level reached for this type of testing. The key FOMs relevant to the device characterisation were derived from the current-voltage characteristics and the optical spectra. The results have shown a degradation of the device responses as a result of neutron irradiation. However, SiPh components have demonstrated good performance even at extremely high neutron fluences, thus making them a suitable candidate for future high-speed links for HEP.

Three PICs were irradiated at different neutron fluxes, where 14 devices for each PIC were analysed at different temperatures. A reference PIC was simultaneously tested with the same experimental setup conditions in a radiation-free environment. The test involved a total of 54 DUTs that were electrically measured and 16 optical waveguides whose spectra were acquired, each containing a different bus of RMs. Despite the different neutron fluxes, all tested devices in the irradiated PICs have shown to follow the same trend with neutron fluence. Therefore, we can conclude that there is not significant flux dependence in the device response.

The devices were minimally affected by varying temperature conditions (from RT to 125 °C), and only during the post-irradiation measurements a small annealing effect was recorded for the DUTs at higher temperatures. This irradiation test yielded a good statistic of the device response under neutron fluence and agreement with theoretical expectations was found.

Out of all the DUTs, greater attention was given to ring modulator RM 0, which was the reference design and will also be the design employed for the next PIC generation. The characterisation of this device has been further developed using a TCAD model realised with the Synopsys® Sentaurus™ software. An initial investigation was carried out to determine the unknown doping profiles of the RM phase shifter, starting from the sheet resistance and developing an analytical model based on the "Arora model" for carrier mobilities [11]. The distribution of the doping profiles was then implemented by simulating multiple ion implantation steps using the *sprocess* tool, combining the results of the analytical model with the results of the Lumerical simulations. The TCAD structure was then electrically simulated and compared with pre-irradiation measurements, showing good agreement. The macroscopic effects of the damage induced by neutron irradiation on the electrical characteristics of the device were implemented in the simulation environment using two different models for radiation damage in silicon: the “Hamburg Pentatrap Model” [43] and the “Perugia Surface and Bulk” model [12]. Both models introduce different trap states in the silicon energy band gap, where the trap concentrations can be calculated as functions of fluence. The simulated current-voltage characteristics were compared with the irradiation measurements, yielding good agreement.

4.1 Future perspectives

SiPh have demonstrated to be a suitable candidate for HEP. In order to implement SiPh PICs in the harsh environment of LHC detectors further research must be carried out.

Future irradiation tests must be conducted to analyse the response of the PIC in the frequency domain, evaluate the bandwidth, and how radiation modifies the device response. These tests aim to simulate the working conditions of the PIC within LHC detectors. Signal generators will emulate the data coming from the particle sensors, while the PIC will be interfaced with electronic chips that drive the electrical signals to the phase shifter of the RMs. Meanwhile, the control signal will be sent from the BE electronics to the FE apparatus, and the signals will be opto-electrically converted by Ge-on-Si photodetectors during irradiation. Due to the complexity of the system, a comprehensive study by multiple research teams is required to achieve reliable, high-speed and radiation-hard link systems for HEP applications.

New irradiation tests must be conducted to validate the devices for the radiation level expected for the high-luminosity upgrade of LHC particle accelerator for the next decades. Therefore, in addition to neutron irradiation, it is essential to conduct proton and X-ray irradiation tests to validate the PICs at various fluences and TID over the next years.

The SiPh PIC analysed in this study will be succeeded by the next generation of PICs, respectively PICv3 and PICv4, which are already in the manufacturing phase. The first challenge will be the migration from the C-band to the O-band, which will require an extensive characterisation of the devices within this band. The forthcoming generation of PICs will no longer rely on fibre grating coupling, as has been the case with the PIC presented in this thesis. Instead, edge coupling will be used. This eliminates the response of grating couplers that was present in the optical spectra, but also necessitates a highly precise alignment of the fibres with the PIC to reduce losses caused by air gaps and reflections of light.

It is fundamental to deepen the understanding of radiation damage in SiPh devices in order to develop reliable models capable of predicting device responses. Additional research is required to expand the available models for radiation damage in silicon and to extend the simulations to different device families, which are currently being developed mainly for electronic components for particle sensors. Once a reliable model has been developed, the future design of SiPh components, such as RMs or Ge-on-Si PDs, can be optimised in the simulator environment prior to fabrication, facilitating the efficient production of radiation-hardened PICs for HEP applications.

Appendix A

Scheme of the IGOR Pro measurement loop

The code was developed to achieve a compromise between accuracy and time. The time of each measurement cycle could not be too long; otherwise, the evaluation of the radiation damage with the neutron fluence would have been meagre. Moreover, the variety of devices analysed led to different specific settings for each of them, including compliances and current limits. The high-level flow chart of the generic measurement loop scheme is reported in Figure A.1.

The most sensitive acquisitions are the current-voltage characteristics because the aim was to evaluate the DUTs over the entire range, thus from the forward to the breakdown. The proper voltage limits had to be found and since they were not known a priori a series of preliminary tests were conducted before the irradiation test. However, the way in which the final experimental conditions and the irradiation damage would have modified the characteristics of the DUTs was unknown. Therefore, the code was developed to be self-consistent and automatically update the scanning range after each measurement. The first cycle, 'run 0', is the most time consuming but also the most accurate and is carried out before the irradiation. From the first measurement loop, the threshold voltage and breakdown limits are calculated for each DUT; these limits are then used to speed up the next measurement cycles. For instance, all DUTs are mainly diodes with different specifications, but the characteristic is known. This leads to developing a code capable of acquiring spreader measurement points in the low-current regions (both reverse saturation current and forward) and then increasing the resolution in the proximity of the breakdown and threshold forward voltages, finding a good compromise between measurement resolution and speed. Moreover, new voltage limits were evaluated at each run cycle for each DUT, to be used for the next measurement loop, and so forth.

In addition to 'run0', the approximate time of a complete cycle was 21 minutes, including electrical and optical measurements, which means that each of the 56 DUTs and 16 optical channels were measured more than 100 times during the 34 hours of neutron irradiation, leading to a substantial number of data sets.

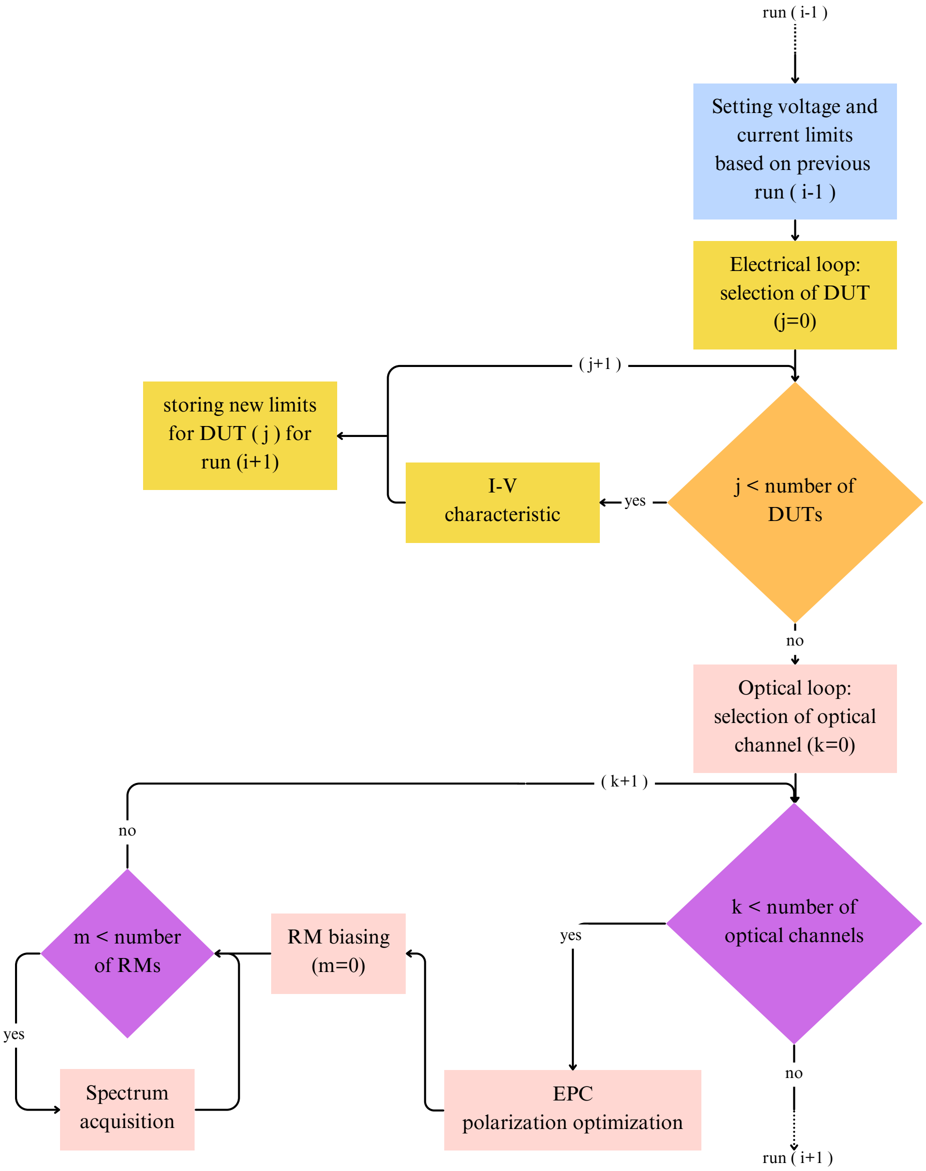

Figure A.1: Flowchart of a single measurement loop with IGOR Pro.

Appendix B

Mehtod for the post-processing of electro-optical measurements

B.1 Electrical post-processing

The current-voltage characteristics obtained for each tested device were used to derive four FOMs: threshold and breakdown voltages, together with the current swing in the forward and breakdown regions (which are not shown in this thesis). All the DUTs exhibit diode characteristics; therefore, the methodology for the derivation of the aforementioned parameters is based on a standard procedure that involves linear fitting of the current. Concerning forward bias, the first step performed to reduce measurement noise was to perform an exponential fitting of the I-V characteristic. Subsequently, this curve was used to estimate the threshold voltage and the swing by performing a linear fitting in the conduction region. To evaluate the swing, it is necessary to calculate the logarithm of the current and then to perform again a linear fitting, to extract the slope. The swing is defined as the inverse of the slope, i.e. for a linear characteristic can be defined as:

$$\text{Swing}\big|_{\text{mV/dec}} = |\text{Slope}|^{-1} = \left|\frac{\mathrm{d}\log_{10} I}{\mathrm{d}V|_{\text{mV}}}\right|^{-1}. \tag{B.1}$$

Figure B.1a shows the procedure followed for the post-processing of the electrical data. The method applied in reverse is complementary but without performing exponential fitting.

Exponential fitting of the characteristic was not feasible under reverse bias. Therefore, a linear fitting was used to extrapolate the breakdown voltage. Subsequently, by computing the logarithm of the absolute value of the current, another linear fitting was carried out to determine the swing.

In the outcomes reported in Section 2.4.1 a stepwise profile is noticeable for some parameters (e.g. breakdown voltage). This phenomenon results from the current compliance set during the irradiation test to protect the DUTs. In fact, since the test was intended to measure diode currents in sensitive areas, such as breakdown, the instrument compliance

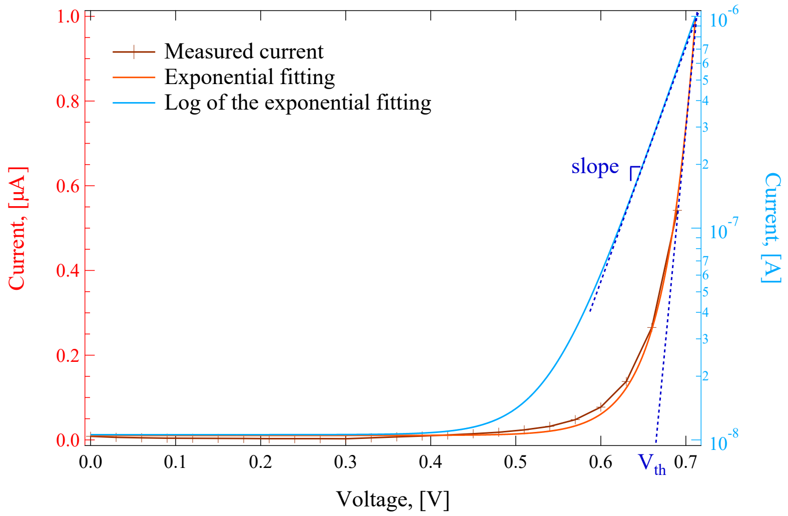

(a) *Procedure used to extrapolate the characterising parameters of the diode starting from the raw current measurements, in forward bias.*

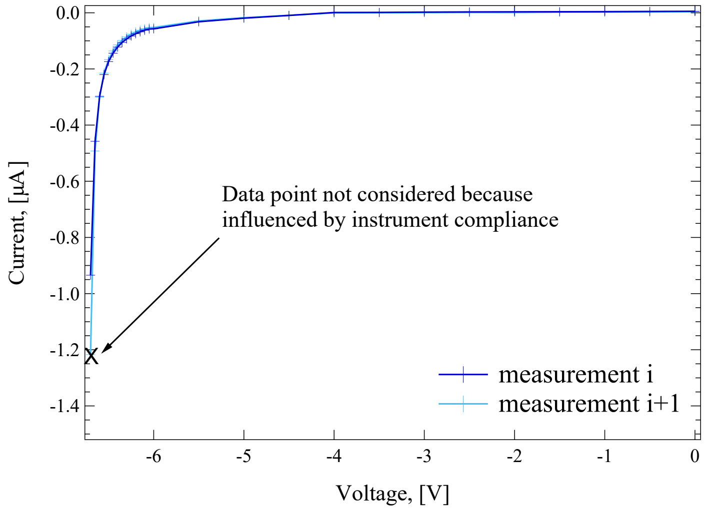

(b) *Example of a raw current-voltage characteristic measurement in reverse bias. Due to the instrument current compliance, the acquired current values greater than 1 µA (for RMs and PDs) were not considered reliable due to instrument limitation. These values were therefore not taken into account for the linear fitting to evaluate breakdown voltage and current swing.*

Figure B.1: Post-processing method for the electrical measurements.

current limit was set to 1 µA for RMs and PDs. For MZMs, the current compliance limit was set to 1 mA due to their larger physical dimensions. When the current value exceeds this limit, the instrument's compliance intervenes, resulting in an impact on the actual current, and any data exceeding this limit are not considered for the data analysis. This results in a variation in the number of data points obtained at both voltage sides during current-voltage measurements. However, for the forward voltage, this contribution is not noticeable because of the exponential fitting of the characteristic, which eliminates this issue. Even so, in analysing the breakdown, it was not possible to perform an exponential fitting of the specific characteristic; therefore, both breakdown voltage extracted from the linear fitting of the raw current measurements show this trend.

An example of the reverse current-voltage characteristic with different acquired data points is shown in Figure B.1b. It is evident that when performing a linear fit to extrapolate the breakdown voltage, the absence of a current point leads to a difference between two consecutive measurements.

B.2 Optical post-processing

The optical spectra of the ring modulators are affected by the grating coupler response; hence, the contribution of the latter has been deducted for the RM analysis. Grating couplers are periodic structures that allow the light guided mode to be coupled to the waveguide for a specific combination of incident angle and light frequency [23]. The double grating used for both light input and output in our PICs limit the overall bandwidth and provides a characteristic response in the optical spectrum.

The typical equations describing a GC could be used to evaluate their response and subtract its contribution from the spectrum, but the variation of the GC due to neutron irradiation is not well known and was out of the scope of this work to evaluate it. Therefore, to isolate the RM resonance peaks, the approach used was to subtract the same GC response to the optical spectrum by eliminating the wavelength in the proximity of the resonances. By applying a mask to the optical spectra of ±1.5 nm around the RM resonance peaks, and then interpolating the empty region, we were able to obtain a consistent GC response, which is shown in Figure B.2a. Then, this response was subtracted from the optical spectrum to isolate the RM resonance profiles, which are now aligned at the same power level. This procedure ensures reliable isolation of the RM response and can be iterated on all irradiated data without being affected by variations in the GC response. Lorentzian fitting was then used to evaluate the resonance peaks and all FOMs of the ring, as reported in Figure B.2b.

Note that the optical power level should be zero since we subtract the exact GC response, resonance peaks apart, but this would not be feasible for the evaluation of the following FOMs, such as intrinsic extinction ratio (ERi) or transmission penalty (TP). Therefore, to be consistent throughout the analysis and considering that the spectra were acquired for different voltages applied to the RMs, the input power was taken from the interpolated optical spectrum corresponding to the RM resonance peak (P_{in} in Figure B.2a) and it was used to shift the entire normalised spectrum. Clearly, the corresponding input power was evaluated accordingly for each peak, i.e. for each ring modulator.

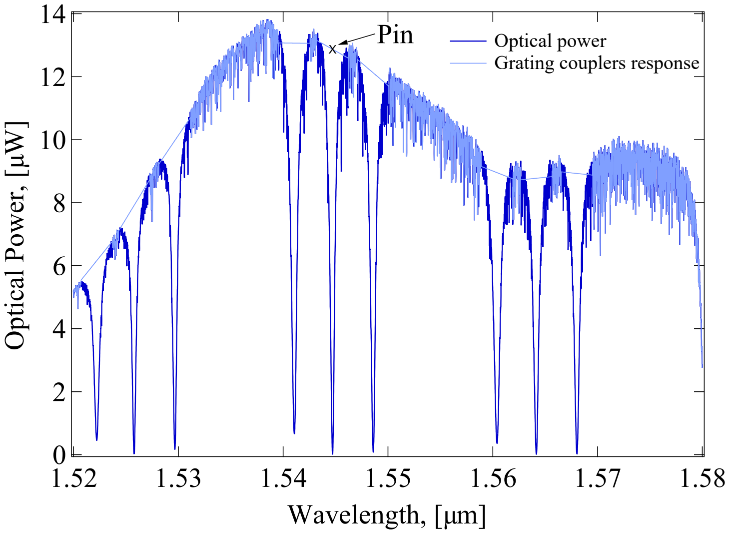

(a) *Optical spectrum with interpolation of GC response.*

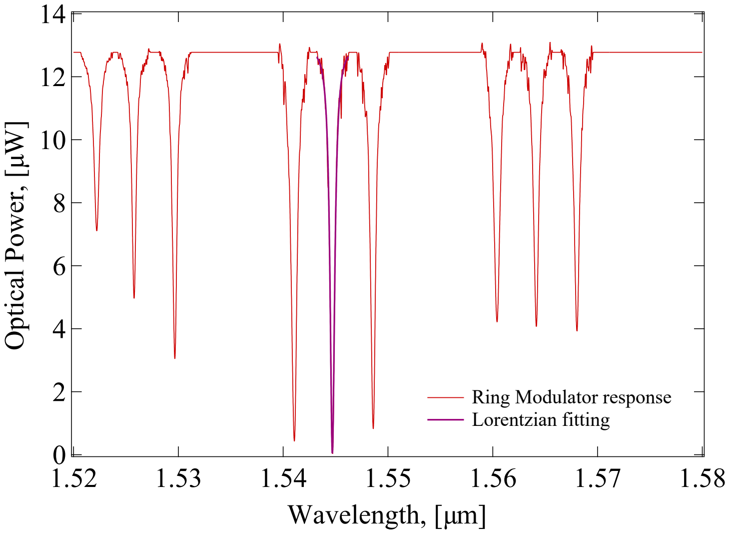

(b) *Optical spectrum with the resonance peaks of RMs, without the GC response.*

Figure B.2: Post-processing procedure to isolate the RMs response in the optical spectrum from the one of GCs. B.2b shows also the Lorentzian fitting of the normalised spectrum, in particular the resonance peak corresponds to RM 0.

Bibliography

[1] Key Facts and Figures - CERN Data Centre. Nov. 2021. URL: https://information-technology.web.cern.ch/sites/default/files/CERNDataCentre_KeyInformation_Nov2021V1.pdf.

[2] Official CERN website, accessed 13/11/2023. URL: https://home.cern/.

[3] Official CERN website, "High Luminosity LHC Project" accessed 16/11/2023. URL: https://hilumilhc.web.cern.ch/article/ls3-schedule-change.

[4] Versatile Link project, public area. URL: https://espace.cern.ch/project-versatile-link/public/default.aspx.

[5] Versatile Link Plus project, public area. URL: https://espace.cern.ch/project-Versatile-Link-Plus/SitePages/Home.aspx.

[6] Optical data transmission for LHC experiment Phase-2 upgrades. URL: https://ep-news.web.cern.ch/content/optical-data-transmission-lhc-experiment-phase-2-upgrades.

[7] R&D programs for the Experimental Physics Department of CERN. URL: https://ep-rnd.web.cern.ch/.

[8] O. Aberle et al. *High-Luminosity Large Hadron Collider (HL-LHC): Technical design report*. CERN Yellow Reports: Monographs. Geneva: CERN, 2020. DOI: 10.23731/CYRM-2020-0010. URL: https://cds.cern.ch/record/2749422.

[9] J. C. Adcock et al. “Advances in Silicon Quantum Photonics”. In: *IEEE Journal of Selected Topics in Quantum Electronics* 27.2 (2021), pp. 1–24. DOI: 10.1109/JSTQE.2020.3025737.

[10] P.P. Altermatt et al. “Reassessment of the intrinsic carrier density in crystalline silicon in view of band-gap narrowing”. In: *Journal of Applied Physics* 93.3 (Feb. 2003), pp. 1598–1604. ISSN: 0021-8979. DOI: 10.1063/1.1529297. URL: https://doi.org/10.1063/1.1529297.

[11] N.D. Arora, J.R. Hauser, and D.J. Roulston. “Electron and hole mobilities in silicon as a function of concentration and temperature”. In: *IEEE Transactions on Electron Devices* 29.2 (1982), pp. 292–295. DOI: 10.1109/T-ED.1982.20698.

[12] P. Asenov et al. “TCAD modeling of bulk radiation damage effects in silicon devices with the Perugia radiation damage model”. In: *Nuclear Instruments and Methods in Physics Research Section A: Accelerators, Spectrometers, Detectors and Associated Equipment* 1040 (2022), p. 167180. ISSN: 0168-9002. DOI: `https://doi.org/10.1016/j.nima.2022.167180`. URL: `https://www.sciencedirect.com/science/article/pii/S0168900222005459`.

[13] W.E. Beadle, J.C.C. Tsai, and R.D. Plummer. *Quick Reference Manual for Silicon Integrated Circuit Technology*. Wiley-Interscience publication. Wiley, 1985. ISBN: 9780471815884. URL: `https://books.google.ch/books?id=WihTAAAAMAAJ`.

[14] W. Bogaerts et al. “Silicon microring resonators”. In: *Laser & Photonics Reviews* 6.1 (2012), pp. 47–73. DOI: `https://doi.org/10.1002/lpor.201100017`. eprint: `https://onlinelibrary.wiley.com/doi/pdf/10.1002/lpor.201100017`. URL: `https://onlinelibrary.wiley.com/doi/abs/10.1002/lpor.201100017`.

[15] J.E. Bowers. “Silicon photonics and applications in aerospace”. In: 2015 IEEE Avionics and Vehicle Fiber-Optics and Photonics Conference (AVFOP) (2015), pp. 17–18. DOI: `10.1109/AVFOP.2015.7356633`.

[16] H. Chen et al. “-1 V bias 67 GHz bandwidth Si-contacted germanium waveguide p-i-n photodetector for optical links at 56 Gbps and beyond”. In: *Optics Express* 24.5 (Mar. 2016), pp. 4622–4631. DOI: `10.1364/OE.24.004622`. URL: `https://opg.optica.org/oe/abstract.cfm?URI=oe-24-5-4622`.

[17] H. T. Chen et al. “High-Responsivity Low-Voltage 28-Gb/s Ge p-i-n Photodetector With Silicon Contacts”. In: *Journal of Lightwave Technology* 33.4 (2015), pp. 820–824. DOI: `10.1109/JLT.2014.2367134`.

[18] K.P. Cheung. “On the 60 mV/dec @300 K limit for MOSFET subthreshold swing”. In: (2010), pp. 72–73. DOI: `10.1109/VTSA.2010.5488941`.

[19] S.L. Chuang. *Physics of Photonic Devices*. Wiley Series in Pure and Applied Optics. Wiley, 2009. ISBN: 9780470293195. URL: `https://books.google.ch/books?id=x5Cd__PDf1kC`.

[20] F. De Leonardis et al. “Modeling of Radiation Effects in Silicon Photonic Devices”. In: *IEEE Transactions on Nuclear Science* 62.5 (2015), pp. 2155–2168. DOI: `10.1109/TNS.2015.2469671`.

[21] *Diffused Ion Implantation Profile Calculator and Graph*. URL: `https://cleanroom.byu.edu/implantcal`.

[22] M. Ferrero et al. “Radiation resistant LGAD design”. In: *Nuclear Instruments and Methods in Physics Research Section A: Accelerators, Spectrometers, Detectors and Associated Equipment* 919 (2019), pp. 16–26. ISSN: 0168-9002. DOI: `https://doi.org/10.1016/j.nima.2018.11.121`. URL: `https://www.sciencedirect.com/science/article/pii/S0168900218317741`.

[23] F. Fesharaki et al. “Accurate theoretical and experimental characterization of optical grating coupler”. In: *Optics Express* 24.18 (Sept. 2016), pp. 21027–21037. DOI: `10.1364/OE.24.021027`. URL: `https://opg.optica.org/oe/abstract.cfm?URI=oe-24-18-21027`.

[24] M. Huhtinen. "Simulation of non-ionising energy loss and defect formation in silicon". In: *Nuclear Instruments and Methods in Physics Research Section A: Accelerators, Spectrometers, Detectors and Associated Equipment* 491.1 (2002), pp. 194–215. ISSN: 0168-9002. DOI: https://doi.org/10.1016/S0168-9002(02)01227-5. URL: https://www.sciencedirect.com/science/article/pii/S0168900202012275.

[25] S. Karimelahi et al. "Optical and electrical trade-offs of rib-to-contact distance in depletion-type ring modulators". In: *Optics Express* 25.17 (Aug. 2017), pp. 20202–20215. DOI: 10.1364/OE.25.020202. URL: https://opg.optica.org/oe/abstract.cfm?URI=oe-25-17-20202.

[26] M. Karpiński, C. Radzewicz, and K. Banaszek. "Fiber-optic realization of anisotropic depolarizing quantum channels". In: *Journal of the Optical Society of America B* 25.4 (Apr. 2008), pp. 668–673. DOI: 10.1364/JOSAB.25.000668. URL: https://opg.optica.org/josab/abstract.cfm?URI=josab-25-4-668.

[27] A. Kraxner et al. "Radiation tolerance enhancement of silicon photonics for HEP applications". In: *Proceeding of science* TWEEP2018 - Topical Workshop on Electronics for Particle Physics (2019), p. 150. DOI: 10.22323/1.343.0150. URL: https://cds.cern.ch/record/2710223.

[28] M. Lalovic et al. "Ionizing Radiation Effects in Silicon Photonics Modulators". In: *IEEE Transactions on Nuclear Science* 69 (July 2022), pp. 1521–1526. DOI: 10.1109/TNS.2022.3148579.

[29] B.C. MacEvoy, G. Hall, and K. Gill. "Defect evolution in irradiated silicon detector material". In: *Nuclear Instruments and Methods in Physics Research Section A: Accelerators, Spectrometers, Detectors and Associated Equipment* 374.1 (1996), pp. 12–26. ISSN: 0168-9002. DOI: https://doi.org/10.1016/0168-9002(96)37410-X. URL: https://www.sciencedirect.com/science/article/pii/016890029637410X.

[30] M. Moll, E. Fretwurst, and G. Lindstrom. "Investigation on the improved radiation hardness of silicon detectors with high oxygen concentration". In: *Nuclear Instruments and Methods in Physics Research Section A: Accelerators, Spectrometers, Detectors and Associated Equipment* 439.2 (2000), pp. 282–292. ISSN: 0168-9002. DOI: https://doi.org/10.1016/S0168-9002(99)00842-6. URL: https://www.sciencedirect.com/science/article/pii/S0168900299008426.

[31] A. Morozzi et al. "TCAD advanced radiation damage modeling in silicon detectors". In: *PoS* Vertex2019 (2020), p. 050. DOI: 10.22323/1.373.0050.

[32] M. Nagli et al. "Silicon-photonics focused ultrasound detector for minimally invasive optoacoustic imaging". In: *Biomedical Optics Express* 13.12 (Dec. 2022), pp. 6229–6244. DOI: 10.1364/BOE.470295. URL: https://opg.optica.org/boe/abstract.cfm?URI=boe-13-12-6229.

[33] A.F.A. Noorden, S. Daud, and J. Ali. "Implication of plasma dispersion effect for controlling refractive index in microresonator". In: *AIP Conference Proceedings* 1824.1 (Mar. 2017), p. 030001. ISSN: 0094-243X. DOI: 10.1063/1.4978819. eprint: https://pubs.aip.org/aip/acp/article-pdf/doi/10.1063/1.4978819/13210403/030001_1_online.pdf. URL: https://doi.org/10.1063/1.4978819.

[34] L. Olantera et al. “Effects of High Fluence Particle Irradiation on Germanium-on-Silicon Photodiodes”. In: *IEEE Transactions on Nuclear Science* (2023), pp. 1–1. DOI: 10.1109/TNS.2023.3327434.

[35] L. Olantera et al. “Radiation Effects on High-Speed InGaAs Photodiodes”. In: *IEEE Transactions on Nuclear Science* 66.7 (2019), pp. 1663–1670. DOI: 10.1109/TNS.2019.2902624.

[36] A. M. Piro et al. “Room-temperature boron displacement in crystalline silicon induced by proton irradiation”. In: *Applied Physics Letters* 86.8 (Feb. 2005), p. 081906. ISSN: 0003-6951. DOI: 10.1063/1.1868874. eprint: https://pubs.aip.org/aip/apl/article-pdf/doi/10.1063/1.1868874/13211236/081906_1_online.pdf. URL: https://doi.org/10.1063/1.1868874.

[37] M. Prabhu et al. “Individually addressable and spectrally programmable artificial atoms in silicon photonics”. In: *Nature Communications* 14.1 (Apr. 2023). DOI: 10.1038/s41467-023-37655-x. URL: https://doi.org/10.1038%2Fs41467-023-37655-x.

[38] T. Prousalidi et al. “System Development of Radiation Tolerant Silicon Photonics Transceivers for High Energy Physics Applications”. In: *IEEE Transactions on Nuclear Science* (2023), pp. 1–1. DOI: 10.1109/TNS.2023.3310059.

[39] G.T. Reed and C.E. Jason Png. “Silicon optical modulators”. In: *Materials Today* 8.1 (2005), pp. 40–50. ISSN: 1369-7021. DOI: https://doi.org/10.1016/S1369-7021(04)00678-9. URL: https://www.sciencedirect.com/science/article/pii/S1369702104006789.

[40] A. Ruzin et al. “Comparison of radiation damage in silicon induced by proton and neutron irradiation”. In: *IEEE Transactions on Nuclear Science* 46.5 (1999), pp. 1310–1313. DOI: 10.1109/23.795808.

[41] C. Scarcella et al. “System development of silicon photonics links for CERN experiments and accelerators”. In: *Journal of Instrumentation* 18.03 (Mar. 2023), p. C03002. DOI: 10.1088/1748-0221/18/03/C03002. URL: https://dx.doi.org/10.1088/1748-0221/18/03/C03002.

[42] D.K. Schroder. *Semiconductor Material and Device Characterization*. Wiley, 1998. ISBN: 9780471241393. URL: https://books.google.ch/books?id=l8N1QgAACAAJ.

[43] J. Schwandt et al. “A new model for the TCAD simulation of the silicon damage by high fluence proton irradiation”. In: *2018 IEEE Nuclear Science Symposium and Medical Imaging Conference Proceedings (NSS/MIC)*. 2018, pp. 1–3. DOI: 10.1109/NSSMIC.2018.8824412.

[44] Y. Shi et al. “Silicon photonics for high-capacity data communications”. In: *Photonics Research* 10.9 (Sept. 2022), A106–A134. DOI: 10.1364/PRJ.456772. URL: https://opg.optica.org/prj/abstract.cfm?URI=prj-10-9-A106.

[45] S. Y. Siew et al. “Review of Silicon Photonics Technology and Platform Development”. In: *Journal of Lightwave Technology* 39.13 (2021), pp. 4374–4389. DOI: 10.1109/JLT.2021.3066203.

[46] R. Soref and B. Bennett. “Electrooptical effects in silicon”. In: *IEEE Journal of Quantum Electronics* 23.1 (1987), pp. 123–129. DOI: 10.1109/JQE.1987.1073206.

[47] Synopsys®. *Sentaurus^{TM} Process User Guide.* Version U-2022.12. Dec. 2022. URL: https://www.synopsys.com/.

[48] Pavel Stejskal. "Radiation Effects in Optical Link Components for Future Particle Physics Detectors". Presented 23 May 2013. 2013. URL: https://cds.cern.ch/record/1596006.

[49] S.M. Sze. *Semiconductor Devices: Physics and Technology.* John Wiley & Sons Singapore Pte. Limited, 2012. ISBN: 9780470873670. URL: https://books.google.ch/books?id=gmmscQAACAAJ.

[50] J. Troska et al. "The VTRx+, an optical link module for data transmission at HL-LHC". In: *Proceeding of science* TWEEP2017 - Topical Workshop on Electronics for Particle Physics (2017), p. 048. DOI: 10.22323/1.313.0048. URL: https://cds.cern.ch/record/2312396.

[51] X. Wang et al. "High-speed silicon photonic Mach–Zehnder modulator at 2 μm". In: *Photonics Reseacrh* 9.4 (Apr. 2021), pp. 535–540. DOI: 10.1364/PRJ.417107. URL: https://opg.optica.org/prj/abstract.cfm?URI=prj-9-4-535.

[52] Z. Wang et al. "Silicon photonic integrated circuit swept-source optical coherence tomography receiver with dual polarization, dual balanced, in-phase and quadrature detection". In: *Biomedical Optics Express* 6.7 (July 2015), pp. 2562–2574. DOI: 10.1364/BOE.6.002562. URL: https://opg.optica.org/boe/abstract.cfm?URI=boe-6-7-2562.

[53] C. Zechner et al. "New implantation tables for B, BF2, P, As, In and Sb". In: (Sept. 2002), pp. 567–570. DOI: 10.1109/IIT.2002.1258068.

[54] M. Zeiler et al. "Radiation Damage in Silicon Photonic Mach-Zehnder Modulators and Photodiodes". In: *IEEE Transactions on Nuclear Science* (2017), pp. 2794–2801. DOI: 10.1109/TNS.2017.2754948.

[55] X. Zheng et al. "Enhanced optical bistability from self-heating due to free carrier absorption in substrate removed silicon ring modulators". In: *Optics Express* 20.10 (May 2012), pp. 11478–11486. DOI: 10.1364/OE.20.011478. URL: https://opg.optica.org/oe/abstract.cfm?URI=oe-20-10-11478.